UNDERSTANDING AND IMPROVING ZINC ANODES FOR HIGH-ENERGY RECHARGEABLE ALKALINE BATTERIES

A Dissertation
Presented to
The Academic Faculty

by

Yamin Zhang

In Partial Fulfillment
of the Requirements for the Degree
Doctor of Philosophy in the
School of Chemical and Biomolecular Engineering

Georgia Institute of Technology
December 2020

UNDERSTANDING AND IMPROVING ZINC ANODES FOR HIGH-ENERGY RECHARGEABLE ALKALINE BATTERIES

Approved by:

Dr. Nian Liu, Advisor
School of Chemical and Biomolecular
Engineering
Georgia Institute of Technology

Dr. Elsa Reichmanis
School of Chemical and Biomolecular
Engineering
Georgia Institute of Technology

Dr. Christopher Jones
School of Chemical and Biomolecular
Engineering
Georgia Institute of Technology

Dr. Matthew McDowell
School of Mechanical Engineering
Georgia Institute of Technology

Dr. Dennis Hess
School of Chemical and Biomolecular
Engineering
Georgia Institute of Technology

Date Approved: [September 28, 2020]

The thesis is dedicated to my family.

ACKNOWLEDGEMENTS

First, I would like to thank my PhD advisor, Prof. Nian Liu, for his encouragement, support, and guidance during my entire course of study in Georgia Tech. Specially, his dedication and enthusiasm towards research has been a great inspiration to me. I would also like to thank all my other committee members: Profs. Christopher Jones, Dennis Hess, Elsa Reichmanis, and Matthew McDowell for evaluating my thesis and giving me some valuable suggestions. Additionally, I want to thank Profs. Nian Liu, Dennis Hess, Elsa Reichmanis, and Martha Grover for being my references on my postdoctoral application.

I would like to thank the Liu group members and my colleagues for their assistance throughout my doctoral studies. I would also like to thank Quinn Spadola for giving me a great chance to start GIN seminar series at Georgia Tech so I can host some eminent professors. Staff members of Institute for Electronics and Nanotechnology are much appreciated for helping on my research.

Most importantly, I thank my family for their love and support. I appreciate the companionship of my friends, especially Yifan Zhang and Yixuan Chen during my hard time. I also appreciate Yifeng Shi for her delicious desserts. They are precious to me. Lastly, I would like to acknowledge my friends who play badminton and Werewolf with me in my spare time.

TABLE OF CONTENTS

LIST OF TABLES

LIST OF FIGURES

Zn anodes for the first 200 galvanostatic cycles. Accumulated discharge areal capacity is calculated by adding the discharge areal capacity of all cycles together. (d) Voltage profiles of the 20th galvanostatic cycle of bare and GO-modified Zn anodes. (e) Nyquist plots of the bare and GO-modified Zn anodes before and after cycling.

solution for 14 days. (b) Percentages of ZnO that has been dissolved in solution over time, measured using inductively coupled plasma atomic emission spectroscopy (ICP-AES). After 14 days, 68.3% of ZnO in open structured electrode was dissolved, while only 15.5% ZnO in lasagna structured electrode was dissolved.

showing lattice of ZnO, [002], d= 0.26 nm. h, Electron diffraction pattern of ZnO@TiN$_x$O$_y$ nanorod, showing diffraction pattern of ZnO. A [002]; B [200]; C [202]. i, XPS survey of ZnO nanorod and ZnO@TiN$_x$O$_y$ nanorod anodes. j, High-resolution XPS spectra of Zn 2p peaks. k, High-resolution XPS spectra of Ti 2p peaks. The samples shown in Fig. d-k are all deposited by ALD for 100 cycles.

ZnO nanorods grown on the inner carbon fibers were not in contact with electrolyte in the first charge, and remained.

TiO$_2$ coating (c). (d) SEM image and elemental mappings of the HSSN anode.

plot) are marked as red circles. c, Cycle life comparison of the C-Ag and C electrodes with relative standard deviations of the discharge capacities over cycling being less than 1%. This result shows that the electrochemical cycling of the C-Ag electrode is more stable than that of the C electrode. d, Cycling performance of the C-Ag-Zn and C-Zn anodes. e, Box-and-whisker plot showing a comparison between the C-Ag-Zn anode and previously published works in terms of cycle life, Coulombic efficiency, and DC/E ratio.

of 2 V or a charge capacity of 0.212 mAh/cm^2, followed by full discharge to 1.2 V in a ZnO-saturated 4 M KOH electrolyte. Cycle range: 50th–60th.

LIST OF SYMBOLS AND ABBREVIATIONS

Zn   zinc

ZnO   zinc oxide

HER   hydrogen evolution reaction

Li   lithium

LIB   lithium ion battery

GO   graphene oxide

TiN   titanium nitride

TiN_xO_y titanium oxynitride

TiO_2 titanium oxide

O_2 oxygen

S   sulfur

MnO_2 manganese oxide

NiOOH   nickel oxide hydroxide

$Ni(OH)_2$ nickel hydroxide

OH^- hydroxide

H_2O water

e^- electron

E   potential

SHE   standard hydrogen electrode

$Zn(OH)_4^{2-}$ zincate

OER   oxygen evolution reaction

ORR   oxygen reduction reaction

DOD   depth of discharge

Zn^{2+} zinc ion

M   mol/L

KOH   potassium hydroxide

DFT   density functional theory

H_2 hydrogen

Ag   silver

Cu   copper

Ni   nickel

Au   gold

Ti   titanium

Fe   iron

Pt   platinum

Hg   mercury

HgO   mercury oxide

Ar   argon

SUMMARY

Batteries with aqueous electrolytes generally feature better intrinsic safety, higher ionic conductivity and lower cost compared with flammable organic electrolytes. Metallic zinc as a rechargeable anode material for aqueous batteries has gained tremendous attention with merits of intrinsic safety, low cost, and high theoretical volumetric capacity (5854 mAh cm^{-3}). Among zinc-based batteries, Zn-air batteries are promising with highest theoretical volumetric energy density (~3x of traditional LIBs). Rechargeable zinc anode has achieved big progress in neutral electrolytes, yet developed slowly in alkaline electrolytes, which are kinetically favorable for air cathodes. Passivation, dissolution, hydrogen evolution reaction (HER), and dendrite formation are four reasons for irreversibility of zinc anodes in alkaline electrolytes.

This research comprises three parts: material, mechanism, and device. From the aspect of material, 4 types of zinc anodes were designed and synthesized to overcome above issues and improve their reversibility. These anodes include graphene oxide-modified (Zn@GO), lasagna-inspired (ZnO@GO), sealed (ZnO@TiN$_x$O$_y$), and hydrogen-evolution-suppressing (ZnO@TiO$_2$) anodes, which improve the deep cycling performance when cycled at lean electrolyte. From the aspect of mechanism, the underlying mechanism of the spatial control of zinc deposition on zinc alloy anodes has been elucidated for the first time. The spatially controlled Zn deposition was visualized for the first time by operando optical microscopy. From the aspect of device, it was discovered that the testing device material has a clear effect on the hydrogen evolution. Specifically, stainless-steel

coin cell cases, as widely used devices in research laboratories, accelerate the HER. Plastic

devices were successfully constructed to minimize the HER.

CHAPTER 1.   INTRODUCTION

Environmental concerns of fossil fuels drive people to develop clean energy economy [1]. Rechargeable batteries are regarded as a green energy storage system and have great potential to alleviate the energy and environmental problems. Their benefits of convenience, low cost, and reliability are the 'enablers' for their use in mobile electronic devices, electric vehicles and grid energy storage [2–4]. A key aspect of any future battery technology development is safety. Although lithium ion batteries (LIBs) are ubiquitous, there are still challenges related to their energy density, cycle life, cost and safety [5–8]. In regard to safety, compared with organic electrolyte, aqueous rechargeable batteries may provide a safer alternative for reliable, low-cost and large-scale energy storage systems. As seen from the penetration test in Figure 1.1a-b, the battery with organic electrolyte catches fire, yet the battery with aqueous electrolyte is relatively safe [9]. Moreover, aqueous batteries have high ion conductivity and cost effectiveness [10–17]. Generally, the cell voltage and energy density of aqueous batteries are lower than those of organic-based batteries (e.g. Li-ion) because of the relatively smaller electrochemical stability window of water. Among all the metals that are stable in water, zinc is the most active and has the lowest possible operating potential [9]. This means using Zn anode can increase overall cell voltage of aqueous batteries. Moreover, zinc is globally available, inexpensive (3.19 USD kg^{-1} [18]), and has high capacity (820 Ah kg^{-1} and 5854 Ah L^{-1}). Zinc-based aqueous batteries also possess the stability to be operated in ambient air. Accordingly, Zn aqueous rechargeable batteries are promising to become a safer energy storage system [19–28]. In Figure 1.1c, I compare the theoretical specific and volumetric capacities of Li and Zn rechargeable

batteries. Among zinc-based aqueous batteries, Zn-air batteries have high theoretical gravimetric and volumetric energy densities (1,093 Wh kg^{-1} and 6,134 Wh L^{-1}, respectively) [29–33].
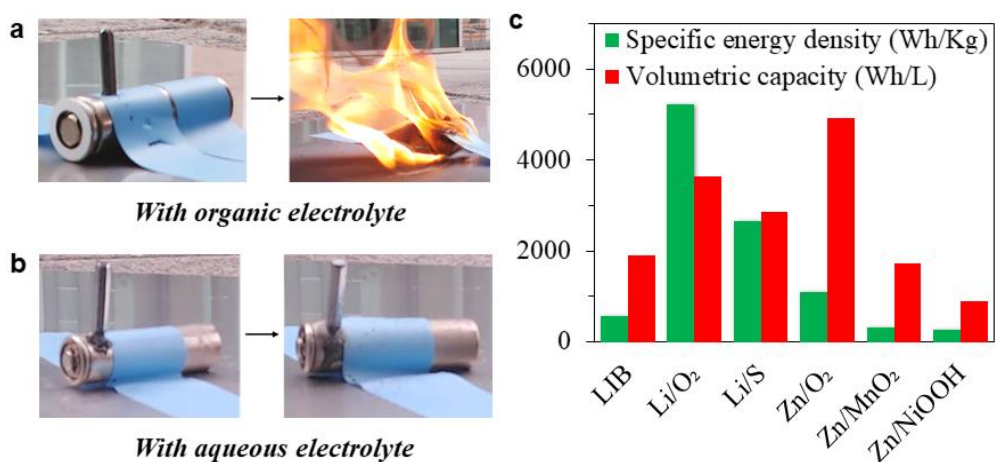
Figure 1.1 - Battery penetration test to investigate the safety property of organic electrolyte (a) and aqueous electrolyte (b). (c) Theoretical specific and volumetric energy density of Li and Zn batteries. LiC$_6$ and CoO$_2$ are used to calculate energy densities of LIB.

1.1 General Understanding of Zinc-Air (Zn-Air) Batteries

The Zn-air batteries[31,34] consist of zinc anodes, air cathodes and alkaline electrolytes, as shown in Figure 1.2. Primary Zn-air batteries have already been the battery of choice for hearing aids, which require extremely high energy density and safety. Below are the reactions of Zn-air batteries in aqueous alkaline electrolyte.

The zinc electrode reaction:

$$Zn + 2OH^- \Leftrightarrow ZnO + H_2O + 2e^- \quad E = -1.26V \; vs \; SHE$$
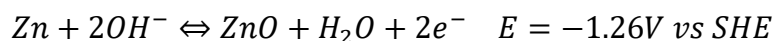
The air electrode reaction:

2

$$O_2 + 2H_2O + 4e^- \Leftrightarrow 4OH^- \qquad E = 0.40V \; vs \; SHE$$
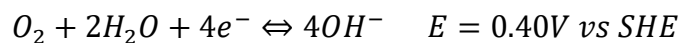
The overall reaction:

$$2Zn + O_2 \Leftrightarrow 2ZnO \qquad E = 1.66V \; vs \; SHE$$
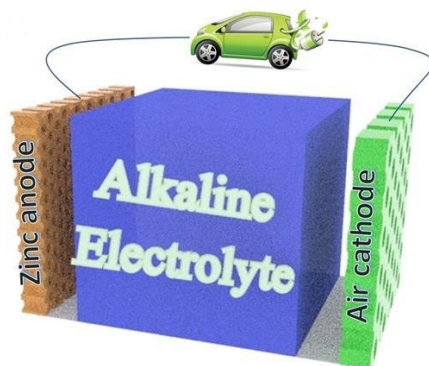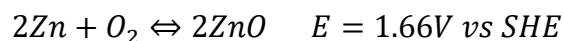
Figure 1.2 - Schematic of zinc air batteries.

Although primary Zn-air batteries have been available in the market for long-duration, low-rate applications, deeply rechargeable ones have not been commercially successful. Also, the practical energy densities of Zn-air batteries are usually between 350-500 Wh/kg[35]. Further rational design and engineering of both cathode and anode are required to achieve high energy-density Zn-air batteries. In this thesis, I focus on Zn anodes.

1.2 Historical Challenges of Rechargeable Zn Anodes

Neutral and alkaline electrolytes are two major classes of aqueous electrolytes for zinc anodes. Research on rechargeable zinc anodes in neutral electrolytes[36,37] has achieved great progress in the past decade; examples include the discoveries of "water-in-salt" electrolytes[38] and molten hydrate electrolytes[39]. Nonetheless, cycling zinc anodes deeply in alkaline electrolytes remains challenging due to the dramatic change of the chemical and

physical forms of zinc species and the severe hydrogen evolution side reaction during cycling[40]. Despite the challenges, it is vital to enable highly rechargeable zinc anodes in alkaline electrolytes to propel the development of rechargeable Zn-air batteries, as air cathodes kinetically favor alkaline electrolytes over neutral ones[41,42]. Even though non-alkaline electrolytes were previously investigated for Zn–air batteries[43], their ORR and OER kinetics at the air cathode are slow. Thus, it is still necessary to study alkaline electrolytes. In alkaline electrolytes, there are two consecutive zinc conversion reactions.

$$ZnO + H_2O + 2OH^- \leftrightarrow Zn(OH)_4{}^{2-}$$

$$Zn(OH)_4{}^{2-} + 2e^- \leftrightarrow Zn + 4OH^-$$
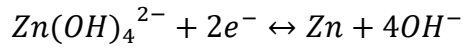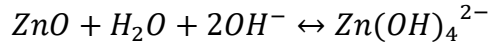
This solid-solute-solid mechanism inherently causes passivation, shape change, and dendrite formation issues on zinc anodes. These issues are due to the following processes: (i) the insulating discharge product ZnO passivates the surface of zinc anodes, preventing the latter from further discharging or recharging back to metallic zinc, (ii) the intermediate zincate ($Zn(OH)_4{}^{2-}$) is soluble in alkaline electrolytes, which leads to active material loss, random ZnO precipitation on the electrode, and morphology change of the electrode over cycling, and (iii) Zn dendrites arise when the deposition reaches beyond the boundary of the diffusion-limited region. In addition, the hydrogen evolution reaction (HER, $2H_2O + 2e^- \rightarrow H_2 + 2OH^-$) is a side reaction on the zinc anode. In an alkaline electrolyte with pH 14, the Zn/ZnO standard reduction potential (-1.26 V vs standard hydrogen electrode (SHE)) is lower than that of the HER (-0.83 V vs SHE). Thus, HER is thermodynamically favored during charging, which causes low Coulombic efficiency, electrolyte drying, bubble accumulation, and eventually cell failure.

1.2.1   Passivation

Passivation is one of the challenges to develop electrochemically rechargeable Zn anode. During the discharge process, active Zn is transformed to relatively insulating ZnO (Figure 1.3), leading to an increase in the internal resistance of the Zn electrode [44–46]. The key factor causing passivation in rechargeable Zn anodes is attributable to the surface concentration of the reaction product [47,48]. This phenomenon inhibits further discharge processes due to the formation of an insulating ZnO film on Zn surface. Besides, precipitation of ZnO on the surface of porous Zn electrodes might reduce the pore volume of these electrodes, leading to the blockage of migration of the hydroxide ions and/or discharge products [49]. This causes the loss of energy efficiency for the charge-discharge cycles (i.e., voltage losses during discharging and voltage increases during charging). This significantly restricts the development of rechargeable Zn-based batteries with high energy density. It is noteworthy that zinc utilization (depth of discharge, DOD) is a common metric used to evaluate the electrochemical rechargeability of Zn anodes [50]. Although the zinc utilization for conventional powder-based electrodes was reported to range from 60–80% [51], it is important to develop Zn anodes that can be operated deeply discharged over repeated cycles. Therefore, it is important to reduce the passivation effect of Zn anodes by adopting the strategies of material design.
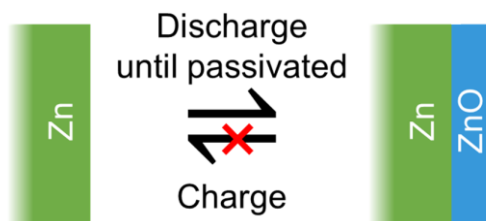
Figure 1.3 - Schematic diagram of the passivation issue of zinc anodes.

1.2.2 Shape Change

Zn electrode shape change (dissolution issue, Figure 1.4), the redistribution of Zn material over the electrode after repeated charge-discharge cycles, has been identified as one of the main life-limiting factors for alkaline Zn-based batteries [52]. It occurs when the dissolved $Zn(OH)_4^{2-}$ and/or Zn^{2+} ions are redeposited onto different locations of Zn electrode during the charge process, resulting in densification of the electrode at specific regions over many charge/discharge cycles. This causes the loss of usable capacity after repeated cycles. The mechanism is attributed to uneven current distribution within the reaction zones, and convective flows when electro-osmotic forces across the battery [53–56].
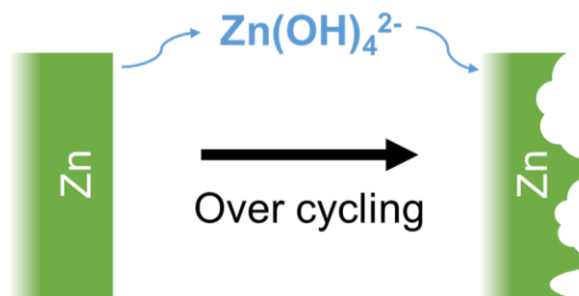
Figure 1.4 - Schematic diagram of shape change of zinc anodes.

Although the deposited Zn structures can be tuned by using specific additives and applied current density [57], Zn shape change is also affected by the concentration of alkaline electrolyte. In typical Zn alkaline batteries, 6–7 M KOH is used due to the maximum electrolyte conductivity [58]. However, the solubility of the discharge product (i.e. ZnO) also increases with increasing electrolyte concentration [59,60]. Therefore, a large amount of Zn dissolves and re-deposits under non-uniform conditions, resulting in a severe shape change of Zn electrode and a poor cycle life [59].

1.2.3   Dendrite Growth

The formation of Zn dendrites is one of the major challenges in secondary alkaline Zn-based batteries [61–63]. A concentration gradient of zincate ions leads to concentration-controlled Zn electrodeposition, where Zn dendrites arise (Figure 1.5) when the deposition reaches beyond the boundary of the diffusion-limited region [64]. Accordingly, dendritic morphologies are formed with repeated cycles, when $Zn(OH)_4^{2-}$ and/or Zn^{2+} ions are deposited faster growth along energetically favorable crystallographic directions [65]. Zn dendrites are sharp, needle-like metallic protrusions reaching hundreds of micrometers in length [66] that can puncture the separator and make contact with the cathode, resulting in internal short circuit and catastrophic failure of Zn-based batteries [67].
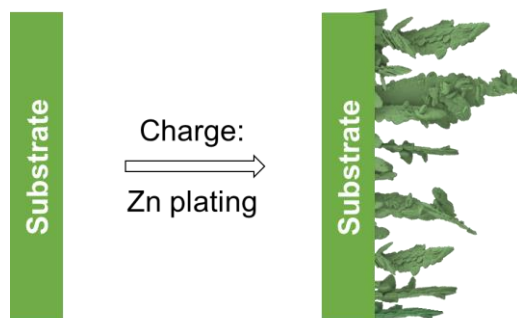
Figure 1.5 - Schematic diagram of dendrite growth on zinc anodes.

The formation of zinc dendrites is mainly controlled by the concentrations of zincate ions and hydroxide ions, the mass transfer process of the electrolyte and current density distributions during charge and discharge [68]. It was reported that dendritic growth arises when the current density was larger than a certain critical value [69]. For instance, cycling Zn electrodes at a current density greater than 10 mA/cm^2 easily induces dendrite formation in alkaline electrolyte [70]. Nonetheless, it is worth mention that dendrites can also

form at lower deposition overpotentials under a long period of time for initiation [69].

Therefore, strategies that can effectively control the dendrite formation must be developed.

1.2.4   Hydrogen Evolution

Hydrogen evolution (Figure 1.6) is thermodynamically favored and inevitably takes place during the operation of Zn-based alkaline batteries. Thus, Zn electrodes cannot be charged with 100% coulombic efficiency, since the H_2 evolution consumes some of the electrons provided to the Zn electrode during charging. Moreover, it generates H_2 gas on the surface of Zn particles in aqueous media by consuming electrolyte during cycling, resulting in battery swell. The rate of H_2 evolution was found to be associated with applied current density and electrolyte concentration [71]. The undesired side reactions can lead to capacity fade and shortened life span of Zn anode [72,73]. Thus, strategies to inhibit H_2 evolution are in great demand to improve the rechargeability of Zn anodes.
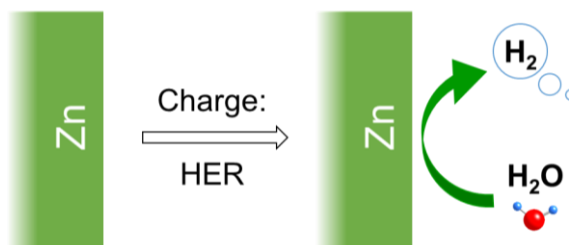
Figure 1.6 - Schematic diagram of hydrogen evolution on zinc anodes.

1.3   Research Motivation

To briefly summarize, the main challenges of rechargeable Zn electrodes are passivation, shape change, dendrite growth, and hydrogen evolution. Attempts have been made in the past to overcome one or two of passivation, dissolution, and HER issues. For example, sub-micron-sized structures[74,75], composites with highly conductive materials[76–

[78], and 3D high surface area electrodes[79,80] have been shown to be effective in addressing the ZnO passivation issue. Surface protective coatings[9,81,82] have been demonstrated to slow down the loss of zinc active material. Specific additives[8365] have been utilized to control the morphologies and suppress dendrite formation on Zn electrodes. Surface treatments[84,85] and additives[86] have been used to suppress the HER. However, there are very few successful examples that address multiple issues simultaneously. In addition, there is a lack of mechanism studies on Zn anodes. Moreover, most previous research has focused on material design, while less attention has been paid to the device level.

1.4   Thesis Overview

This thesis describes systematic approaches to understand and improve zinc anodes for high-energy rechargeable alkaline batteries from three aspects, which are material, mechanism, and device. From the aspect of material (*Chapter 2*), 4 types of zinc anodes have been designed and synthesized to overcome multiple issues simultaneously and improve their reversibility. These anodes include graphene oxide-modified (Zn@GO), lasagna-inspired (ZnO@GO), sealed (ZnO@TiN$_x$O$_y$), and hydrogen-evolution-suppressing (ZnO@TiO$_2$) anodes, which improve the deep cycling performance when cycled at lean electrolyte. From the aspect of mechanism (*Chapter 3*), the underlying mechanism of the spatial control of zinc deposition on zinc alloy anodes has been elucidated for the first time. The thermodynamic and atomic mechanisms of heterogeneous seeded growth were studied both experimentally and computationally (CALPHAD and DFT). Spatially controlled and nondendritic Zn deposition was achieved by inducing Zn alloying and soluble metals on Zn anodes to nucleate and accommodate Zn. The spatially controlled Zn deposition was visualized for the first time by operando optical microscopy.

As a result, the Ag-loaded Zn anode exhibited comprehensively superior cycling performance compared with previously reported deeply cycled Zn anodes in alkaline electrolytes. From the aspect of device (*Chapter 4*), it was demonstrated that the testing device material has a clear effect on the HER in alkaline zinc-based batteries. In addition, the capacity loss on the zinc anode is mainly caused by the HER as identified quantitatively HER through an electrochemical cell–gas chromatography analysis method. Specifically, stainless-steel coin cells, as widely used devices in research laboratories, accelerate the HER due to the synergistic effects of galvanic corrosion and a high HER activity. Plastic cells were successfully constructed and HER was minimized, resulting in a higher Coulombic efficiency and longer cycling life than the stainless-steel coin cell.

CHAPTER 2.   MATERIAL DESIGN OF RECHARGEABLE ZINC ANODES

Four types of zinc anodes have been designed and synthesized to overcome passivation, shape change, dendrite growth, and hydrogen evolution issues and improve their reversibility. These anodes include graphene oxide-modified (Zn@GO), lasagna-inspired (ZnO@GO), sealed (ZnO@TiN$_x$O$_y$), and HER suppressing sealed nanosized (HSSN, ZnO@TiO$_2$) anodes.

2.1   Graphene Oxide-Modified Zn Metal Anode

2.1.1   Introduction

The passivation and dissolution of Zn anodes lead to low utilization of Zn anodes and make it non-rechargeable (Figure 2.1a). Herein, the passivation and dissolution problems of Zn anodes were solved through applying GO onto Zn mesh surface (Figure 2.1b). GO is a layered material, which consists of hydrophilic oxygenated graphene sheets bearing oxygen functional groups on their basal planes and edges [87]. GO has been demonstrated to have ionic sieving capability. Ions that are smaller in size than the GO nanochannel can permeate in the GO layers, while larger ions will be blocked [88]. In addition, GO could be partially reduced when soaked in alkaline solution[89] and facilitate the electron transport across ZnO. Therefore, this structure has the following advantages: (i) During cycling, $Zn(OH)_4^{2-}$ will be blocked by the GO compared to H_2O and OH^-. Thus, the active material loss of anodes can be minimized. (ii) zincate can form hydrogen bonds with oxygen-containing groups on the GO surface and thus has a good affinity with GO,

11

which results in a relatively uniform distribution of zincate among GO layers during the reaction. Once the zincate reaches its solubility, it will decompose to ZnO, which will be encapsulated by GO. The GO encapsulation of ZnO can create the desirable environment for free transportation of electrons and therefore makes ZnO electrochemically active.

Figure 2.1 - Schematic of morphological changes of zinc electrodes during electrochemical cycling. (a) ZnO passivation layer leads to low utilization of the Zn mesh anode. (b) GO on Zn surface makes it possible for electrons to move freely across the insulating ZnO and slows down the dissolution of Zn species.

Zn mesh was chosen to be used as the anode instead of Zn foil because Zn mesh has relatively higher specific surface area with three-dimensional structure. The electrochemical performance of anodes is tested using coin-type cells because they use minimum amount of electrolyte and resemble the practical operating condition. They are assembled in commercial CR2032 coin-type battery cases using NiOOH as the cathode.

2.1.2 *Experimental Section*

Materials. The following materials and chemicals are used in this work: water binder (MTI Corporation), graphite (Sigma-Aldrich), sulfuric acid (H_2SO_4, Fisher Scientific), Zn mesh (Dexmet Corporation), glass fiber (GE Healthcare, WhatmanTM

10370003), commercial Ni-Zn AA batteries (PowerGenix), potassium permanganate ($KMnO_4$, Sigma-Aldrich), potassium hydroxide (KOH, Sigma-Aldrich), potassium fluoride (KF, Sigma-Aldrich), potassium carbonate (K_2CO_3, Sigma-Aldrich).

Synthesis of GO powders. Modified Hummer method is utilized to produce aqueous GO solution [90]. A pretreatment was carried out to prevent the formation of inadequate oxidized graphite-core/GO-shell particles [91]. The pretreated powder was placed in a beaker containing 120 ml concentrated H_2SO_4 solution. Under stirring in ice bath, 15 g $KMnO_4$ was added into the beaker. When the $KMnO_4$ powder dissolved completely, the ice bath was removed, and the beaker was heated to 35°C. After maintaining the mixture temperature at 35°C for 45 min, 200 ml deionized water was added to the beaker drop by drop. The mixture was then heated to 98°C and maintained at 98°C for 15 min. Subsequently, another 700 ml deionized water was added to the mixture in order to decompose unreacted $KMnO_4$ and insoluble MnO_2. The color of the mixture changed to bright-yellow. Subsequently, the GO was centrifuged (7000 rpm, 15 min) and redispersed in water for 5 times to remove ions. The resulting suspension was then subject to a 2 h sonication, followed by a 15-min centrifugation at 4000 rpm. The transparent supernatant was obtained as the GO aqueous solution (~1 g/L). This GO solution was then concentrated using hydrogel beads until a 2.0 g/L concentration was reached. Finally, GO powers were obtained through freeze-drying.

Fabrication of GO-coated Zn anodes. GO/water binder slurry was prepared by mixing 2.1 mg GO powder, 2.4 mg water binder, and 160 μL water in a glass vial under sonication for 60 min. The slurry was then stirred for 1 day at room temperature to ensure thorough mixing. Zn mesh was cut into round disks with 1 cm diameter using a precision

disc cutter and then weighed. After that, the GO slurry was applied onto the surface of the Zn mesh disks and dried for 20 min. To obtain a uniform GO-modified Zn surface, the GO slurry was applied one more time, especially the parts that have not yet been covered with GO. Finally, the GO-modified Zn mesh was dried at room temperature in air.

Preparation of Ni cathodes. To evaluate the electrochemical performance of GO-modified Zn anode, Ni cathodes harvested from commercial Ni-Zn AA batteries were used as the rechargeable cathode. Before cell assembly, Ni cathodes were electrochemically oxidized to 0.6 V vs HgO/Hg reference electrode in a beaker cell with 2 M KOH as the electrolyte, to completely turn $Ni(OH)_2$ to NiOOH.

Assembly of coin-type rechargeable Zn-Ni batteries. The coin-type batteries were assembled using CR2032 cases (MTI Corporation), the Zn mesh anodes or Zn@GO anodes (round disk, 1 cm diameter) and NiOOH cathodes with excess capacity. Glass fiber was used as the separator. 50 µL electrolyte was added onto each separator. The aqueous electrolyte consists of 4 M KOH, 2 M KF and 2 M K_2CO_3. An MSK-110M hydraulic sealing machine was used to seal the battery.

Materials characterization and electrochemical testing. X-ray photoelectron spectroscopy (XPS), X-ray diffraction (XRD), Scanning Electron Microscopy (SEM) and Transmission Electron Microscopy (TEM) at Institute for Electronics and Nanotechnology (IEN) were used to characterize the GO and anodes. The cycle life and capacity of batteries were measured by using a LAND battery tester. All the cells were galvanostatically cycled between 1.5 V and 1.9 V at a constant current of 1 mA with 1 h limit. Electrochemical impedance spectroscope (EIS) measurements were performed on a Bio-Logic instrument.

14

The frequency range was between 100 KHz and 10 mHz. The amplitude of AC signal was 10 mV.

2.1.3   Results and Discussion

As shown in Figure 2.2a, high quality GO with nano thick GO layers was successfully synthesized. Then GO slurry was applied on Zn mesh (Figure 2.2b). The comparison between Figure 2.2c and Figure 2.2f shows that GO has been coated onto the Zn mesh uniformly. By comparing Figure 2.2d and Figure 2.2g, it was found that the GO coating is ~ 4 μm thick with a 0.19 mg/cm^2 GO coating, which is 1.92 wt% of a Zn mesh. Under optical microscope, Zn mesh looks shiny (Figure 2.2e), and after GO coating, it turns uniformly dark in color and rough in texture (Figure 2.2h). The complete coverage of Zn by GO is supported by XPS results (Figure 2.2i and Figure 2.2j), where the Zn signal is barely detectable from Zn@GO. XRD patterns (Figure 2.2k) of unmodified Zn and Zn@GO anodes show same ZnO peaks, which indicate the amorphous nature of GO.
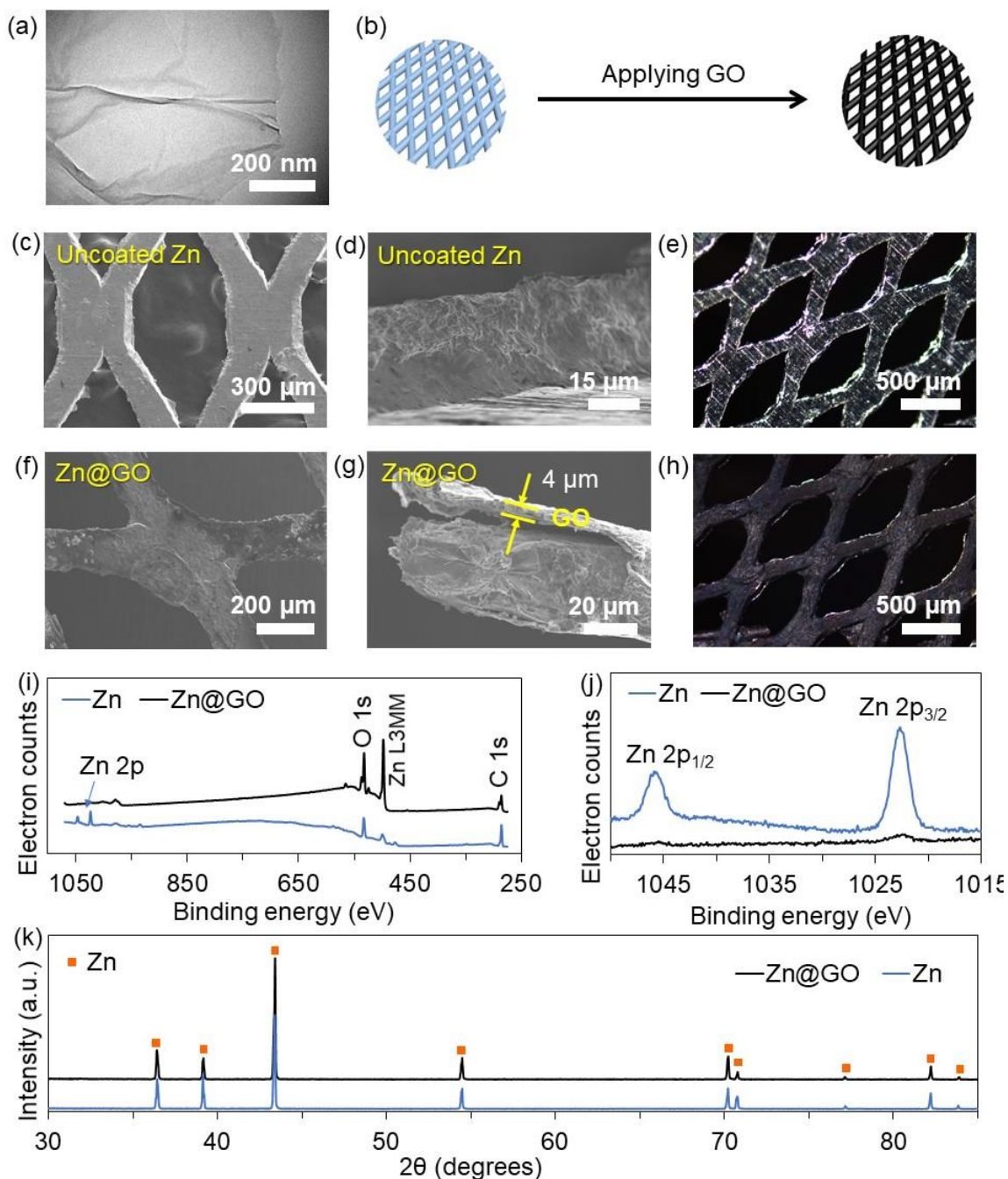
Figure 2.2 - Fabrication and characterization of anodes. (a) TEM image of GO. (b) Schematic of the fabrication process. (c) Top-view SEM image of Zn mesh. (d) Cross-section SEM image of Zn mesh. (e) Optical microscopy image of Zn mesh. (f) Top-view SEM image of GO modified Zn mesh. (g) Cross-section SEM image of GO modified Zn mesh. (h) Optical microscopy image of GO modified Zn mesh. (i) XPS survey of Zn mesh and GO modified Zn mesh. The C peak of Zn mesh is from the carbon tape under the Zn metal, which was used to fix the Zn mesh. (j) High-resolution Zn 2p spectra of Zn mesh and GO modified Zn mesh. (k) XRD results of Zn mesh and GO modified Zn mesh.

To verify the function of GO coating, Zn anodes were assembled with NiOOH cathodes in coin-type cells, discharged and charged for 10 times, and opened for characterization. As shown in Figure 2.3a and b, the structure of the unmodified Zn mesh anode collapsed after cycling. In contrast, the shape of the Zn@GO anode remained after cycling (Figure 2.3c and d), which means that the GO coating has effectively stabilized the Zn anode. This is also an evidence that GO blocks zincates and encapsulates insulating discharged product ZnO (Figure 2.3e), so electrons can be delivered across insulating ZnO. These morphological observations confirmed the hypothesis that thin and uniform GO coating could address the problems of Zn metal anode.
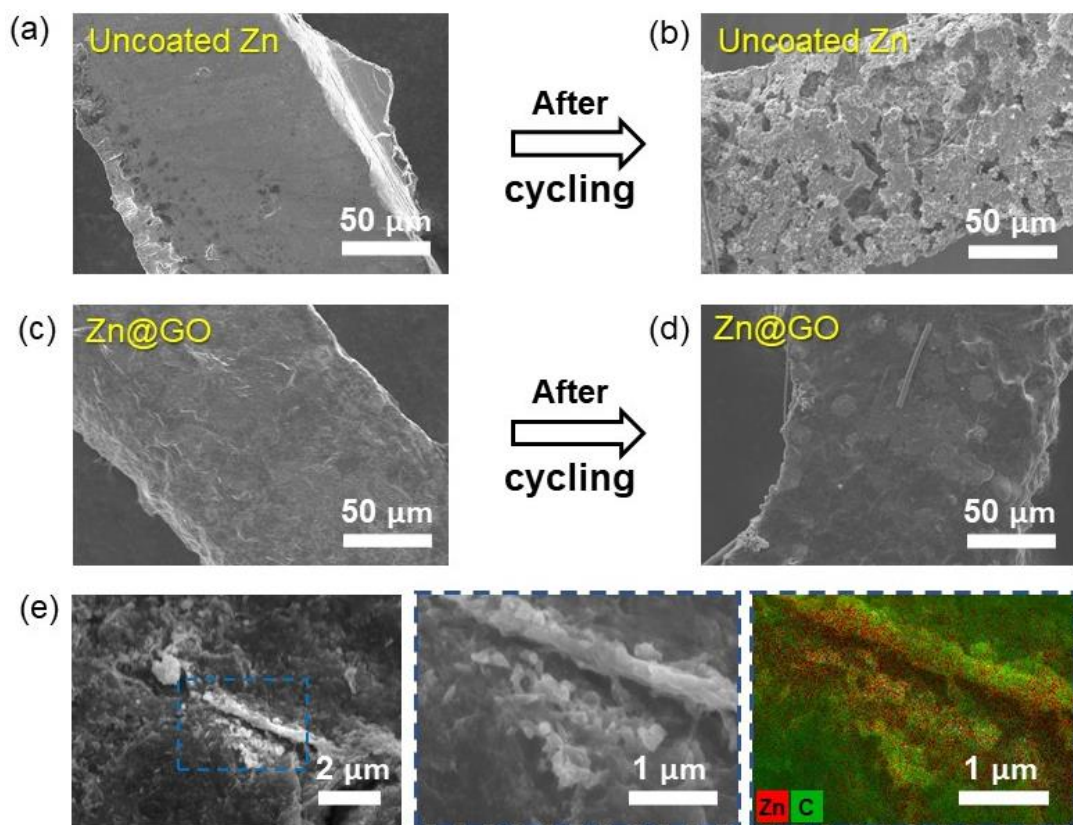
Figure 2.3 - Characterization of anodes before and after 10 galvanostatic cycles. (a) SEM image of unmodified Zn anode before cycling. (b) SEM image of unmodified Zn anode after cycling. (c) SEM image of Zn@GO anode before cycling. (d) SEM image

of Zn@GO anode after cycling. (e) SEM images and EDS mapping of the Zn@GO anode after cycling.

Conventionally, beaker cells are used to examine the electrochemical performance of Zn-based batteries. Yet the large amount of electrolyte (ZnO saturated KOH solution) required by beaker cells significantly decrease the overall specific energy. Also, zincates in the electrolyte can participate in the reaction and conceal the true performance of Zn electrodes. Hence, coin-type cells were chosen here to evaluate the performance of GO-modified Zn anode in a way that resembles practical applications, as shown in Figure 2.4a. The areal density of the Zn mesh is 10.05 mg/cm^2. If discharged in a primary cell, its theoretical capacity is 8.24 mAh/cm^2. In the rechargeability testing, its discharge capacity was limited to 1.27 mAh/cm^2 by limiting its discharge time to 1 h. As shown in Figure 2.4b, the battery assembled using Zn@GO anode with 0.19 mg/cm^2 GO coating displayed its superiority over the one assembled using bare Zn mesh anode. At the 20th galvanostatic cycle, the reversible discharge areal capacity of the Zn@GO anode is ~118% of that of the bare Zn anode. The accumulated discharge capacity of GO-modified Zn anode (61.5 mAh/cm^2) is 128% of that of bare Zn anode (47.9 mAh/cm^2, Figure 2.4c) for the first 200 galvanostatic cycles. The voltage in the charging step of the Zn@GO anode is slightly lower than that of bare Zn anode at the 20th galvanostatic cycle, which means that the Zn@GO anode has lower overpotential (Figure 2.4d). The performance of Zn@GO anodes were also tested with lower and higher amount of GO coating, respectively. The effect of low amount of GO coating is not evident because GO is not enough to cover the Zn surface. High amount of GO coating makes the performance worse because thick GO hinders the contact of electrode and electrolyte, which hinders the electrochemical reaction.

Electrochemical impedance spectroscopy (EIS) was employed to investigate the influence of GO modification on the impedance. The Nyquist plots of the GO-coated and bare Zn anodes before and after 10 galvanostatic cycles (1 mA for 1 min per cycle) are shown in Figure 2.4e. The initial charge-transfer resistance of GO-coated Zn anode is lower than that of the uncoated Zn anode. After cycling, the impedance of both anodes decreases, yet that of GO modified Zn anode is still smaller. For Zn@GO anode, the impedance decreased after cycling because GO was partially reduced in alkaline electrolyte. For Zn anode, the zincates disperse surrounding the surface of Zn after cycling, which decreased the charge-transfer resistance. These observations indicate that GO improves the electrochemical performance of the original Zn anode, which can be attributed to a uniform distribution of ZnO among GO layers during the electrochemical reactions. This extends the cycle life of Zn-based batteries by both creating a desirable environment for electrons to transport freely and slowing down the inevitable dissolution process of active anode materials.
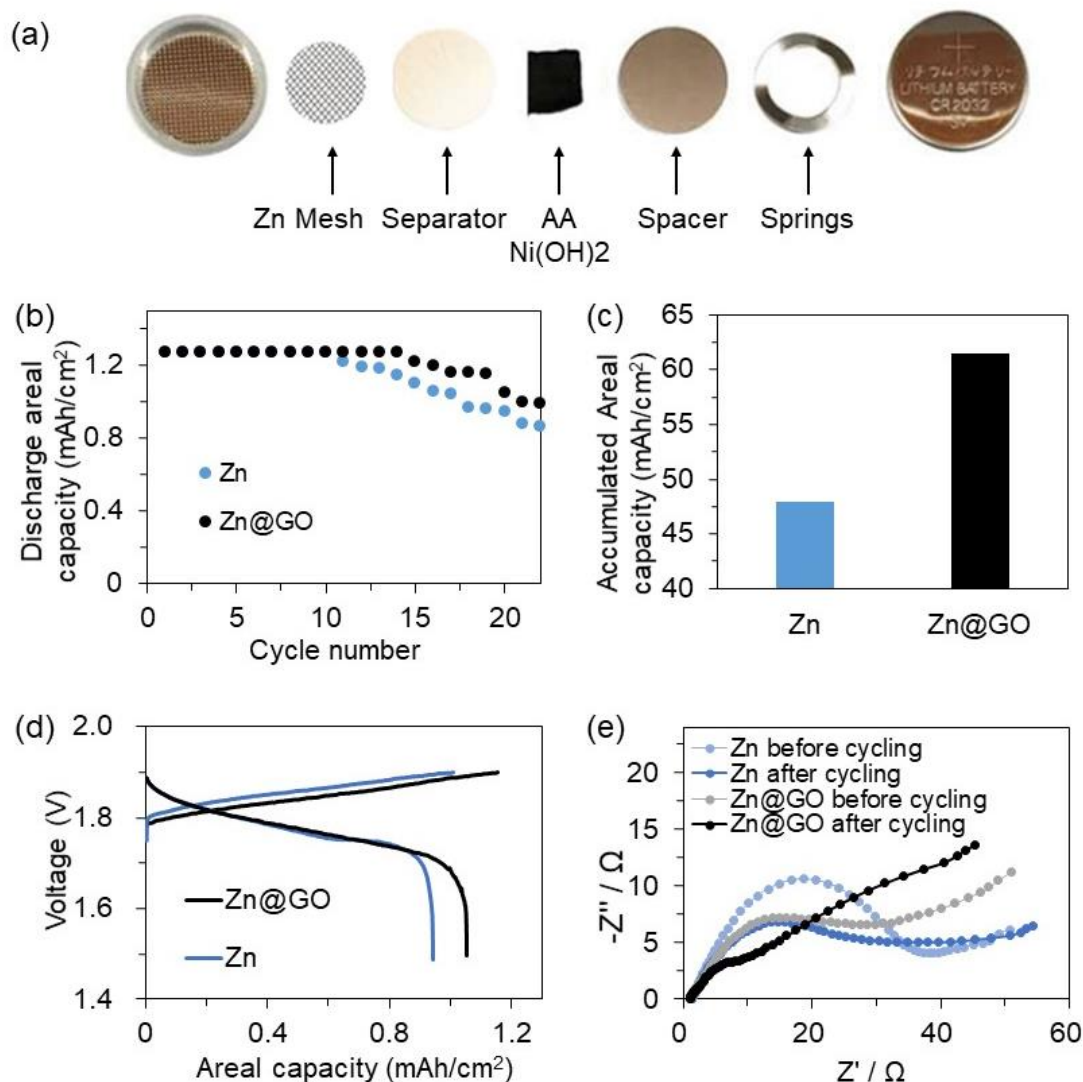
Figure 2.4 - Electrochemical performance of anodes. (a) Optical picture of the coin cell assembly. (b) Discharge areal capacity for the first 22 galvanostatic cycles of bare and GO-modified Zn anodes. (c) Accumulated discharge areal capacity of bare and GO-modified Zn anodes for the first 200 galvanostatic cycles. Accumulated discharge areal capacity is calculated by adding the discharge areal capacity of all cycles together. (d) Voltage profiles of the 20th galvanostatic cycle of bare and GO-modified Zn anodes. (e) Nyquist plots of the bare and GO-modified Zn anodes before and after cycling.

2.1.4   Conclusion

A GO-modified Zn anode was reported to solve the passivation and dissolution problems of Zn anodes, and extend the cycle life of Zn-based batteries. The Zn surface is

20

modified by applying GO slurry onto Zn mesh uniformly. The GO layers on Zn surface allow electrons to move freely across the insulating ZnO and reduce the dissolution rate of Zn intermediate species. As a result, a small amount of GO (1.92 wt%) on the Zn anode surface can significantly reduce the electrochemical impedance, and improve its life-time accumulated capacity by 28%. This GO modification approach is expected to be applicable to other battery electrodes as well.

2.2   Lasagna-Inspired Nanoscale Zn Anode

2.2.1   Introduction

Bulk zinc foil or mesh have been used as typical anode materials of aqueous Zn batteries. Upon discharging, insulating ZnO product forms on the zinc foil electrode surface and passivates unreacted Zn underneath, limiting the Zn utilization and rechargeability (Figure 2.6a). After cycling, Zn metal anodes (25 µm in thickness) had a ZnO passivation layer with typical thickness of ~ 2 µm (Figure 2.5). Thus, it was hypothesized that the critical size of passivation is ~ 2 µm. When the feature size of Zn/ZnO is sufficiently small (e.g. sub-micron), other conditions kept the same, the reversibility of Zn/ZnO conversion could potentially be enhanced. Micro-structured Zn metal with large surface area has improved rechargeability in coin-type cells,[79,92] yet the depth-of-discharge (DOD) still has to be limited under 40% to prevent passivation and maintain activity.
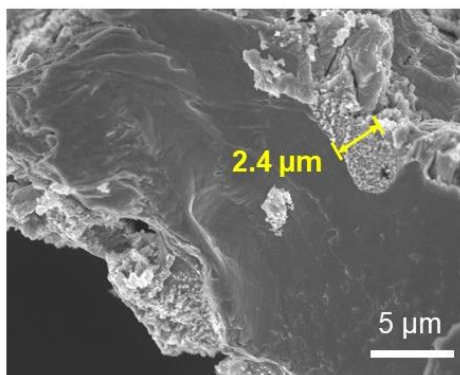
Figure 2.5 - SEM image of ZnO passivation layer on Zn mesh (Dexmet), formed by discharging Zn mesh under 1 mA with 10 μL electrolyte. Separator used here was Celgard 3501.

Decreasing the feature size of zinc-based anode to below the critical size of passivation is possible by starting with nanostructured ZnO, which can be synthesized by a wide gamut of approaches.[93] It is also feasible to combine nanosized ZnO with conductive additives in a composite, to facilitate electron transport to insulating ZnO and enable its conversion to Zn during charging. However, nanostructured ZnO could exacerbate the dissolution problem due to the enlarged electrode-electrolyte interface.[94] As shown in Figure 2.6b, ZnO dissolution will change the structure of the electrode, and the spreading of $Zn(OH)_4^{2-}$ will lead to the loss of the active material and a quick decay in capacity over cycling. To mitigate problems caused by ZnO dissolution, electrodes were tested in beaker cells with excess amount of electrolyte saturated with $Zn(OH)_4^{2-}$ for most past reports.[95–98] Yet, the large electrolyte/electrode ratio makes the overall energy density extremely low and deviates from practical operating condition. Also, Zn species from the electrolyte could also behave as active material during testing, making it impossible to evaluate the true performance of Zn electrodes.

22
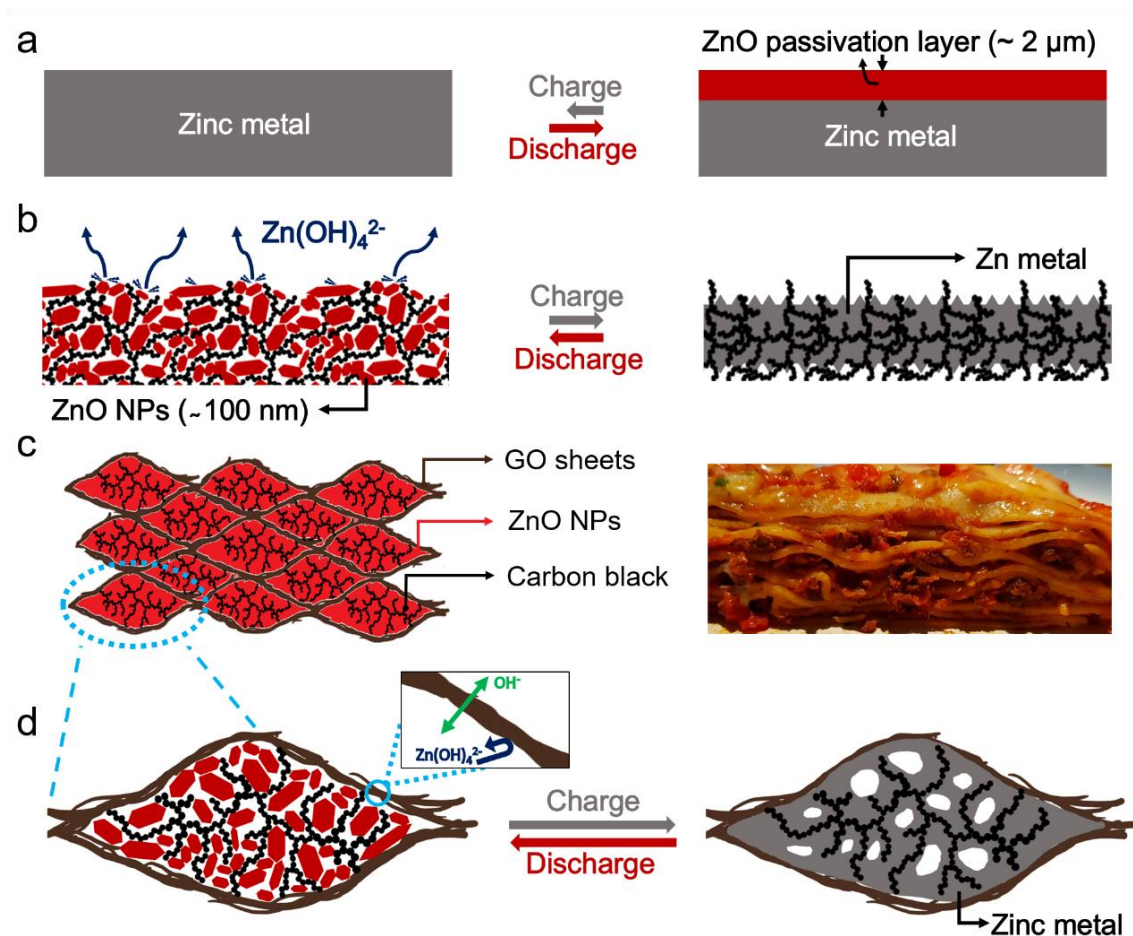
Figure 2.6 - Schematic of changes that occur in zinc-based electrodes during electrochemical cycling in alkaline aqueous electrolyte. (a) Bulk zinc metal anode tends to stop discharging ("passivated") after discharge product ZnO reaches a thickness of ~ 2 μm, resulting in limited utilization. (b) ZnO nanoparticles have diameter (~100 nm) smaller than the critical passivation size, yet enlarged surface area, and the absence of confinement leads to the escape of ZnO and morphology change of the electrode. (c) ZnO lasagna microstructure comprising ZnO nanoparticles and carbon black encapsulated by graphene oxide sheets (left), and a real lasagna (right). (d) Schematic of a single capsule inside the ZnO lasagna electrode. The graphene oxide (GO) sheets confines $Zn(OH)_4^{2-}$ inside the capsule, while allows smaller OH^- and H_2O to permeate. Stable GO framework and confined ZnO maintain the electrode morphology after cycling.

Here, a lasagna-inspired Zn anode was reported, in which ZnO nanoparticles are encapsulated by graphene oxide (GO) to form a free-standing film, to simultaneously solve the passivation and dissolution problems of aqueous Zn anode (Figure 2.6c, d). ZnO lasagna structure has three features: 1) the size of ZnO nanoparticles is smaller than the

23

critical size of passivation; 2) the fabrication of ZnO lasagna anode starts with commercially available ZnO nanoparticles (~100 nm), and is compatible with the roll-to-roll process, which is ideal for large-scale manufacturing; 3) GO allows permeation of OH^- and water,[99,100] and prevents loss of Zn active material through blocking bigger $Zn(OH)_4^{2-}$.[101] And GO can be partially reduced when soaked into alkaline electrolyte,[77,89] which can facilitate electron transfer inside anodes. The transmission electron microscopy (TEM) image (Figure 2.7a) and Raman spectra (Figure 2.7c) shows the high-quality GO sheets with characteristic peaks of D and G bands at 1363 and 1589 cm^{-1}, respectively. Zn active material is confined inside the GO framework, which is stable during electrochemical cycling. The blocking of $Zn(OH)_4^{2-}$ is attributed to 1) geometric confinement and 2) electrostatic repulsion. First, H_2O and OH^- have solvodynamic radii of 0.138 and 0.110 nm,[102] which allows unrestrained permeation through the nanochannels between adjacent GO nanosheets.[99] But $Zn(OH)_4^{2-}$ has an average hydrated radii of 0.330 nm,[103] which is too big for it to transport through the nanochannels.[101,104] Second, GO carries negative charges because of the oxygen functional groups (e.g. carboxyl). $Zn(OH)_4^{2-}$ ions inside the GO capsule have an electrostatic barrier to cross before they could escape out.

2.2.2   Experimental Section

Materials and chemicals. Zn metal (0.25mm thick, 99.98%, Alfa Aesar), zinc oxide nanoparticles (ZnO, ~100 nm, Sigma-Aldrich), water binder (BTA-520L, MTI), alginic acid sodium salt (Alfa Aesar), carbon black (Super-P, Timcal), graphite powder (MTI), hydrogen peroxide (H_2O_2, 30% wt. % in H_2O, Sigma-Aldrich), sulfuric acid (H_2SO_4, 95.0-98.0%, Sigma-Aldrich), potassium permanganate ($KMnO_4$, 97%, Sigma-Aldrich), Soil water crystal beads (hydrogel beads, Eboot Online), potassium hydroxide

(KOH, 99.97%, Sigma-Aldrich), potassium fluoride (KF, 99.9%, Sigma-Aldrich), potassium carbonate (K_2CO_3, 99.0%, Sigma-Aldrich), copper foil (37 µm, single side polished, Shenzhen Jingliang Copper Co., Ltd.), tin foil (25 µm, Alfa).

Synthesis of graphene oxide. GO was synthesized from graphite using a modified Hummers' method.[90] A pretreatment step was used to avoid the formation of inadequate oxidized graphite-core/GO-shell particles.[91] The pretreated graphite powders were added into 120 mL concentrated H_2SO_4 solution under stirring in an ice bath. 15 g $KMnO_4$ was then slowly added under stirring, keeping the temperature below 10°C. After adding $KMnO_4$, the beaker was heated to 35°C and maintained for 45 min, followed by drop-by-drop addition of 200 mL deionized water (DI-water). Next, the beaker was heated to 98°C and maintained for 15 min, followed by addition of another 700 mL DI-water. Finally, 20 mL 30% H_2O_2 was gradually added to the mixture to decompose unreacted $KMnO_4$ and insoluble MnO_2, the resulting dispersion turned to bright yellow. To work out the GO, the dispersion was subjected to centrifugation (7000 rpm, 15 min). The resultant sediment was washed with DI-water for 5 times until the pH of the supernatant reached neutral. The resulting GO was dispersed into DI-water and sonicated for 2 hours, followed by centrifugation (4000 rpm, 15 min). The clear supernatant is the aimed aqueous GO dispersion (~1 g/L). To further get GO powders, the above GO dispersion was concentrated to 2 g/L using hydrogel beads, followed by freeze-drying.[105]

Preparation of Zn anodes. ZnO lasagna (ZnO/GO/carbon black) anode on metal current collectors was synthesized as followed process. ZnO lasagna slurry was prepared first. Typically, 15.0 mL DI-water was added into a glass vial (20 mL) containing 72.0 mg water binder and 18.0 mg alginic acid sodium salt, followed by vigorous stirring to form

Solution A. Then 2.50 mg GO powder was dispersed into 0.500 mL Solution A under vigorous stirring to form Slurry B. Substantially, 20.0 mg ZnO nanoparticles and 2.50 mg carbon black were added into the well-mixed Slurry B, followed by one hour of ultrasonication and six hours of stirring at room temperature. The obtained ZnO lasagna slurry, containing ZnO nanoparticles, graphene oxide, carbon black and binder with a weight ratio of 8:1:1:1.2, was ready for casting electrodes. 75 µL ZnO lasagna slurry was dropped on the rough surface of a round Cu disk (37 µm in thickness, 1 cm in diameter) and dried at room temperature. The same process was done on Sn disks (25 µm in thickness, 1.0 cm in diameter) as well. The average thickness of the film after calendering was 5.11 µm. ZnO particle anode on metal current collectors was synthesized through the same process, containing ZnO nanoparticles, carbon black and binder with a weight ratio of 8:2:1.2. And the synthesis of free-standing ZnO anode can be found in the Supporting information.

Battery assembly. Two kinds of ZnO anodes with metal current collectors were assembled in 2032 coin-type cells with $Ni(OH)_2$ cathodes from discharged commercial cylindrical Ni-Zn rechargeable batteries (PowerGenix) as counter/reference electrodes, Whatman glass fiber filter as separators, and 100 µL ZnO-free alkaline electrolyte. The electrolyte was 4.0 M KOH, 2.0 M KF, and 2.0 M K_2CO_3 aqueous solution. ZnO metal and four kinds of free-standing ZnO anodes were assembled in 2032 coin-type cells with Sn foil (25 µm in thickness, 1.0cm in diameter) as the current collector. The counter electrode, separator and electrolyte were the same as former assembly process.

Electrochemical test. All electrochemical testing was performed using LAND CT2001A 8 channels battery testers. Coin cells containing Sn current collector supported

ZnO anodes were galvanostatically cycled between 1.45 and 2.00 V (charged at 1C rate, discharged at 5C rate). The specific capacity of anode was calculated based on the weight of ZnO inside the anode. The charging/discharging rate was calculated with respect to the theoretical capacity of ZnO (658 Ah/kg). Coin cells containing Zn metal anode were galvanostatically cycled between 1.40 and 1.90 V. Coin cells containing Cu current collector supported ZnO anodes were galvanostatically cycled between 1.40 and 2.00 V (charged at 1C rate, discharged at 1C rate). Coin cells containing free-standing ZnO anodes were galvanostatically cycled between 1.40 and 1.95 V.

Material characterization. To characterize the Zn anodes after cycling, coin-type cells were first cycled 40 times, and opened immediately. Then the Zn anodes were gently cleaned with DI-water to remove the electrolyte and glass fiber. The SEM images were obtained using HITACHI SU8230 with a 10 KV accelerating voltage. The samples for cross-sectional imaging were placed between two pieces of silicon wafer, and attached to a vertical stage with carbon tape. The XRD patterns were collected using Panalytical Empyrean, with Cu K(α), which is 1.5425 Å in wavelength. The Raman spectrum was collected using Thermo Nicolet Almega XR Dispersive Raman Spectrometer, with 785 nm laser.

2.2.3   Results and Discussion

A facile and scalable process to fabricate lasagna-like ZnO anode was developed, either on metal current collectors or as free-standing foil. For metal-supported ZnO lasagna, ZnO nanoparticles were mixed with graphene oxide, carbon black and binder (8:1:1:1.2 by weight) in water to form a slurry, which is then casted on tin or copper foil.

27

Both sides of metal foil can be coated to form an electrode similar to the one used in cylindrical cells. For free-standing ZnO lasagna, the weight percentage of binder was increased to enhance mechanical strength. This process is compatible with roll-to-roll manufacturing and can be easily scaled up. Figure 2.7b shows a large free-standing ZnO lasagna foil (10 cm × 5 cm).

The successful fabrication of ZnO lasagna anode was supported by various characterization. Raman spectrum (Figure 2.7c) confirms the D and G peaks of the GO inside the ZnO lasagna. X-ray diffraction (XRD) pattern of ZnO lasagna contains peaks of ZnO (wurtzite) (Figure 2.8). Low-magnification cross-section scanning electron microscope (SEM) image of the free-standing ZnO lasagna (Figure 2.7d) shows that the components were well mixed. In high-magnification image (Figure 2.7d, inset), ZnO nanoparticles and carbon black are visible in the graphene oxide framework. ZnO nanoparticles aggregate to form clusters, mix well with carbon black, and together encapsulated by graphene oxide. The GO encapsulation design is critical for slowing down dissolution of ZnO in alkaline electrolyte and extending cycle life. In further evaluation of the merit of ZnO lasagna electrodes, they are compared with open-structured ZnO particle electrodes made of ZnO nanoparticles, carbon black and binder (Figure 2.9). The structure consists of simply connected particles, without any encapsulation (Figure 2.8, inset).
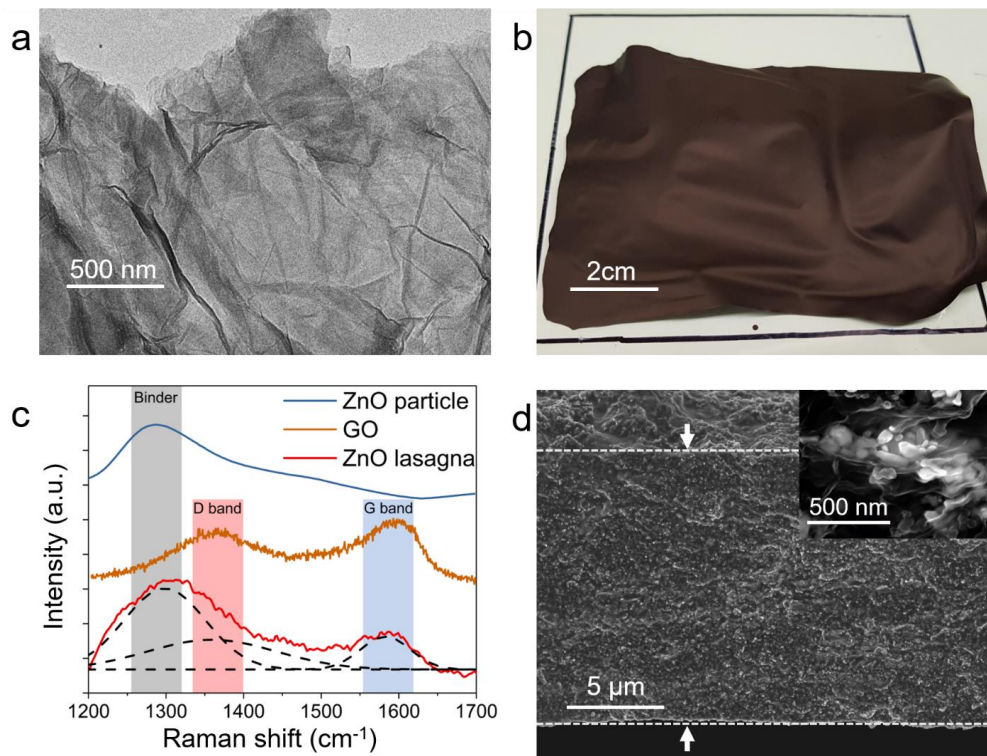
Figure 2.7 - Characterization of the synthesized ZnO lasagna electrodes. (a) Low magnification TEM image of the overlapped graphene oxide sheets. (b) Optical image of a large (10 cm × 5 cm) freestanding ZnO lasagna electrode. (c) Raman spectrum of the ZnO particle, GO and ZnO lasagna. Dashed curves are the fit peaks of ZnO lasagna. (d) Low and high magnification (inset) cross-section SEM images of the ZnO lasagna electrode. The dash lines and arrows indicate the top and bottom surfaces of the electrode.
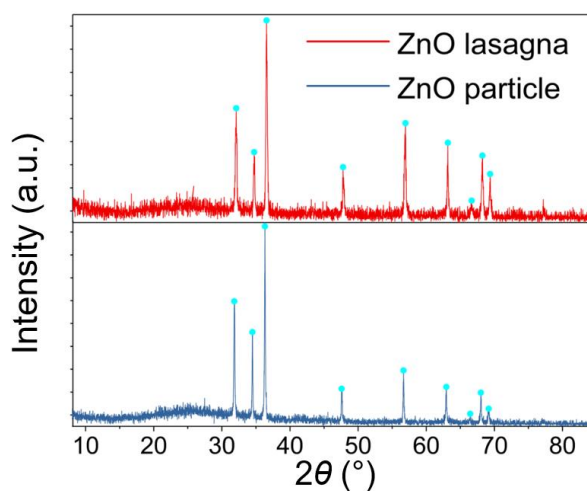
Figure 2.8 - XRD patterns of ZnO lasagna and ZnO particle anodes. The peaks marked by cyan dots belong to ZnO with hexagonal close packing (hcp) structure.
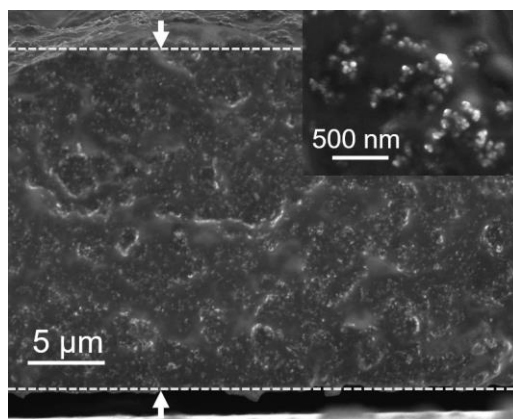
Figure 2.9 - Low and high magnification (inset) cross-sectional SEM images of the ZnO particle electrode. The dash lines and arrows indicate the outline of the electrodes.

To examine the ability of graphene oxide framework in encapsulating $ZnO/Zn(OH)_4^{2-}$ inside the electrode, a ZnO lasagna anode and a ZnO particle anode (both have the size of 3.0 mm $\times$ 3.0 mm) were soaked separately in 0.30 mL of electrolyte, and measured Zn concentration in both solutions over time using inductively coupled plasma atomic emission spectroscopy (ICP-AES). Compared with 4 M KOH, 2 M KF, 2 M K_2CO_3 electrolyte, ZnO solubility is higher in 4 M KOH solution.[106] For better differentiating the two ZnO anodes, 4 M KOH was used in the dissolution test. After 14 days of soaking, the severe ZnO loss of ZnO particle anode disintegrated the electrode, the detached electrode fragments turned the solution dark and turbid (Figure 2.10a, right). In contrast, ZnO lasagna anode remains almost the same after 14 days (Figure 2.10a, left). In addition, over the 14 days, 10 µL clear solution was drew from each tube every other day to analyze the dissolved Zn concentration and added 10 µL of 4 mol/L KOH aqueous solution back to maintain same volume. In addition, the Zn concentration measured by ICP-AES shows the huge difference between two anodes, from which the percentage of dissolved Zn (Figure 2.10b) was calculated. Based on the calculation, 6.8% of ZnO inside the ZnO lasagna

electrode was dissolved in the first week (six days), and 15.5% after two weeks. Yet for

ZnO particle electrode, about half of ZnO inside was dissolved after the first week, and

68.5% after two weeks (4 times more than ZnO lasagna). Because a large electrolyte :

active materials ratio (~25 times larger than in coin cell) was applied, which speeds up the

dissolution, the amount of dissolved ZnO is high for both anodes. These results suggest

that, due to the encapsulation of graphene oxide, ZnO in lasagna-structured anode is much

more resistant to dissolution than ZnO in the open structure anode. The nanoscale lasagna

structure is effective in keeping active material, $ZnO/Zn(OH)_4^{2-}$, inside the electrode.
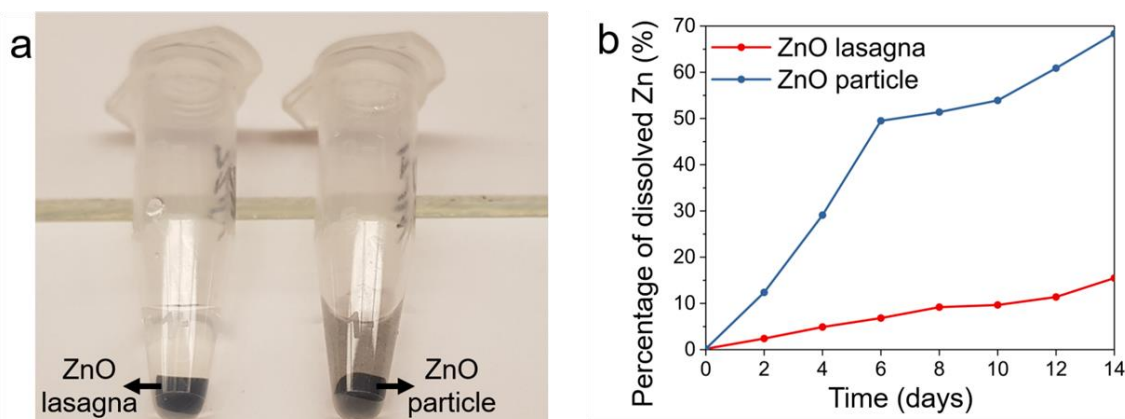
Figure 2.10 - Suppression of ZnO dissolution with nanoscale lasagna structure. (a) Pictures of ZnO lasagna (left) and ZnO particle (right) electrodes that have been soaked in 4 mol/L KOH aqueous solution for 14 days. (b) Percentages of ZnO that has been dissolved in solution over time, measured using inductively coupled plasma atomic emission spectroscopy (ICP-AES). After 14 days, 68.3% of ZnO in open structured electrode was dissolved, while only 15.5% ZnO in lasagna structured electrode was dissolved.

The electrochemical performance of ZnO lasagna anodes was evaluated in sealed

coin-type batteries with $Ni(OH)_2$ cathodes containing excessive capacity (Figure 2.11).

Open-structured ZnO particle anodes were tested in the same way for comparison, and the

charge capacity was limited to the theoretical capacity of ZnO (658 Ah/kg). Both upper

and lower voltage limits were set. Figure 2.11a shows the cycle performance and

Coulombic efficiency (CE) of tin-supported anodes. The capacity increase of both anodes around 45 cycles can be attributed to the slow activation of the commercial $Ni(OH)_2$ cathodes in the beginning of electrochemical cycling.[107–109] The capacity decrease might be caused by the electrolyte dry and bubble accumulation because of hydrogen evolution. The open-structured ZnO particle anode quickly decayed after 75 cycles and completely degraded after 95 cycles (Figure 2.11a), because the loss of unprotected active material, which is indicated by the ICP-AES results shown above. In contrast, ZnO lasagna anodes (Figure 2.11b) showed excellent electrochemical performance. At 100% DOD, its discharge capacity reached 586 Ah/kg after the cathode activation and remained above 565 Ah/kg for 150 cycles (Figure 2.11a). The high performance of ZnO lasagna anode is attributed to the confinement of $Zn(OH)_4^{2-}$ inside the electrodes by GO sheets' geometric encapsulation and electrostatic repulsion. Notably, the practical volumetric capacity of ZnO lasagna anode reached 2308 Ah/L. When taking current collector (25 µm tin foil) into account, volumetric capacity is 441 Ah/L, which is similar to the state-of-the-art 3D-Zn sponge anode (423 Ah/L).[79,92] And to notify that this number 2308 Ah/L is much higher than graphite anode in Li-ion batteries,[110] even higher than Li metal, rendering safe and high-energy Zn-based batteries a promising alternative to Li-ion batteries for large-scale energy storage.

The ZnO lasagna anode was recovered from coin cells after 40 cycles and examined under SEM. As shown in Figure 2.11c, the thickness and morphology of the cycled ZnO lasagna anode were almost identical as the pristine one. High magnification SEM images (Figure 2.11d, e) showed that the nanoscale lasagna structure (ZnO encapsulated by GO framework) was maintained after electrochemical cycling. In contrast, the morphology of

ZnO particle anode completely changed after 40 cycles (Figure 2.11f, g). The former dense structure became porous one due to the rearrangement of the unprotected ZnO and carbon black, resulting from the dissolution and deposition of ZnO during cycling. The morphology change of ZnO particle anodes, along with the continual active material loss, led to low cyclability.
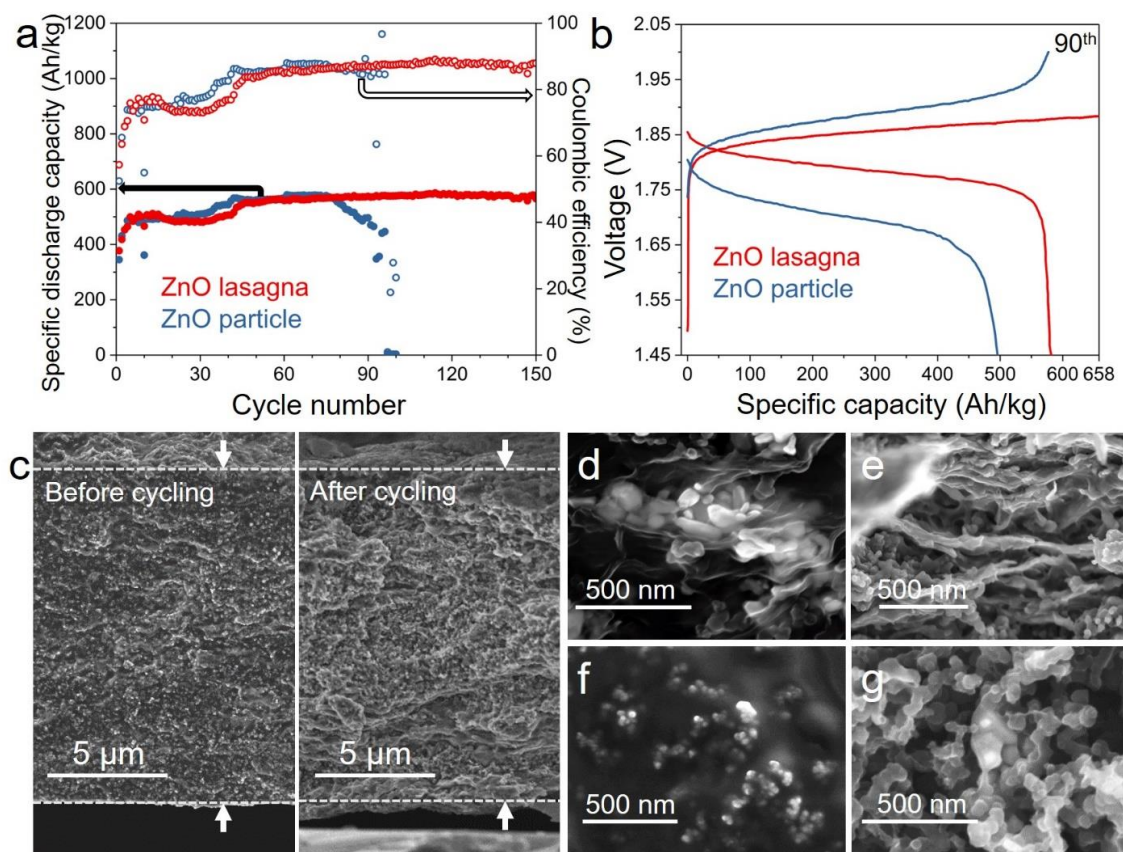
Figure 2.11 - Electrochemical performance of Zn lasagna anodes. The cells were galvanostatically cycled between 1.45 and 2.00 V, at 1C rate for charging and 5C for discharging. The mass loading of ZnO was ~ 1 mg/cm². (a) Cycling performance and Coulombic efficiency, and (b) voltage profiles of 90th cycle of tin-supported ZnO lasagna and ZnO particle anodes. (c) Cross-section SEM images of the ZnO lasagna before (left) and after 40 cycles (right). (d, e) High-magnification cross-section SEM images of the ZnO lasagna anode before (d) and after (e) 40 cycles. (f, g) High-magnification cross-section SEM images of the ZnO particle anode before (f) and after (g) 40 cycles.

With encapsulation structure, ZnO lasagna anodes slow down the loss of active materials, maintain electrode morphology, and out-performs open-structured ZnO anodes. While longer cycle life for Zn anode have been reported in beaker cells or neutral electrolytes, the performance of ZnO lasagna is among the best obtained in coin cell and ZnO-free alkaline electrolyte.

2.2.4 Conclusion

In summary, a lasagna-inspired nanostructure was designed to solve simultaneously the passivation and dissolution problems of aqueous Zn anode and developed a facile and scalable approach to synthesize it. With geometric confinement and electrostatic repulsion of graphene oxide sheets towards $Zn(OH)_4^{2-}$, the active material is confined inside the electrodes during electrochemical cycling. ZnO lasagna anode achieved a high cycling-available volumetric capacity of 2308 Ah/L, even higher than lithium metal, as well as long cycle life (> 150 cycles) and a high specific capacity in coin-type cells and ZnO-free alkaline electrolyte. This work demonstrated the effectiveness of nanoscale structure design in addressing intrinsic passivation and dissolution problems of Zn anodes in alkaline electrolyte, the design principles can possibly be extended to enable other soluble active materials (e.g. sulfur) for future high-energy and safe batteries.

2.3 Sealed ZnO Nanorod Anode

2.3.1 Introduction

As mentioned above, Zn metal foil is the most commonly used Zn anode in aqueous batteries. However, the passivation problem (nonconductive property of ZnO) of Zn foil

34

limits the utilization (<1%) of Zn foil anode and makes it non-rechargeable (Figure 2.12a).

Under 10 mA discharge, only 1.7 mAh capacity of Zn foil can be gotten with 0.25 mm

thickness and 1 cm diameter in coin cell (Figure 2.13). The thickness of the passivation

layer (or the critical passivation size) is ~ 2 µm. Microporous Zn sponges[79,111,112] have been

made to enhance the rechargeability, yet its feature size is ~ 10 µm (> 2 µm), so only 40%

DOD of them can be achieved. Sub-micron-sized Zn anodes[96–98,113] including ZnO

nanoplates[114] and ZnO nanoparticles[74] are also investigated. However, the anode

dissolution problem, resulting from large electrode-electrolyte surface area[94] of these sub-

micron-sized Zn anodes, is not well controlled or clearly stated. The lasagna-inspired Zn

anode[78] can address the passivation problem initially. However, the feature size of ZnO

would be larger than the critical passivation size (~2 µm) after cycling due to its structure

degradation.

a   Zn foil

Charge ⇄ Discharge

~2 μm↓ ← Passivation layer
ZnO
Zn foil

b   ZnO nanorod anode

Complexation

$Zn(OH)_4^{2-}$ ~200 nm

Carbon paper

Charge →

Electroreduction

$Zn(OH)_4^{2-}$

Carbon paper

c   ZnO@TiN$_x$O$_y$ nanorod anode

Complexation/Precipitation

Block $Zn(OH)_4^{2-}$

Carbon paper

Charge ⇄ Discharge

Electroreduction/Electrooxidation

Zn metal

OH⁻   e⁻

Mechanical backbone

Electrical pathway

Carbon paper

Figure 2.12 - Schematic of morphological changes of zinc electrode during electrochemical cycling. a, Zn foil shows very low utilization (<1%) because of ZnO passivation layer. The critical passivation size is ~ 2 μm, as shown above. b, The feature size of ZnO nanorod is smaller than the critical passivation size, however, the large electrode-electrolyte surface area accelerates anode dissolution and promotes electrode shape change. Moreover, due to the relatively insulating property of ZnO, electrons can only be distributed on carbon paper, which leads to fast complexation and electroreduction reactions on the root of nanorods in charging. As a result, the nanorods will detach from carbon paper. c, The shape of ZnO@TiN$_x$O$_y$ nanorod anode retains during cycling with the sealed nanorod structure.
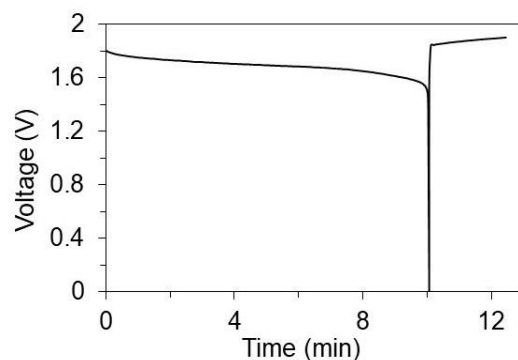
Figure 2.13 - One cycle discharge and charge test for Zn foil under 10 mA, showing that Zn foil can only deliver 1.7 mAh capacity (1% utilization) and charge capacity is only 1/5 of discharge capacity.

Herein, Zn anode's dilemma of passivation and dissolution was solved with a sealed structure (ZnO@TiN$_x$O$_y$ nanorod anode), with feature size smaller than the critical passivation size, and a thin and conformal coating to prevent dissolution of anode (Figure 2.12c). The hydrothermal method[115] was used to grow ZnO nanorods on carbon fiber paper (Figure 2.12b). Then, the atomic layer deposition (ALD) technique was used to form a strong and conductive stable TiN$_x$O$_y$ coating on the ZnO nanorods. This structure has a few advantages: (i) the feature size of ZnO nanorod is smaller than critical passivation size; (ii) the carbon paper framework and TiN$_x$O$_y$ coating, which encapsulates ZnO nanorod, function as an electrical pathway so that all ZnO nanorods are electrochemically active; (iii) the TiN$_x$O$_y$ coating enables fast hydroxide/water diffusion as well as blocks large zincates from escaping during electrochemical cycling, thus prevents anode structure fracture.

2.3.2 Experimental Section

Synthesis of ZnO nanorods. Briefly, carbon paper (Fuel Cell Store) was first heat-treated at 500 °C for 1 h in air to increase its wettability. Then, ZnO nanorods were grown

37

on carbon paper by a wet chemical process. carbon paper was soaked in an aqueous solution containing 0.1 M $KMnO_4$ (Sigma Aldrich) for 1 h to form a seed layer. The seeded carbon paper was then dipped into a glass bottle with a precursor solution containing 50 mL zinc nitrate hexahydrate (30 mM, Alfa Aesar), 50 mL hexamethylenetetramine (30 mM, Sigma Aldrich), and ammonia (28.0-30.0% NH_3 basis, Sigma Aldrich)[115]. The sealed bottle was placed into an oven at 90 °C. After that, the white-colored carbon paper ZnO nanorods was obtained by water washing and drying at 80 °C for 3 h. Different mass loadings of ZnO nanorods on carbon paper ranging from 0.5 mg/cm^2 to 5.5 mg/cm^2 were synthesized by adjusting the carbon paper area per bottle, NH_3 concentration, hydrothermal time and hydrothermal times, as summarized in Table 2.1.

Table 2.1 - Experiment conditions for different mass loadings of ZnO nanorods.

Mass loading	Carbon paper area per bottle	NH_3 quantity	Hydrothermal time	Hydrothermal times
0.5 mg/cm^2	2×(2.1*6) cm^2	2 mL	13 h	1
0.9 mg/cm^2	1×(2.1*6) cm^2	4 mL	22 h	1
5.5 mg/cm^2	1×(2.1*6) cm^2	4 mL	20 h	2

Synthesis of ZnO@TiN$_x$O$_y$ core/shell nanorods. The synthesis of ZnO@TiN$_x$O$_y$ core/shell nanorods was conducted in Cambridge FIJI Plasma ALD system. First of all, the TiN was deposited onto the ZnO nanorods. The precursors of TiN were Tetrakis(dimethylamido)Titanium(IV) (TDMAT, Sigma Aldrich) and N_2. During TiN ALD process, the recipe was run 100 or 200 cycles at 250 °C. The TiN ALD recipe is shown in Figure 2.14. Then, when ZnO@TiN nanorods were exposed to air, the TiN was

partially oxidized to TiN_xO_y (evidenced by XPS spectra in Figure 2.15k). Thus, for accuracy purpose, the anode is named as $ZnO@TiN_xO_y$ in this manuscript.
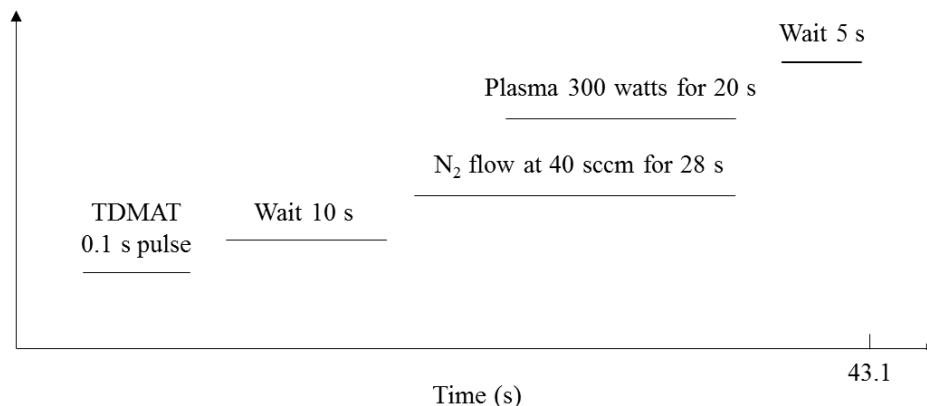
Figure 2.14 - Schematic of TiN ALD recipe.

Electrochemistry. To investigate the Zn anode, full batteries using $Ni(OH)_2$ as the rechargeable cathode were made. The $Ni(OH)_2$ cathodes were harvested from commercial Ni-Zn AA batteries from PowerGenix.

Coin cell: Coin-type batteries were assembled using CR2032 cases (MTI Corporation), zinc anodes (round disk, 1 cm diameter) and $Ni(OH)_2$ cathodes with excess capacity. Coin cell has small volume of electrolyte, which is required for practical application. The aqueous electrolyte consists of 4 M KOH (Sigma Aldrich, 99.99%), 2 M KF (Alfa Aesar, 99.99%) and 2 M K_2CO_3 (Alfa Aesar, 99.997%).[116] Glass fiber (GE Healthcare, Whatman^{TM} 10370003) was used as the separator. For start-stop operation, $ZnO@TiN_xO_y$ nanorod anode and Zn foil were pre-activated. $ZnO@TiN_xO_y$ nanorod anode was pre-cycled three times at 0.5C between 1.4 and 2 V. Zn foil (0.02% DOD) was firstly discharged for 2h and re-charged for 2h at the constant current of 1.35 mA. Then it was discharged twice and charged once at the same time interval of 1 h at 1.35 mA. Zn foil

(1% DOD) was pre-cycled twice at the constant current of 1 mA. When Zn foil was used as the anode, the cathode harvested from commercial Ni-Zn AA batteries was electrochemically oxidized to 0.6 V vs HgO/Hg reference electrode in a beaker cell with 2 M KOH as electrolyte.

Pouch cell: Pouch-type batteries were assembled using Ampac's SealPAK, zinc anodes (round disk, 1 cm diameter) and $Ni(OH)_2$ cathodes with excess capacity. The aqueous electrolyte consists of 4 M KOH (Sigma Aldrich, 99.99%), 2 M KF (Alfa Aesar, 99.99%) and 2 M K_2CO_3 (Alfa Aesar, 99.997%).[116] Celgard 3501 (close to anode) and Freudenberg 700/28K (close to cathode)[79] were used as the separators.

Beaker cell: Beaker-type batteries were assembled using beakers, zinc anodes (round disk, 1 cm diameter) and $Ni(OH)_2$ cathodes with excess capacity. 10 mL ZnO saturated 4M KOH (Sigma Aldrich) was used as the electrolyte.

Electrochemical impedance spectroscope (EIS) measurements were performed on a Bio-Logic instrument. The frequency range was between 100 KHz and 10 mHz. The amplitude of AC signal was 10 mV. Coin-type batteries, assembled using zinc anodes and $Ni(OH)_2$ cathodes were used to measure EIS. 100 µL 4 M KOH, 2 M KF and 2 M K_2CO_3 electrolyte was added to glass fiber separator.

The charge capacity was limited to the theoretical capacity of ZnO (658 mAh/g). The theoretical specific capacity (charge capacity) was calculated by Equation 1.

$$C_T(mAh\ g^{-1}) = \frac{1}{MW} * \frac{nF}{3.6} \qquad (1)$$

where MW is the molar weight of active material, n is the number of electrons transferred in the relevant reaction, and F is the Faraday's constant.

The specific discharge capacity of the electrode was calculated by Equation 2.

$$C = It/m \qquad\qquad (2)$$

where I is the discharge current, t is the discharge time per cycle, and m is active materials' mass. A rate of mC corresponds to a full charge/discharge in 1/m hours.

2.3.3 Results and Discussion

ZnO nanorods are synthesized on carbon paper with mass loading ranging from 0.5 to 5.5 mg/cm^2 (Figure 2.15a-c) by adjusting the area of carbon paper placed in hydrothermal reactor, NH_3 concentration, hydrothermal time, etc.. In ALD process, the recipe was run 100 or 200 cycles. The TiN_xO_y mass loadings of 100 cycles and 200 cycles are about 0.057 mg/cm^2 and 0.19 mg/cm^2, which are only 0.6 wt% and 1.9 wt% of $ZnO@TiN_xO_y$ nanorod anode, respectively (for 3 mg/cm^2 ZnO nanorods). The nanorod morphology does not change after TiN_xO_y coating (Figure 2.15d). High-resolution transmission electron microscopy (HRTEM) images show uniform TiN_xO_y coating with a thickness of 6.1 nm for $ZnO@TiN_xO_y$ nanorod with 100 cycles ALD (Figure 2.15e, f). ZnO nanorod is hexagonal and TiN_xO_y coating is amorphous, which are evident from TEM (Figure 2.15g, h) and X-ray diffraction (XRD) results (Figure 2.15f). In addition to TEM, X-ray photoelectron spectroscopy (XPS) results also indicate complete coverage of TiN_xO_y on ZnO (Figure 2.15i, j), which is crucial for encapsulating zincate during cycling. Besides, nitrogen peak in the XPS survey spectra (Figure 2.15i) and three Ti 2p peaks in the high-

resolution XPS spectra (Figure 2.15k), which belong to TiO_2,[117] indicate that ALD TiN is partially oxidized to TiN_xO_y.
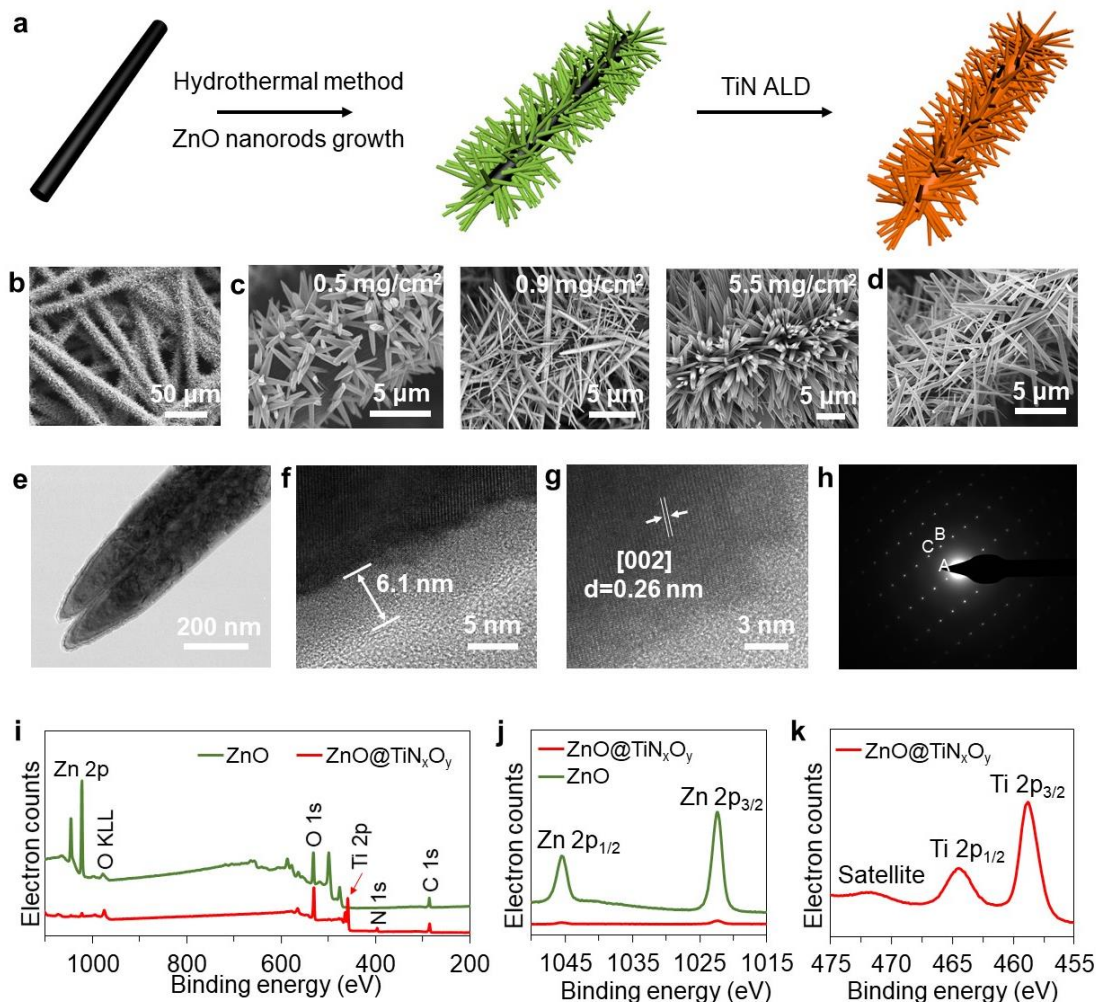
Figure 2.15 - Fabrication and characterization of anodes. a, Schematic of the fabrication process for $ZnO@TiN_xO_y$ core/shell nanorod anode. b, Low magnification SEM image of ZnO nanorod anode. c, High magnification SEM images of three ZnO nanorod anodes with different mass loadings. d, SEM image of $ZnO@TiN_xO_y$ nanorod anode. e, TEM image of a $ZnO@TiN_xO_y$ nanorod. f, HRTEM image of $ZnO@100TiN_xO_y$ nanorod, showing thickness (6.1 nm) of TiN_xO_y coating. g, HRTEM image of $ZnO@TiN_xO_y$ nanorod, showing lattice of ZnO, [002], d= 0.26 nm. h, Electron diffraction pattern of $ZnO@TiN_xO_y$ nanorod, showing diffraction pattern of ZnO. A [002]; B [200]; C [202]. i, XPS survey of ZnO nanorod and $ZnO@TiN_xO_y$ nanorod anodes. j, High-resolution XPS spectra of Zn 2p peaks. k, High-resolution XPS spectra of Ti 2p peaks. The samples shown in Fig. d-k are all deposited by ALD for 100 cycles.

The TiN_xO_y coating, although only a few nanometers thick, firmly supports the ZnO nanorod, blocks zincates, and enables OH^-/H_2O to pass through. As shown in Figure 2.16a, a $ZnO@TiN_xO_y$ anode and an uncoated ZnO anode (1 cm diameter disk) were soaked into two tubes with 2 mL 4M KOH solution, respectively. Then the dissolved Zn concentration in both solutions was measured using inductively coupled plasma atomic emission spectroscopy (ICP-AES). The dissolved Zn of the $ZnO@TiN_xO_y$ anode is much lower than that of the uncoated ZnO anode, which means that TiN_xO_y coating effectively blocks zincates. Furthermore, coin cells with these two anodes and $Ni(OH)_2$ cathodes were assembled to investigate the influence of the TiN_xO_y coating during electrochemical cycling. After 2h charge (1h constant current at 1C rate and 1h constant voltage at 1.93 V), uncoated ZnO nanorod anode shows severely morphological degradation, almost all ZnO nanorods detach from carbon paper because of dissolution (Figure 2.16b). On the other hand, there is no obvious shape change for $ZnO@TiN_xO_y$ nanorod anode with 100 cycles ALD (Figure 2.16c). $ZnO@TiN_xO_y$ nanorod anode with 200 cycles ALD maintained its morphology after charging as well (Figure 2.17). Additional SEM image, elemental mapping (Figure 2.16d), TEM image (Figure 2.16e), and Zn peaks in XRD results (Figure 2.16f) all support that TiN_xO_y coating confined zinc active material inside, while still allowing it to participate in electrochemical reaction. The mass loading of ZnO nanorods shown in Figure 2.16b-e is 0.5 mg/cm^2. For longer nanorods with higher mass loading (~1.7 mg/cm^2), there is also no apparent shape change of $ZnO@TiN_xO_y$ nanorod anode after the first charge and discharge (Figure 2.18), while ZnO nanorod anode shows severe structure degradation after the first charge (Figure 2.19). Electrochemical impedance spectroscopy (EIS) was also employed to investigate the electrochemical influence of

conductive TiN_xO_y coating. As shown in the Nyquist plot (Figure 2.16g) and equivalent circuit (Randles-Ershler impedance)[118], the charge-transfer resistance (R_{ct}) of $ZnO@TiN_xO_y$ nanorod anode (0.8 Ω) is much lower than that of the uncoated ZnO anode (1.8 Ω). This can be attributed to the good conductivity of TiN_xO_y[119] and the high zincate concentration inside the TiN_xO_y coating.
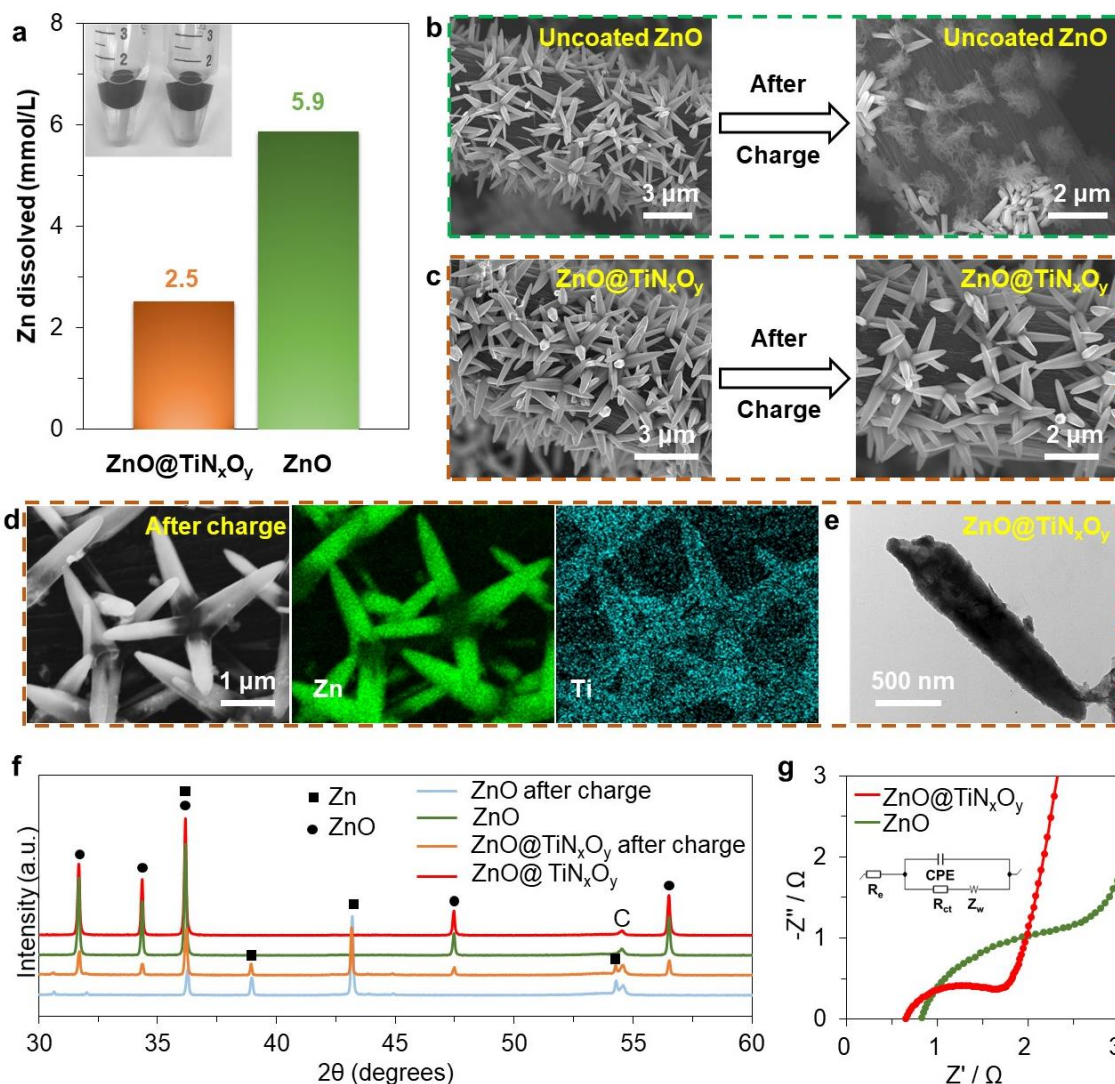
Figure 2.16 - Investigation on the influence of TiN_xO_y coating on the electrochemical performance of zinc anodes. a, ICP results and image (inset) showing dissolved Zn concentration after soaking the $ZnO@TiN_xO_y$ and uncoated ZnO anodes in 4M KOH solution. b,c, SEM images of uncoated ZnO nanorod anode (b) and $ZnO@TiN_xO_y$ nanorod anode (c) before and after 2h charge with 25 µL electrolyte. d, SEM image

44

and elemental mapping of ZnO@TiN$_x$O$_y$ nanorod anode after 2h charge. e, TEM image of ZnO@TiN$_x$O$_y$ nanorod anode after 2h charge. Fig. c-e are from the same anode sample with 100 cycles ALD. f, XRD results of ZnO nanorod and ZnO@TiN$_x$O$_y$ nanorod anode before and after charge. The weak ZnO peaks of ZnO@TiN$_x$O$_y$ nanorod anode with 200 cycles ALD after charge is from residual unreacted ZnO. Tin foils were used as anode current collectors.[120] g, EIS result and equivalent circuit of uncoated ZnO anode and ZnO@TiN$_x$O$_y$ nanorod anode. Z$_w$: Warburg impedance; R$_{ct}$: charge-transfer resistance; CPE: double layer capacity; R$_e$: total ohmic resistance.
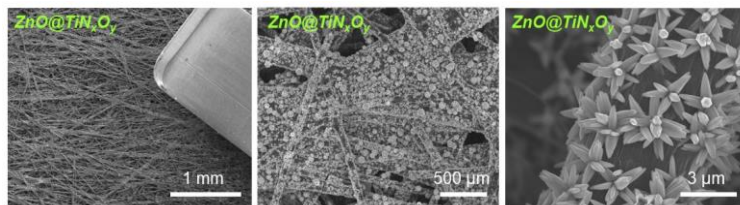
Figure 2.17 - SEM images of 0.5 mg/cm^2 ZnO@TiN$_x$O$_y$ nanorod anode with 200 cycles ALD after 1h constant current charge at 1C rate with 25 µL electrolyte. Tin was used as anode current collector.
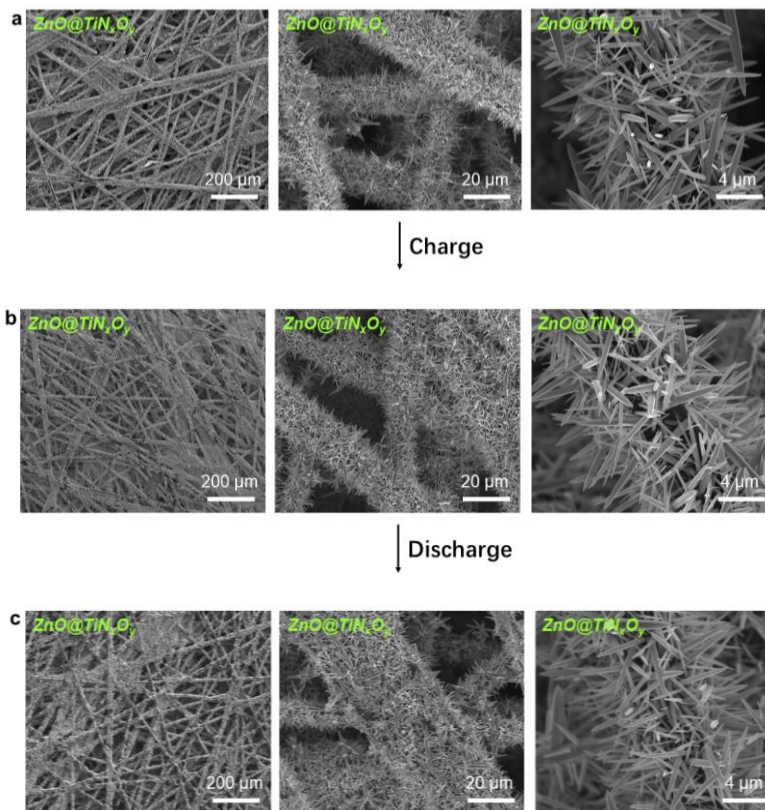
Figure 2.18 - SEM images of pristine ZnO@TiN$_x$O$_y$ nanorod anode with 200 cycles ALD (a), after 3h constant current charge at 0.33C with 25 µL electrolyte (b), and

after further constant current discharge at 0.33C (0.7 h) to 1.5 V with 25 µL electrolyte (c). All SEM images are from same sample with a mass density of 1.7 mg/cm^2. This result indicates that there is almost no shape change during the charge and discharge step.
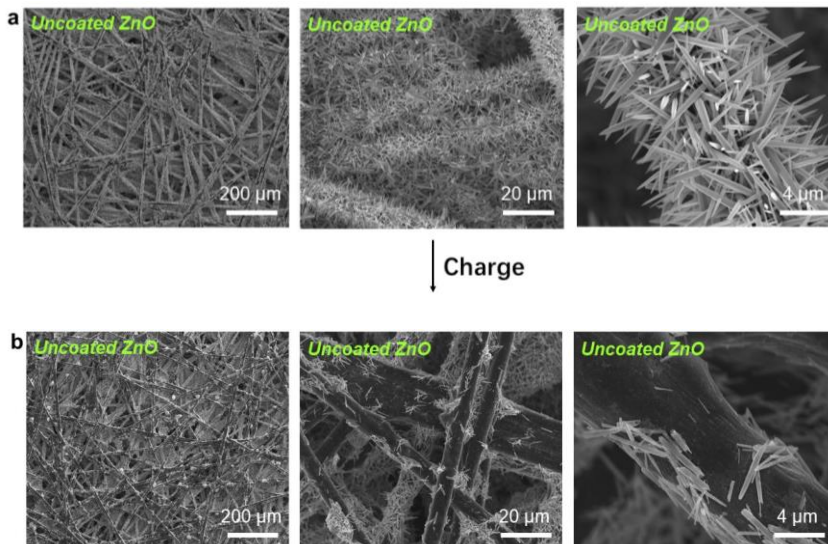
Figure 2.19 - SEM images of pristine uncoated ZnO nanorod anode (a), and after 3h constant current charge at 0.33C with 25 µL electrolyte (b). All SEM images are from same sample with a mass density of 1.7 mg/cm^2. Some nanorods were detached from the beginning as shown in Fig. a, due to external mechanical force during transfer. After charge, most ZnO nanorods grown on the top layer of carbon fibers detached. Because of the small amount of electrolyte, the ZnO nanorods grown on the inner carbon fibers were not in contact with electrolyte in the first charge, and remained.

Zinc anodes were tested in coin-type cells with lean zinc-free electrolyte here to evaluate their real performance, which is different from most of previous investigations[95–97,114,121–126] using beaker cells with a large amount of ZnO saturated electrolyte. When testing the performance of zinc anodes in ZnO saturated electrolyte, all the zincates in the electrolyte could also participate in electrochemical reactions and contribute capacity in addition to the Zn in the anode. However, most previous works reported their specific capacity without counting Zn in the electrolyte, which gives pseudo performance. In an extreme case, even if there is no active material in the anode, only a pure current collector can cycle in ZnO saturated electrolyte. Here two pure carbon fiber paper substrates (1 cm

diameter disk) in a beaker cell with 10 mL ZnO saturated 4M KOH electrolyte and a coin

cell with 100 uL ZnO saturated 4M KOH electrolyte (Figure 2.20a), respectively, were

tested . They were both cycled at 1 mA with a limiting charge capacity of 1 mAh and cut-

off voltage of 1.4/2V. The theoretical specific capacity of ZnO is 658 mAh/g. As shown in

Figure 2.20b, if zinc in the electrolyte is not counted, the pure current collector without any

active material in the beaker cell can show excellent cycling performance with a pseudo

specific discharge capacity of 600 mAh/g (Assume there is 1.5 mg ZnO on the anode,

which has 1 mAh theoretical capacity). However, when zinc in the electrolyte (see Table

2.2 for equivalent ZnO mass) is counted, the real specific discharge capacity in the beaker

cell is only 4 mAh/g, while that in the coin cell is ~150 mAh/g. These results show that

testing zinc anodes in beaker cells with a large amount of ZnO saturated electrolyte will

dramatically decrease the overall specific energy. Moreover, it's hard to evaluate the true

performance of anodes with a lot of capacity contributed from electrolyte. Coin-type cells

use minimum amount of electrolyte and have a higher volumetric capacity compared with

beaker cells, which is closer to practical operating condition. Thus, even though the coin

cell with lean electrolyte is an extreme harsh testing environment (~25 cycles), it was still

chosen to test materials. To evaluate the true performance of anodes, ZnO-free electrolytes

were used because capacity contributed by electrolytes could cause an unrealistically high

capacity of anodes.
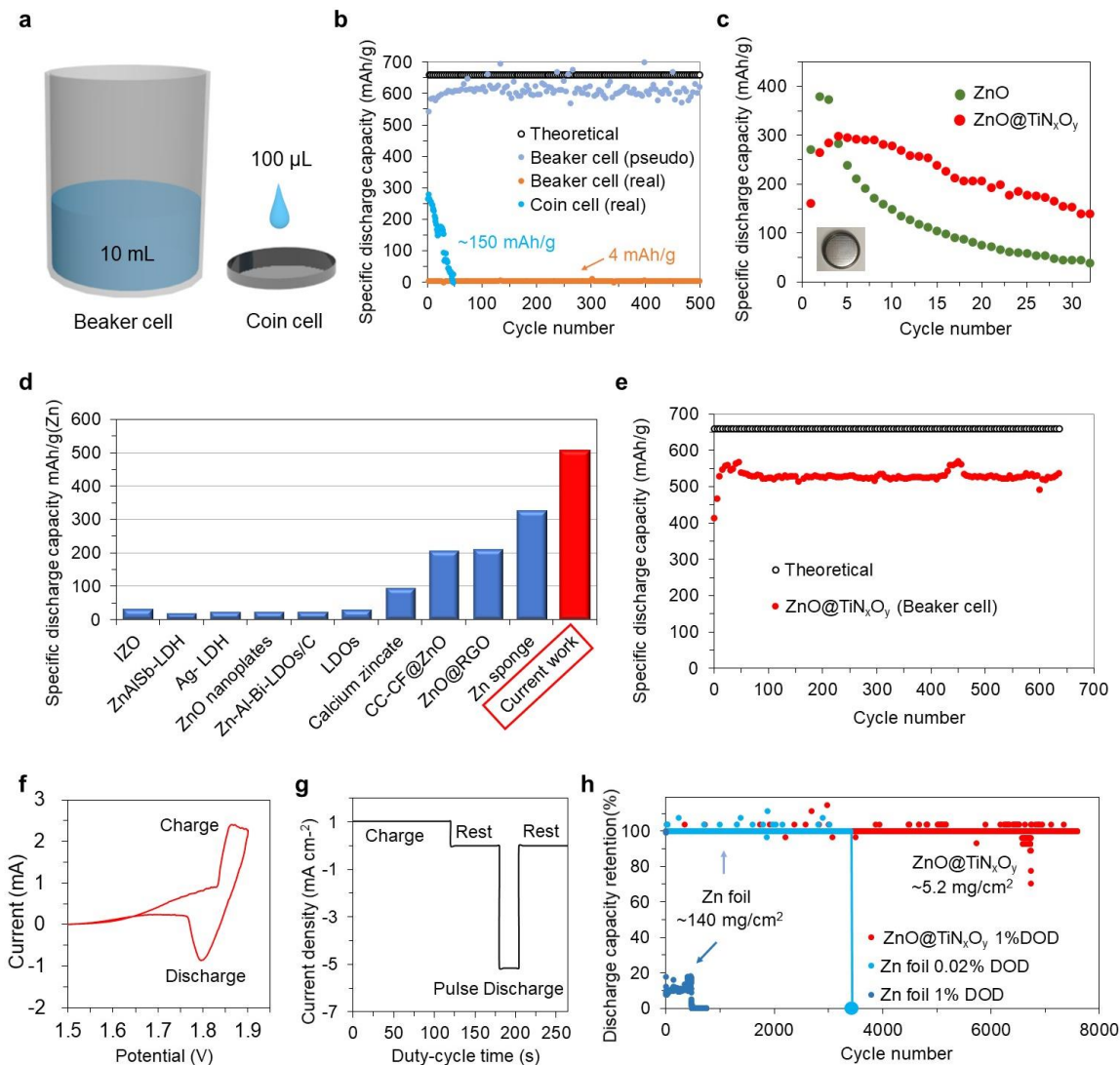
Figure 2.20 - Electrochemical performance of zinc anodes. a, Schematic diagram of beaker cell and coin cell. b, Cycling performance of pure current collector in the beaker cell and coin cell. Real: count all the zinc in the electrolyte. Pseudo: calculation without counting zinc in the electrolyte. One dot every four data points. c, Discharge capacity for the first 32 galvanostatic cycles of uncoated ZnO nanorod and ZnO@TiN$_x$O$_y$ nanorod anodes with ~2.1 mg/cm^2 at 0.5C rate in coin cell with ZnO-free electrolyte. 50 μL electrolyte was dropped onto separator and 10 μL electrolyte was dropped onto cathode. Inset: optical image of a coin cell. d, Comparison of specific discharge capacity between this anode and previously reported anodes. Zinc in the electrode and electrolyte are both counted. e, Cycling performance of the ZnO@TiN$_x$O$_y$ nanorod anode (2 mg/cm^2) with 200 cycles ALD at 0.5C charge and 2C discharge rates in beaker cell with 10 mL ZnO saturated 4M KOH electrolyte. The cut-off voltages are 1.4/2V. One dot every five data points. f, Cyclic voltammogram for ZnO@TiN$_x$O$_y$ anode in coin cell at 0.1 mV s^{-1} scan rate. The CV was done using two electrodes with ZnO@TiN$_x$O$_y$ anode and Ni(OH)$_2$ cathode in ZnO free electrolyte. g, Current density profile as cycled under start-stop conditions in coin

48

cells. h, Long-term discharge capacity retention of Zn foil and ZnO@TiN$_x$O$_y$ nanorod anode as cycled under start-stop conditions with 100 µL electrolyte. Zn foil with 0.02% DOD and ZnO@TiN$_x$O$_y$ nanorod anode with 1% DOD were cycled at the same current density, which is shown in Fig. g. Tin foils were used as anode current collectors. Cells were cycled between 0 and 2 V.

Table 2.2 - Calculation of equivalent ZnO quantity and capacity

System	Large amount of electrolyte	Lean electrolyte
Test equipment	Beaker cell	Coin cell
Volume of electrolyte	10 mL	100 uL
Electrolyte	ZnO saturated 4M KOH	ZnO saturated 4M KOH
Zincate concentration	0.256 mol/L	0.256 mol/L
Amount of zinc	0.00256 mol	0.0000256 mol
Mass of equivalent ZnO	***208 mg***	***2.08 mg***
Capacity contributed by electrolyte	137 mAh	1.37 mAh
Effect of zinc deposition from electrolyte on anode shape change	Big	Small

As shown in Figure 2.20c, the ZnO@TiN$_x$O$_y$ nanorod anode affords remarkable battery performance in lean electrolyte configuration even with a high mass loading of active materials (~2.1 mg/cm^2). The coin cells are galvanostatically deep-cycled to 100% state of charge (SOC) with 1.5 and 1.9 V as cut-off voltages. The charge capacity was limited to the theoretical capacity of ZnO (658 mAh/g). The reversible discharge capacity of ZnO@TiN$_x$O$_y$ nanorod anode at tenth galvanostatic cycle is 279 mAh g^{-1}, which is twice as large as that of uncoated ZnO nanorod anode (148 mAh g^{-1}) at a rate of C/2. The discharge capacity of ZnO@TiN$_x$O$_y$ nanorod anode decays to below 150 mAh g^{-1} after 30 cycles, versus only 9 cycles for uncoated ZnO nanorod anode. For the ZnO@TiN$_x$O$_y$ anode, the TiN$_x$O$_y$ coating did not change the overpotential of ZnO anode with almost the same charge profile as the uncoated ZnO (Figure 2.21). Cycled at a lower rate (C/4) with

50% SOC, the capacity difference between coated and uncoated ZnO nanorod anodes in initial cycles is small, yet ZnO@TiN$_x$O$_y$ nanorod anode shows better capacity retention than uncoated ZnO nanorod anode (Figure 2.22). The discharge capacities of uncoated and sealed ZnO nanorod anodes decay to 50% after 31 and 53 cycles, respectively. To probe the behavior of ZnO over cycling, the electrodes after three galvanostatic cycles at 0.33C were imaged . As can be seen in Figure 2.23, ZnO@TiN$_x$O$_y$ nanorod anode keeps its original morphology after cycling, whereas almost no nanorods can be found on the carbon paper for the uncoated ZnO nanorod anode.
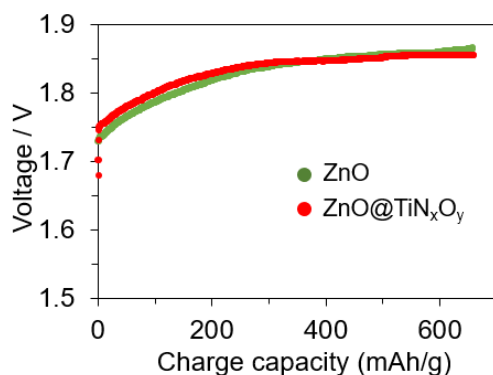
Figure 2.21 - Charge voltage profiles of the ZnO and ZnO@TiN$_x$O$_y$ anodes.
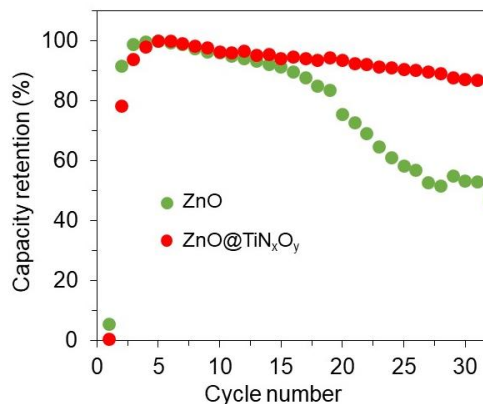
Figure 2.22 - Discharge capacity retention of uncoated ZnO nanorod and ZnO@TiN$_x$O$_y$ nanorod anodes with ~1.5 mg/cm^2 at 0.25C rate in coin cells. 25 µL electrolyte was dropped onto separator. The cut-off voltages are 1.5/1.9V. The

50

maximum discharge capacity (corresponding to 100%) of uncoated ZnO nanorod and ZnO@TiN$_x$O$_y$ nanorod anodes are 235.2 mAh g^{-1} and 153.5 mAh g^{-1}, respectively.
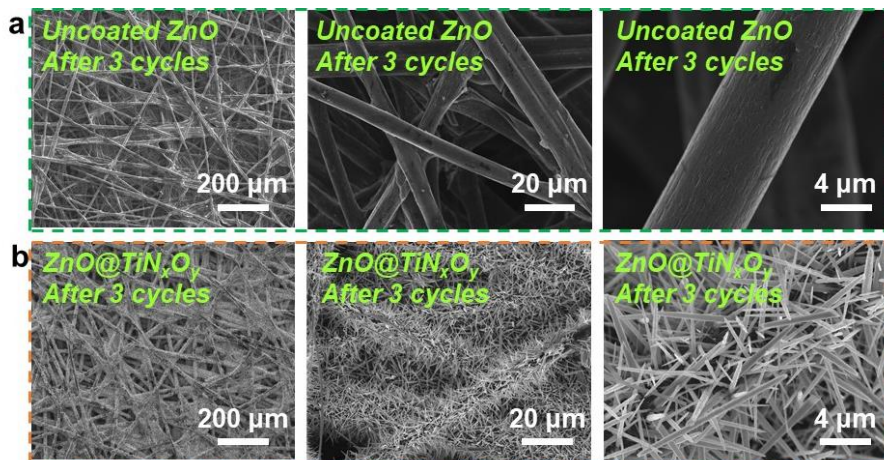
Figure 2.23 - SEM images of 1.8 mg/cm^2 uncoated ZnO nanorod anode (a) and ZnO@TiN$_x$O$_y$ nanorod anode (b) after three galvanostatic cycles at 0.33C rate with 25 µL electrolyte. The cut-off voltages are 1.5/1.9V.

The superior performance of ZnO@TiN$_x$O$_y$ nanorod anode can be attributed to the small feature size of ZnO and conformal TiN$_x$O$_y$ coating. Below the critical passivation thickness, anode passivation problem is eliminated. And the TiN$_x$O$_y$ coating serves as an electrical pathway, confines large zincate molecules yet allows OH$^-$ and water to pass. As a mechanical backbone, TiN$_x$O$_y$ coating protects ZnO nanorods from detaching from carbon paper substrate and thus provides a short zincate mass transfer path for the reaction. Without TiN$_x$O$_y$ coating, ZnO nanorod will detach from substrate upon charging. This on one hand leads to a much slower mass transport for electrically disconnected ZnO to dissolve in electrolyte to form zincate and then diffuse to current collector. On the other hand, detached ZnO or dissolved zincate may migrate far from anode and never participate in further cycling. Both mechanisms will cause capacity decay over cycling. The utilization of Zn could be potentially modeled by quantitative comparison of electroreduction rate and mass transfer rate of Zn(OH)$_4^{2-}$.

The ZnO@TiN$_x$O$_y$ nanorod anode was also tested in pouch cell with ZnO-free electrolyte (Figure 2.24). It achieves a specific discharge capacity of 408 mAh/g (based on ZnO if not otherwise stated), which is 508 mAh/g(Zn). As shown in Figure 2.20d, the ZnO@TiN$_x$O$_y$ nanorod anode demonstrates a much higher specific capacity than that of many previously reported zinc anodes.[74,79,127,95,96,98,114,121–124] The ZnO@TiN$_x$O$_y$ nanorod anodes in beaker cell (Figure 2.20e) and pouch cell with ZnO saturated electrolyte were also tested, which achieves a discharge capacity of ~550 mAh/g for >640 cycles (64 days) and 50 cycles, respectively. Figure 2.20f shows the cyclic voltammogram (CV) of the ZnO@TiN$_x$O$_y$ nanorod anode in coin cell with ZnO free electrolyte. CV of the ZnO@TiN$_x$O$_y$ nanorod anode in pouch and beaker cells is shown in Figure 2.25. In addition, the ZnO@TiN$_x$O$_y$ nanorod anode also has excellent performance under start-stop operations, demonstrating potential to replace lead acid batteries in micro-hybrid vehicles[128]. Engine restart, rest and pulse discharge are involved in the start-stop operation.[79] The procedure of test is showed in Figure 2.20g. The capacity of ZnO@TiN$_x$O$_y$ nanorod anode was kept at 1% depth of discharge (DOD) per duty cycle. The ZnO@TiN$_x$O$_y$ nanorod anode maintained 100% discharge capacity for more than 7,500 cycles (Figure 2.20h) at 1% DOD. Voltage profile of the ZnO@TiN$_x$O$_y$ nanorod anode was shown in Figure 2.26. Under the same current density (Figure 2.20g), Zn foil died after 3,400 cycles, which is less than half of cycle number of ZnO@TiN$_x$O$_y$ nanorod anode, even though the DOD of Zn foil is only 0.02% (1/50 of that of ZnO@TiN$_x$O$_y$ nanorod anode). This Zn foil cell died with a sudden voltage drop to <0 V because Zn is completely passivated by ZnO. And the cell was severely swelled, possibly due to accumulation of hydrogen evolved on the anode (Figure 2.26). Severe hydrogen evolution occurs after the

passivation of Zn anode. The cell with $ZnO@TiN_xO_y$ nanorod anode only slightly swelled, which indicated less side reaction and higher utilization of zinc. Less swelling further indicates the $ZnO@TiN_xO_y$ nanorod anode does not passivate and retains its activity over thousands of cycles. Besides, Zn foil start stop performance with 1% DOD at the same time interval was also tested as shown in Figure 2.20g, which showed dramatically discharge capacity decay (Figure 2.20h). This result indicates the high stability of $ZnO@TiN_xO_y$ nanorod anode.
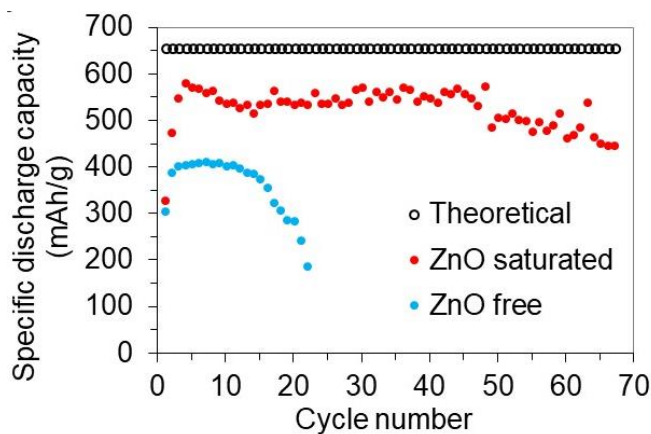
Figure 2.24 - Cycling performance of ~1.1 mg/cm² $ZnO@TiN_xO_y$ nanorod anodes in pouch cells with ZnO saturated and ZnO-free electrolytes, respectively. They were cycled at 1C for charge and 5C for discharge with 1.4/2V cut-off voltages.
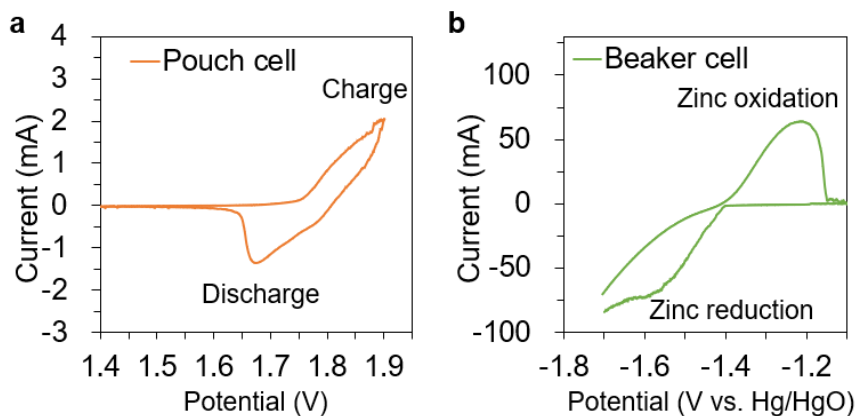
Figure 2.25 - Cyclic voltammogram for $ZnO@TiN_xO_y$ anodes in pouch cell (a) and beaker cell (b) at 0.1 mV s⁻¹ scan rate. The CV for the anode in pouch cell was done using two electrodes with $ZnO@TiN_xO_y$ anode and $Ni(OH)_2$ cathode in ZnO

53

saturated electrolyte. The CV for the anode in beaker cell was done using three electrodes with ZnO@TiN$_x$O$_y$ anode, Hg/HgO reference electrode and graphite counter electrode in ZnO saturated 4M KOH electrolyte.
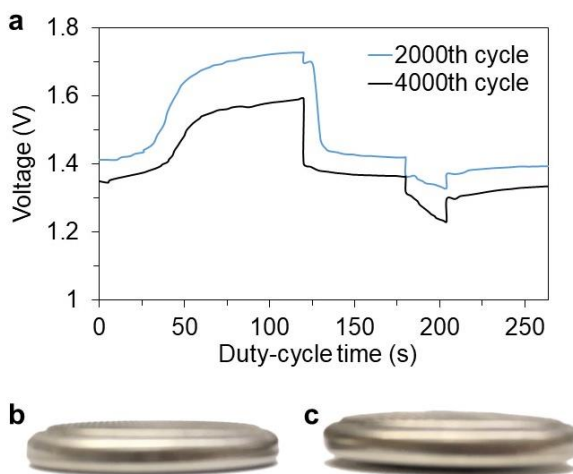
Figure 2.26 - Start-stop operations. a, Voltage profiles of ZnO@TiN$_x$O$_y$ nanorod anode of the 2000th and 4000th cycles under start-stop conditions. b,c, Photo of cells, with ZnO@TiN$_x$O$_y$ nanorod anode (b) and Zn foil (c) as anode respectively, after long-term start-stop conditions at the same current density.

2.3.4   Conclusion

In summary, the ZnO@TiN$_x$O$_y$ nanorod anode achieves very high specific discharge capacity and superior reversibility when testing in a coin cell with lean ZnO-free electrolyte. In commercial PowerGenix AA batteries, which consists Zn metal anode and NiOOH cathode, the discharge capacity decayed to 50% of its initial capacity after only 9 cycles (0.5C, 20 °C, charged to 105% theoretical capacity).[120] NiOOH cathodes are very reversible[129], and the Zn anode is the main cause of the poor reversibility. The ZnO@TiN$_x$O$_y$ core/shell nanorod anode structure reported here successfully solves the problems of ZnO passivation and zincate dissolution simultaneously, and significantly improved the cycle life of Zn anode. Because of electrolyte consumption and bubble accumulation resulted from hydrogen evolution side reaction, anodes degraded ultimately

when cycled in coin cells with lean electrolyte. It is believed this work can be further improved by coating hydrogen evolution suppressive materials. In addition, the mechanistic understanding and design principles could provide guidance to future design of zinc and other metal anodes (e.g. Li, Na, Mg, Ca). This work prepares the path towards rechargeable Zn-air aqueous batteries, and other rechargeable, high-energy and safe batteries.

2.4 Hydrogen-Evolution-Suppressing Zn Anode

2.4.1 Introduction

A battery-gas chromatography (GC) quantitative analysis method (Figure 2.27) has been created to identify the influence of HER on the capacity loss of zinc anodes. This is achieved by measuring the evolved H_2 using GC after charging/discharging the zinc anode in alkaline electrolyte (ZnO-saturated 4M KOH) for one cycle (Figure 2.28). It is worth noting that the amount of NiOOH was in excess, which could guarantee the full depletion of Zn in the discharge step. In other words, the capacity loss (charge capacity-discharge capacity) on Zn anodes is attributed to side reactions on Zn anodes. As shown in Figure 2.29, the capacity loss on the Zn anode is almost fully caused by HER (99.47% = 87.34%/87.81%). The other 0.46% of capacity loss might be caused by the oxidation of Zn^{120} through reacting with O_2. In consideration of Zn anodes, HER suppressing Zn anodes should possess high Coulombic efficiency (discharge capacity/charge capacity).
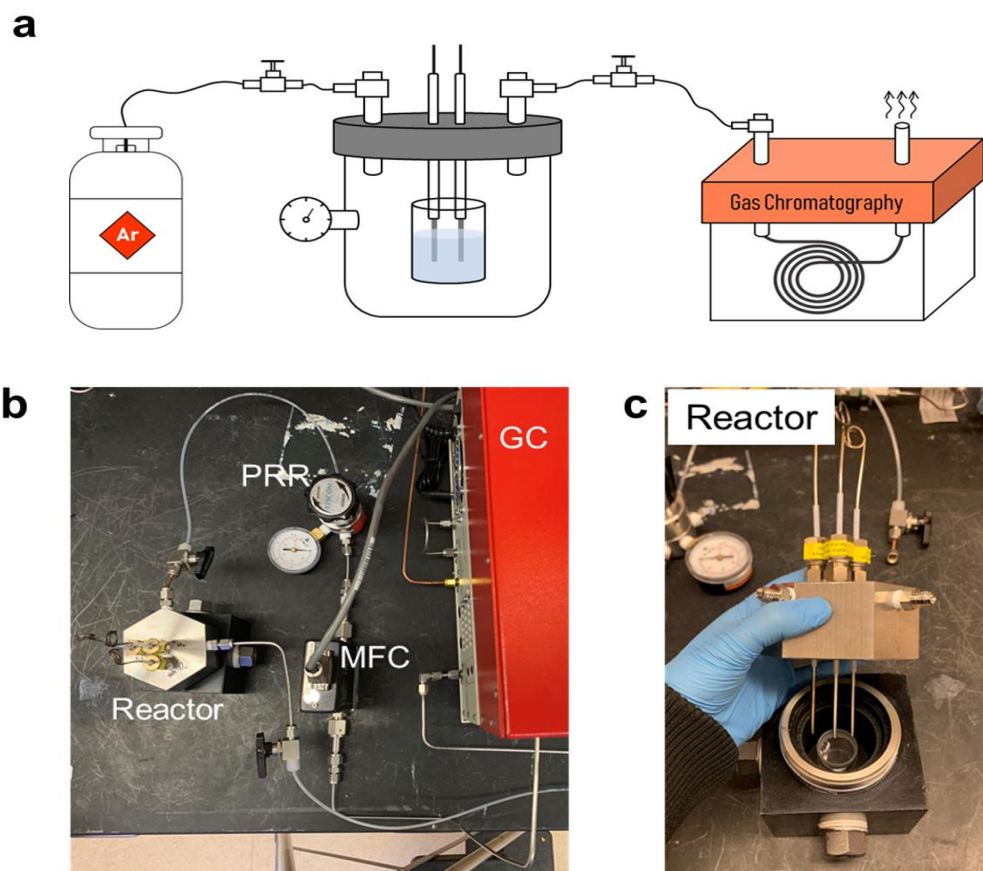
Figure 2.27 - Battery-GC quantitative analysis method. (a-c) Schematic diagram (a), experiment setup (b), and reactor design (c) of the battery-GC quantitative analysis method to quantitatively identify the influence of HER on Coulombic efficiency of zinc anodes. PRR: pressure reducing regulator; MFC: mass flow controller; GC: gas chromatography.
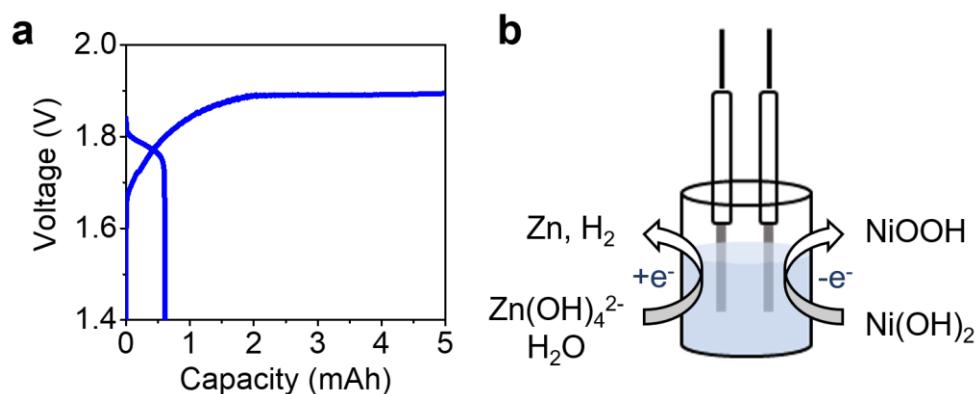
Figure 2.28 - Electrode reactions happened during charging for Zn-Ni battery system.
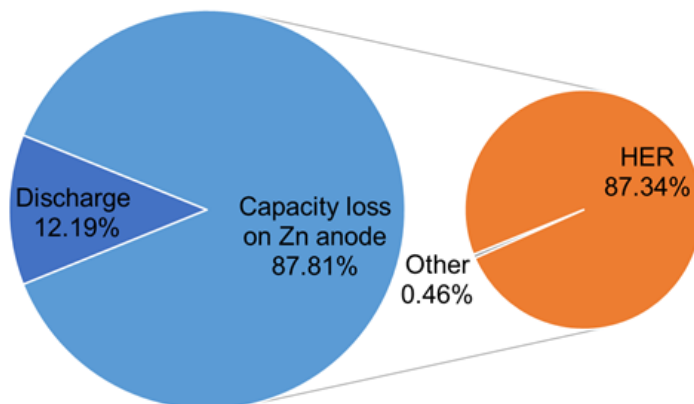
Figure 2.29 - Distribution of the charged capacity on the zinc anode in a Zn-Ni battery. The capacity loss on the Zn anode is almost fully caused by HER. Thus, HER suppressing zinc anodes should possess high Coulombic efficiency.

Attempts have been made in the past to overcome one or two of passivation, dissolution, and HER issues. For example, sub-micron-sized structures[74,75], composites with highly conductive materials[76–78], and 3D high surface area electrodes[79,80] have been shown to be effective in addressing the ZnO passivation issue. Surface protective coatings[9,81,82] have been demonstrated to slow down the loss of zinc active material. Surface treatments[84,85] and additives[86] have been used to suppress the HER. However, there are very few successful examples that address these issues simultaneously.

In this work, sub-micron-sized anodes were sealed by coating them with a HER suppressing ion-sieving layer to tackle simultaneously passivation, dissolution, and HER issues (Figure 2.30). This design features the following advantages: (i) sub-micron-sized ZnO avoids passivation and allows complete utilization of the active materials; (ii) ion-sieving coating layer confines zincate inside and mitigates shape changes of the electrode; and (iii) the coating layer is made of HER suppressing material, which represses side reactions. The results demonstrate that HER suppressing sealed nanorod (HSSN) zinc

57

anodes exhibit long cycle life, high Coulombic efficiency, and high specific discharge capacity.

HSSN anode
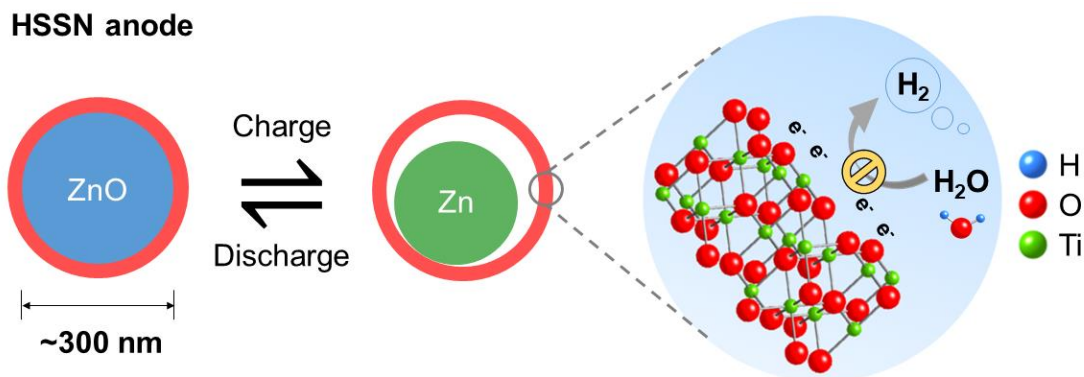
Figure 2.30 - Schematic illustration of zinc anode design principle: sealed sub-micron-sized anodes with a HER suppressing ion-sieving coating to overcome passivation, dissolution, and hydrogen evolution issues simultaneously in alkaline electrolytes.

2.4.2 *Experimental Section*

Synthesis of the uncoated ZnO nanorod anode. ZnO nanorods were grown on carbon papers (8.4 mg/cm^2) by a hydrothermal method. Carbon paper (Fuel Cell Store) was first heated in air at 500 °C for 1 h to increase its wettability. Then, the carbon paper was soaked in 0.1 M KMnO$_4$ (Sigma Aldrich) aqueous solution for 1 h to form a seed layer. The ZnO precursor solution is prepared by mixing 50 mL zinc nitrate hexahydrate (30 mM, Alfa Aesar), 50 mL hexamethylenetetramine (30 mM, Sigma Aldrich), and ammonia (28.0-30.0% NH$_3$ basis, Sigma Aldrich). The seeded carbon paper was placed in the above solution[115], followed by heating in an oven at 90 °C for a certain time. After DI-H$_2$O washing and drying at 80 °C for 3 h, the white-colored product on carbon paper was obtained.

Synthesis of the HER suppressing sealed nanosized (HSSN) zinc anode. The HSSN zinc anode with the ZnO core/TiO$_2$ shell structure was synthesized using a solution method. The carbon paper with grown ZnO nanorods was immersed into a solution of 0.075 M (NH$_4$)$_2$TiF$_6$ and 0.2 M H$_3$BO$_3$ for 10 min at room temperature[130]. A layer of ~30 nm thick TiO$_2$ was deposited.

Synthesis of the ZnO@TiN$_x$O$_y$ anode. To get the ZnO@TiN$_x$O$_y$ anode, TiN was deposited onto the uncoated ZnO nanorod anode through atomic layer deposition (ALD). ALD was conducted in Cambridge FIJI Plasma ALD system. The precursors of TiN were TDMAT and N$_2$. During TiN ALD process, the recipe was run 200 cycles (1 Å per cycle) at 250 °C. Then, when ZnO@TiN nanorods were exposed to air, the TiN was partially oxidized to TiN$_x$O$_y$.

Sheet resistance measurement of TiN$_x$O$_y$ and TiO$_2$ coatings using a four-point probe system. To measure the sheet resistance of TiN$_x$O$_y$ and TiO$_2$ coatings, TiN$_x$O$_y$ and TiO$_2$ are deposited onto glass slides, respectively. The glass slides were cleaned by sonication in acetone/ethanol, followed by ultraviolet-ozone (UVO) treatment. TiN$_x$O$_y$ was obtained through an ALD of TiN on the glass slides followed by an oxidation step in air. The precursors of TiN were TDMAT and N$_2$. During ALD process, the recipe was run 400 cycles (1 Å per cycle) at 250 °C. A layer of ~1 μm thick TiO2 was deposited on the glass slides by immersing the glass slides in a solution of 0.1 M (NH4)2TiF6 +0.2 M H3BO3 for 11h at 25 °C.[130] The sheet resistance was measured using a four-point probe measurement system (2000 multimeter, Keithley).

Material Characterization and Measurements. The morphological and compositional analyses were carried out using scanning electron microscopy (SEM, Hitachi SU 8230), transmission electron microscopy (TEM, Hitachi HT7700, FEI Tecnai F30, and JEOL 100 CX-II), and scanning transmission electron microscopy (STEM, Hitachi HD-2700). The X-ray diffraction patterns (XRD, Panalytical XPert PRO Alpha-1) were carried out with Cu K-Alpha radiation. The X-ray photoelectron spectroscopy (XPS) was measured with Thermo Scientific K-Alpha system. The specific Brunauer–Emmett–Teller surface areas and pore size distribution were determined by physisorption (BELSORP-max, MicrotracBEL Corp.). The dissolved Zn concentration of samples in 4M KOH electrolyte was measured with an inductively coupled plasma (ICP) measurement. Cyclic voltammetry, linear sweep voltammetry, and electrochemical impedance spectroscopy were conducted using a VSP system (BioLogic). Battery cycling tests were carried out using LANHE operating in galvanostatic mode.

In the battery-gas chromatography quantitative analysis measurement, the airtight battery system was connected to a gas chromatography (MG#5, SRI Instruments). The system was purged with Ar before the measurement. The stainless-steel rod was used as the anode. ZnO-saturated 4M KOH (Sigma Aldrich) was used as the electrolyte. A 4 cm^2 cathode from a commercial Ni-Zn AA battery (PowerGenix), which is a mixture of NiOOH (~8 mAh/cm^2)/Ni(OH)$_2$ (~32 mAh/cm^2), was harvested to pair with the anode. The battery was charged at 20 mA for 15 min and then fully discharged (20 mA) to 0.8 V for 1 cycle. Then H$_2$ measurements were conducted using the thermal conductivity detector. Ar was the carrier gas for gas chromatography. The capacity loss (= Charge capacity - Discharge

capacity = Capacity (HER) + Capacity (Other)) on the Zn anode is almost fully caused by HER (99.47%).

Electrochemistry. The zinc anodes were cut to round disks with diameter of 1 cm. Cathodes from commercial Ni-Zn AA batteries (PowerGenix), which is a mixture of NiOOH ($\sim$8 mAh/cm^2)/Ni(OH)$_2$ ($\sim$32 mAh/cm^2), were harvested to pair with the anodes.

Coin cell: CR2032 cases (MTI Corporation) were used to make coin cells. The aqueous electrolyte consists of 4 M KOH (Sigma Aldrich, 99.99%), 2 M KF (Alfa Aesar, 99.99%) and 2 M K$_2$CO$_3$ (Alfa Aesar, 99.997%)[116]. 25 μL electrolyte was used. Glass fiber (GE Healthcare, Whatman^{TM} 10370003) was used as the separator.

Pouch cell: Pouch-type batteries were assembled using Ampac's SealPAK. The mass loading of active material (ZnO) on the anode is 1.5 mg/cm^2. The aqueous electrolyte consists of 4 M KOH (Sigma Aldrich, 99.99%), 2 M KF (Alfa Aesar, 99.99%) and 2 M K$_2$CO$_3$ (Alfa Aesar, 99.997%) with saturated ZnO. 100 μL electrolyte was used. Glass fiber (GE Healthcare, Whatman^{TM} 10370003) was used as the separator. Ti wires were used as electrode terminals. Cells are galvanostatically cycled at a charge rate of 1C and a discharge rate of 5C between 1.4 and 1.9 V. For anodes cycled at 100% DOD, the anodes were activated by being pre-cycled in pouch cells for 6 cycles. The charge capacity limit cut-off is 658 mAh/g (theoretical specific capacity of ZnO). For anodes cycled at 40% DOD, the anodes were activated by being pre-cycled with 100% active material utilization for 1 cycle and then being fully charged.

Beaker cell: In beaker-type batteries, the mass loading of active material (ZnO) on the anode is 1.6 mg/cm^2. 10 mL ZnO-saturated 4M KOH (Sigma Aldrich) was used as the

electrolyte. Cells are galvanostatically cycled at 100% DOD at a charge rate of 1C and a discharge rate of 5C between 1.4 and 1.9 V. The anodes were activated by being pre-cycled in beaker cells for 50 cycles. The charge capacity limit cut-off is 658 mAh/g. Ag wire was used as anode terminal. Stainless steel wire was used as cathode terminal.

Electrolyte-to-discharge-capacity (E/DC) ratio (Equation 3):

$$E/DC\ ratio = Volume\ of\ electrolyte/measured\ discharge\ capacity \qquad (3)$$

The theoretical gravimetric capacity of Zn metal (Equation 4):

$$C_g(mAh\ g^{-1}) = \frac{1}{MW_{Zn}} * \frac{nF}{3.6} = \frac{1}{65.38} * \frac{2*96485}{3.6} = 820 \qquad (4)$$

The theoretical volumetric capacity of Zn metal (Equation 5):

$$C_v(mAh\ cm^{-3}) = C_g * \rho_{Zn} = 5854 \qquad (5)$$

where ρ_{Zn} is the density of Zn metal. $\rho_{Zn} = 7.14\ g\ cm^{-3}$.

The theoretical gravimetric energy density of Zn-air batteries (calculated based on the discharged state, ZnO) (Equation 6):

$$E_g(Wh\ kg^{-1}) = \frac{1}{MW_{ZnO}} * \frac{nF}{3.6} * V = \frac{1}{81.38} * \frac{2*96485}{3.6} * 1.66 = 1093 \qquad (6)$$

where V is the battery volatge. $V = 1.66\ V$.

The theoretical volumetric energy density of Zn-air batteries (Equation 7):

$$E_v (Wh\ L^{-1}) = E_g * \rho_{ZnO} = 6134 \qquad (7)$$

where ρ_{ZnO} is the density of ZnO. $\rho_{ZnO} = 5.61\ g\ cm^{-3}$.

Simulation of hydrogen suppressing property. Simulation based on force field model was conducted to investigate the hydrogen suppressing property of TiO_2 and TiN_xO_y. The Monte Carlo and Least Squares techniques are used to minimize the energy. Ti_5O_{10} cluster was used to represent amorphous TiO_2. For TiN_xO_y, the overall atomic ratio of O to N (O/N) was experimentally determined to be 6.66 as evidenced by XPS. From many possible structures of amorphous TiN_xO_y, four representative models (denoted as TiN_xO_y-n, n=1, 2, 3, 4) with O/N atomic ratios of 9 and 4 were chosen and built to simulate the actual shell material. Ti_5O_9N cluster (O/N=9) for TiN_xO_y-1 and TiN_xO_y-2, and $Ti_5O_8N_2$ cluster (O/N=4) for TiN_xO_y-3 and TiN_xO_y-4 are built. ΔG_H^* represents the free energy for H adsorption. In a three-state diagram, consisting of an initial H^+ state, an intermediate H^* state, and $1/2 H_2$ as the final product, the material with higher $|\Delta G_H^*|$ value possesses lower catalytic activity[131,132] and thus better hydrogen suppressing capability. ΔG_H^* was obtained by $\Delta G_{H^*} = \Delta E_H + \Delta E_{ZPE} - T\Delta S_H$, where ΔE_H is the binding energy of H species, ΔE_{ZPE} and ΔS_H are the zero point energy change and entropy change of adsorption H, respectively. The contribution of entropies and ZPE for ΔG_{H^*} were obtained according to literatures[131,132], where finally $\Delta G_{H^*} = \Delta E_H + 0.24\ eV$. ΔE_H was obtained by $\Delta E_H = E_{M-H} - E_M - 1/2 \times E_{H_2}$. E_{H_2} was calculated to be -3.040 eV.

2.4.3 Results and Discussion

The critical thickness of ZnO passivation layer has previously been quantified to be ~ 2 μm when a zinc metal anode is completely passivated[81]. Thus, sub-micron-sized zinc anodes are believed to be able to overcome the passivation problem. However, decreasing the feature size to be nanoscale will intensify the dissolution and HER problems, due to increased electrode-electrolyte contact area[94]. Therefore, it was proposed to seal sub-micron-sized anodes by uniformly coating a HER suppressing ion-sieving layer, which can suppress HER and selectively block larger zincate ions inside the coating while enabling OH^-/H_2O transport. Some Zn anodes have been reported to have the above-proposed structure, such as Al_2O_3 coated Zn powders[84], Li_2O–$2B_2O_3$ coated Zn powders[85] and TiO_2-Coated ZnO[113]. However, there is lack of evidence showing that the coating is uniform, with either no or unclear TEM images. As a result, these structures may still suffer dissolution and HER issues, which might be the reason for their short cycle life (<20 cycles)[84,85] and low specific discharge capacity[113]. I have also reported a $ZnO@TiN_xO_y$ anode[9], which could address the dissolution issue while the HER issue still exists. In this study, TiO_2 was chosen as the coating material here to demonstrate the concept, as it is stable with alkaline electrolytes and has been reported to have low HER activity[133]. A binder-free self-supporting ZnO nanorod anode was chosen as the model system for this study because its structure and morphology can be easily studied. This design principle is applicable to Zn anodes with other structures and coating materials.

The HSSN anode was successfully fabricated as shown in Figure 2.31. ZnO nanorods were first grown on the carbon paper hydrothermally[115]. The TiO_2 layer was coated on the ZnO nanorods via a mild solution method at room temperature[130]. The ZnO nanorods were immersed in an aqueous solution consisting of 0.075 M $(NH_4)_2TiF_6$ and 0.2

M H_3BO_3. After the TiO_2 coating, the ZnO nanorod structure was well maintained (Figure 2.32). Scanning transmission electron microscopy (STEM) image and elemental mappings (Figure 2.33a) of the HSSN anode confirms that the TiO_2 coating is uniform. Spatial distributions of Zn and Ti were also obtained by taking energy-dispersive X-ray (EDX) spectroscopies in the core and shell regions (Figure 2.33b). The core region shows a much higher Zn intensity than that of the shell region, which further affirms the ZnO core/TiO_2 shell structure. During synthesis, $(NH_4)_2TiF_6$ hydrolyzed to TiO_2 on the surface of ZnO while surface ZnO slightly dissolved in the solution with acids produced by $(NH_4)_2TiF_6$ hydrolysis[130]. Thus, it is believed some Zn species went into the TiO_2 coating during the synthesis, which may explain for the Zn signal on the TiO_2 shell. As evidenced by Figure 2.33c, the ZnO in the core has a hexagonal close packed crystal structure and the TiO_2 coating is amorphous. The TiO_2 layer has a thickness of ~31.7 nm (Figure 2.33d). The mass loading of TiO_2 is ~0.35 mg/cm^2, which is only ~10.4 wt% of the HSSN anode (with 3 mg/cm^2 ZnO nanorods). After etching the ZnO away, the hollow nanoarrays stayed in place (Figure 2.34), displaying that the TiO_2 coating, although only 30 nm thick, is mechanically strong and firmly supports the ZnO nanorods.
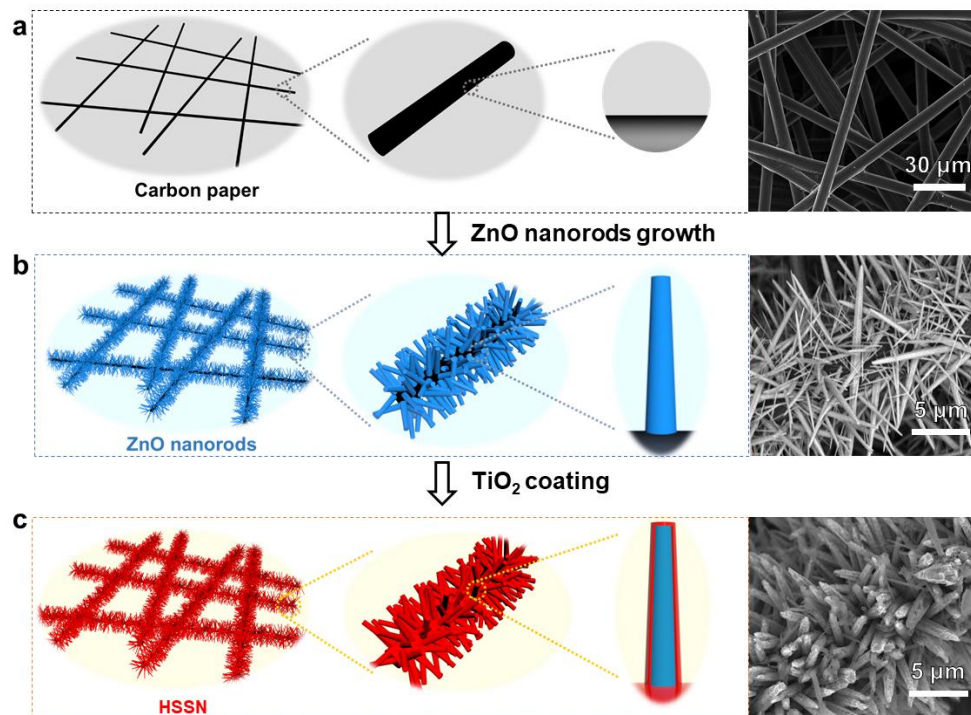
Figure 2.31 - Fabrication of the HSSN anode. a,b,c, Schematic diagrams and SEM images of carbon paper (a), ZnO nanorod anode (b), and HSSN anode (c).
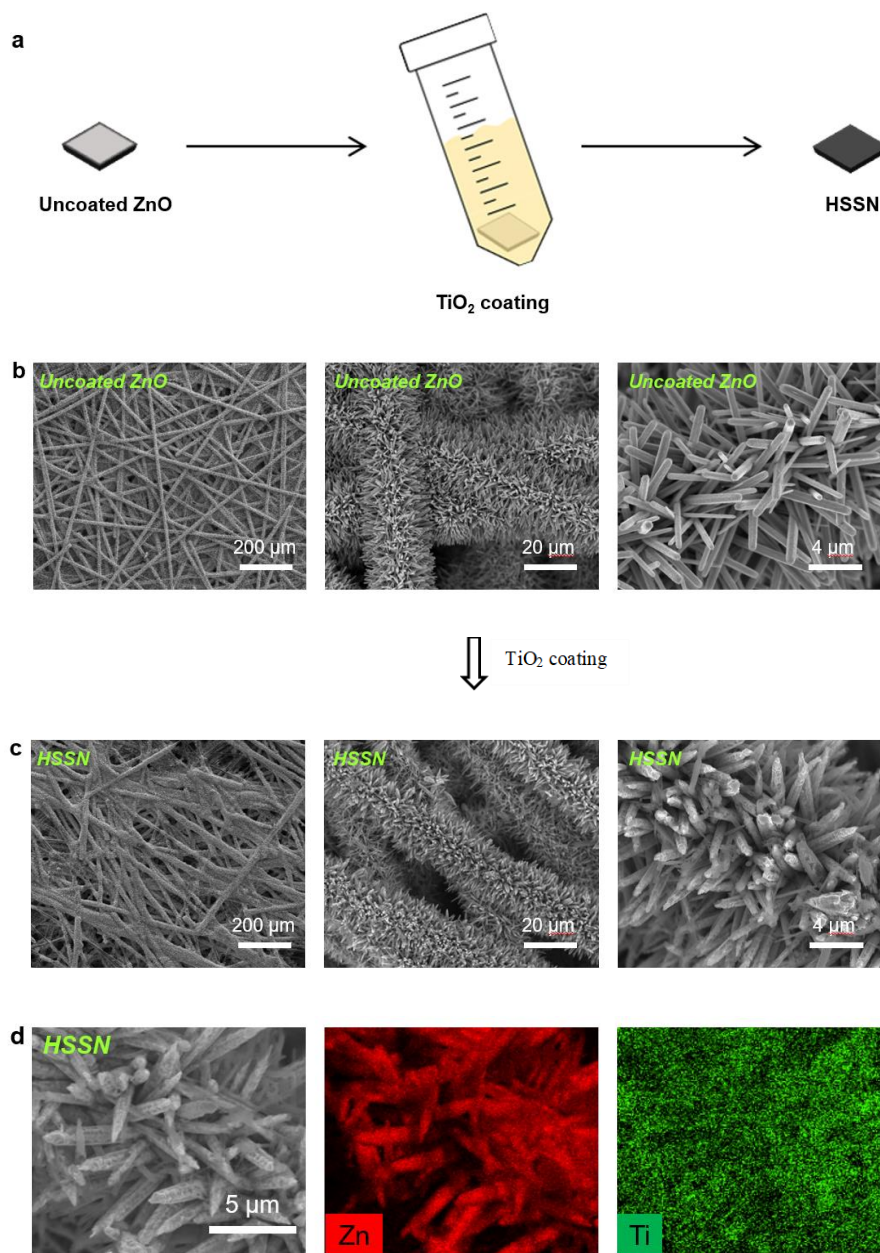
Figure 2.32 - TiO₂ coating process. (a) Schematic diagram of TiO₂ coating process. (b)(c) SEM images of ZnO nanorods before (b) and after TiO₂ coating (c). (d) SEM image and elemental mappings of the HSSN anode.
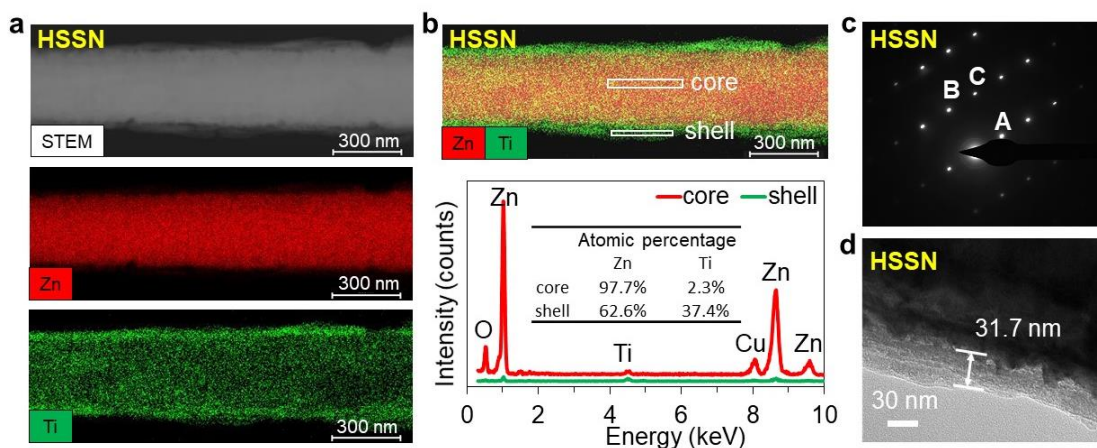
Figure 2.33 - Characterization of a single ZnO@TiO₂ nanorod collected from the HSSN anode. a, STEM image and elemental mappings of a ZnO@TiO₂ nanorod. **b,** Spatial distributions of Zn and Ti elements and EDX spectroscopies in the core and shell regions. **c,** Transmission electron microscopy (TEM) diffraction image of a ZnO@TiO₂ nanorod, showing diffraction pattern of hexagonal ZnO. A [002]; B [110]; C [112]. **d,** TEM image of a ZnO@TiO₂ nanorod, showing the thickness (~30 nm) of TiO₂ coating.
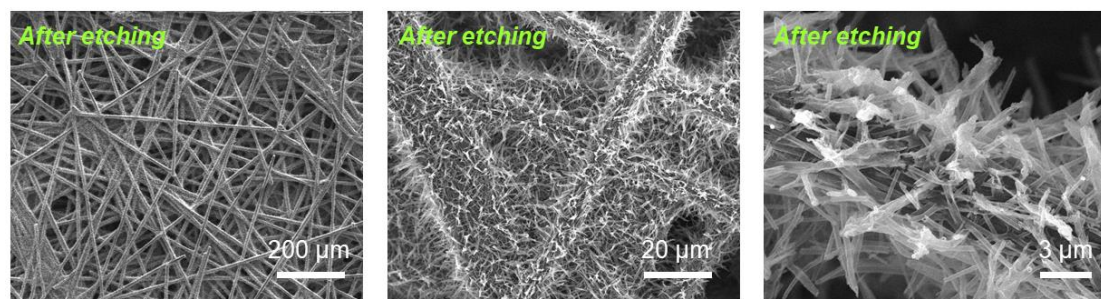
Figure 2.34 - SEM images of HSSN anode after etching ZnO away.

To evaluate the capability of the TiO₂ shell to suppress zincate dissolution, both the HSSN and the uncoated ZnO anodes were soaked in ZnO-free 4M KOH solution for 15 minutes. The ratio of ZnO active material mass and solution volume was 0.02 mg/μL. The dissolved Zn concentration was then measured in both solutions using inductively coupled plasma atomic emission spectroscopy (ICP-AES). As shown in Figure 2.35a, the dissolved Zn of the HSSN anode (1.9%) is much lower than that of the uncoated ZnO anode (16.9%). 90% ZnO dissolution is suppressed in the HSSN anode, which displays that the TiO₂ shell

effectively blocks zincate ions. Both anodes were imaged after soaking in 4M KOH solution (Figure 2.36), which also supports that TiO$_2$ coating can effectively confine zincates inside the shell.
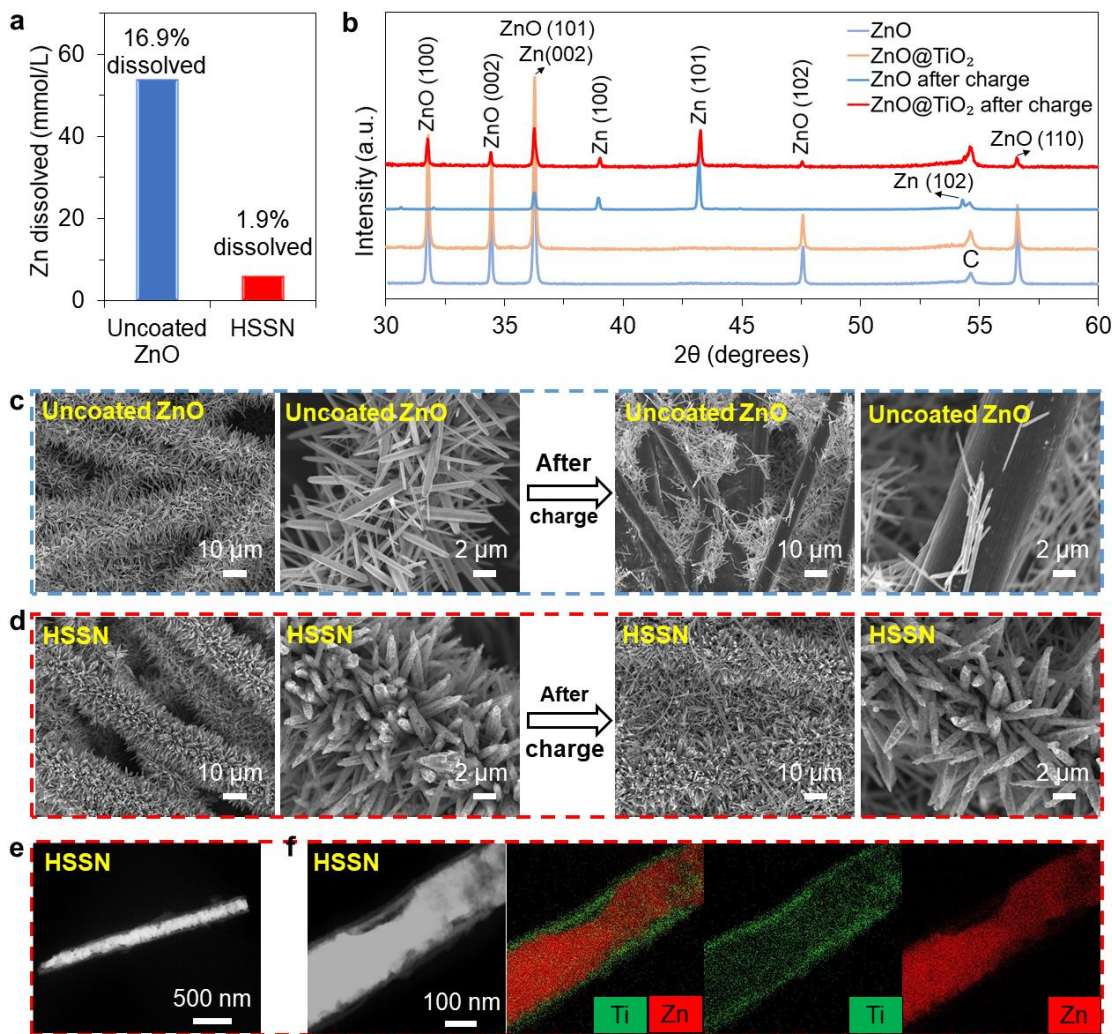
Figure 2.35 - Characterization of zinc anodes before and after charging. a, ICP results showing dissolved Zn concentration after soaking the HSSN and uncoated ZnO anodes in 4M KOH solution. 90% ZnO dissolution is suppressed in the HSSN anode, which means that the TiO$_2$ coating effectively blocks zincate ions. b, XRD patterns of uncoated ZnO and HSSN anodes before and after charging. The weak ZnO peaks of HSSN anode after charging is from residual unreacted ZnO. c,d, SEM images before and after charging uncoated ZnO anode (c) and HSSN anode (d). e, STEM image of a ZnO@TiO$_2$ nanorod after charging. f, STEM image and elemental mappings of a ZnO@TiO$_2$ nanorod after charging. The same anode sample was used to get Figure d-f.
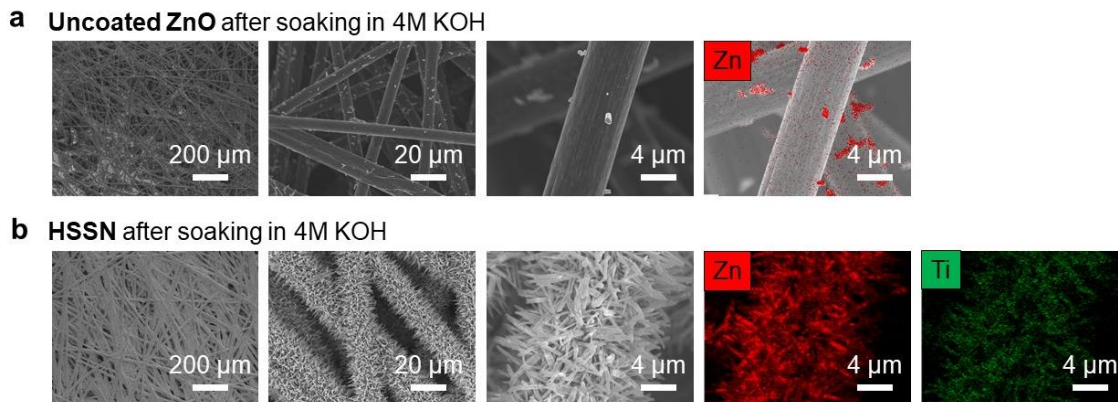
Figure 2.36 - SEM images and elemental mappings of the uncoated ZnO (a) and HSSN (b) anodes after soaking in 4M KOH solution. The reservation of Zn in the HSSN anode supports that TiO$_2$ coating can effectively block zincate ions.

The zinc-based anodes were also characterized before and after a single charge in coin cells. As shown in Figure 2.35b, XRD patterns confirmed the existence of the charging product, metallic Zn. After being charged at 0.25 mA/cm^2 for 1.5 h, the uncoated ZnO nanorod anode showed severe structural degradation. The nanorods detach from carbon paper (Figure 2.35c). In contrast, the HSSN anode has no obvious shape change (Figure 2.35d). Additionally, the HSSN anode kept nearly unchanged after five cycles (Figure 2.37). STEM images and elemental mappings of the HSSN anode after charging are presented in Figure 2.35e-f, Figure 2.38. These results indicate that the TiO$_2$ shell confines zinc active materials inside during cycling, which can be attributed to the ion-sieving effect of the TiO$_2$ shell. As shown in the N$_2$ absorption spectrum (Figure 2.39), TiO$_2$ layer has nanosized pores, which block larger zincate ion inside the shell and enable OH$^-$/H$_2$O transport through the shell. More explanation for the ion-sieving effect of the shell can be found in my previous study[81]. The porosity of TiO$_2$ can potentially be further engineered to optimize its ion-sieving performance.

a **Uncoated ZnO** anode after 5 cycles
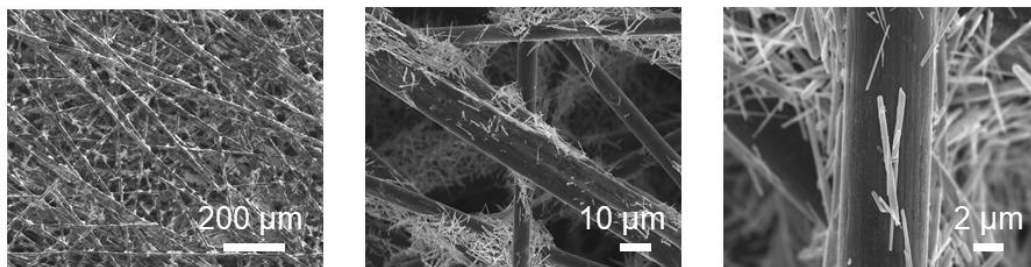
b **HSSN** anode after 5 cycles
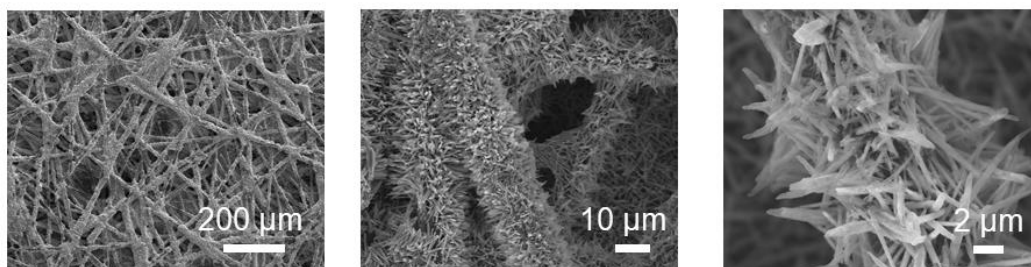
Figure 2.37 - SEM images of uncoated ZnO nanorod anode (a) and HSSN anode (b) after five galvanostatic cycles with 25 µL electrolyte. They were cycled at 0.25 mA/cm² for 2h charge and 0.25 mA/cm² discharge to 1.5V. The mass loadings of ZnO nanorods on both anodes are ~3.3 mg/cm².
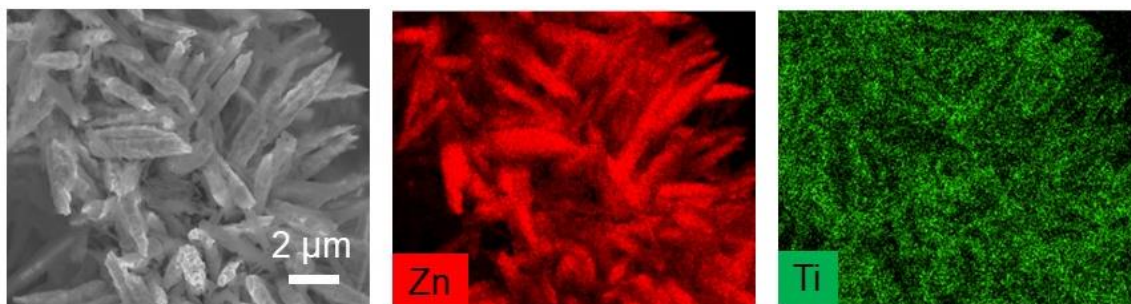
Figure 2.38 - SEM image and elemental mappings of the HSSN anode after charge.
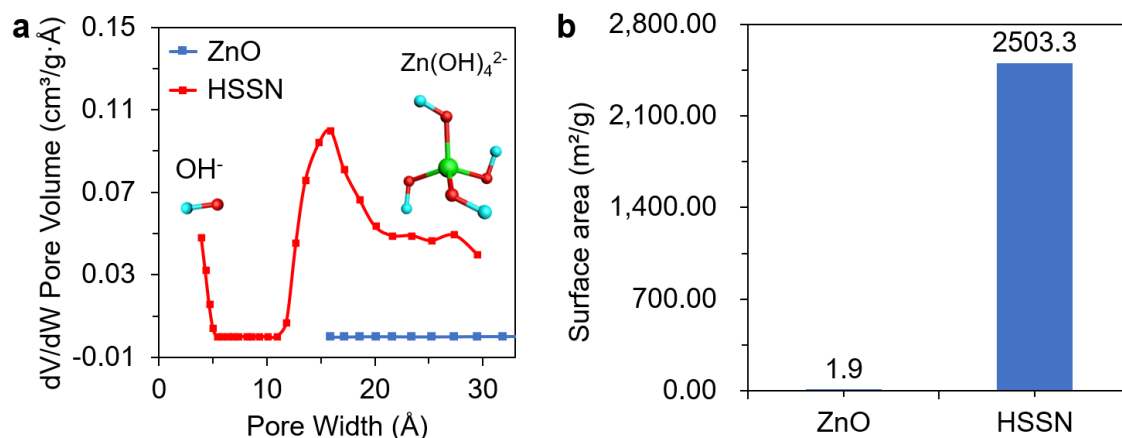
Figure 2.39 - BET pore width distribution (a) and surface areas (b) of uncoated ZnO and HSSN anodes. After TiO₂ coating, nanopores are measured, which indicates that TiO₂ coating is nanoporous.

As discussed above, an ion-sieving coating layer is necessary for nanostructured Zn anodes to suppress active material dissolution. In consideration of HER, such an ion-sieving coating layer should be HER suppressing. To evaluate the HER suppressing capability of the TiO_2 shell and its effect on the Coulombic efficiency, HER activities of TiO_2 and TiN_xO_y were investigated . TiN_xO_y (Figure 2.40) was chosen to be the control material because its uniform coating and ion-sieving property have been achieved[9]. To best represent designed anodes, ZnO was etched away from HSSN and ZnO@TiN_xO_y anodes to get TiO_2 and TiN_xO_y hollow nanorod coatings on carbon paper substrates, respectively (Figure 2.41). Three-electrode cells were then assembled in 4M KOH electrolyte with TiO_2 or TiN_xO_y electrode as the working electrode, Hg/HgO electrode as the reference electrode, and Pt foil as the counter electrode (Figure 2.42). As shown in IR-corrected polarization curves (Figure 2.43a), the HER on the TiN_xO_y electrode was more severe (higher current density at a fixed HER potential) than on TiO_2. These experimental results reveal that the TiO_2 is more hydrogen suppressive than TiN_xO_y. In addition, the HER activities of the TiO_2 electrode were also compared with the carbon paper substrate, which experimentally

72

indicates that the existence of TiO_2 coating can suppress HER (Figure 2.44). To understand the hydrogen suppressing property of TiO_2, the sheet resistance of TiO_2 and TiN_xO_y were measured using a four-point probe system (Figure 2.45). TiO_2 has lower electrical conductivity, which may be part of the reason for its lower HER activity and better HER suppressing capability. Simulations based on the force field model were also conducted to confirm the hydrogen suppressing property of TiO_2. Cluster rather than slab model was chosen because of its applicability in representing amorphous materials (Figure 2.43b)[134]. In a three-state diagram (Figure 2.43c), ΔG_H^* represents the free energy for H adsorption. The material with higher $|\Delta G_H^*|$ value possesses lower catalytic activity[131,135] and better hydrogen suppressing capability. The free energy for TiO_2 is 0.495 eV, which is higher than that of TiN_xO_y clusters (Figure 2.46 and Table 2.3). This result illustrates that TiO_2 is the most hydrogen suppressive.
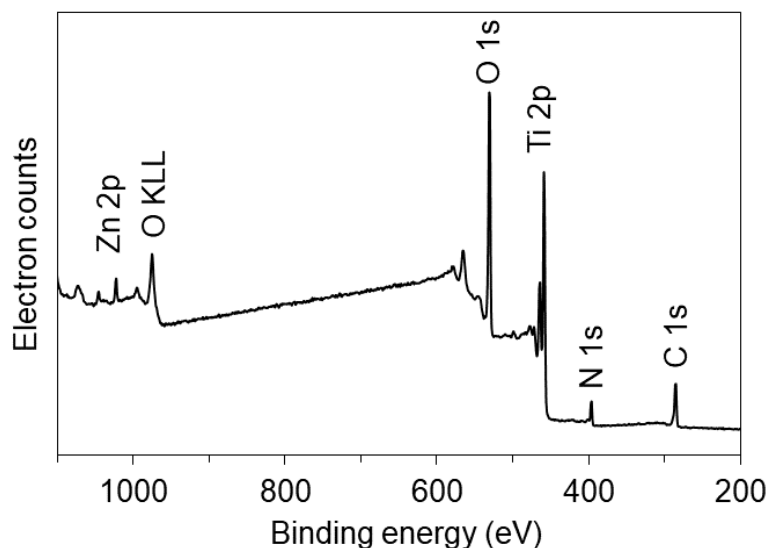
Figure 2.40 - XPS survey spectra of the $ZnO@TiN_xO_y$ anode. The atomic ratio of O to N is ~6.66 in the TiN_xO_y coating.

a CP-TiN$_x$O$_y$
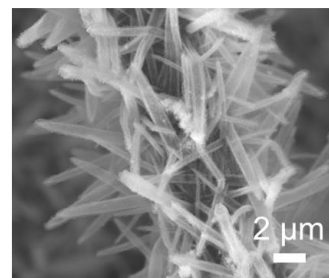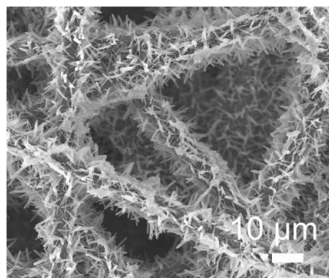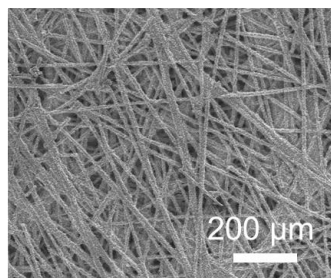
b CP-TiO$_2$
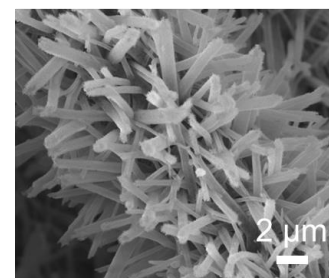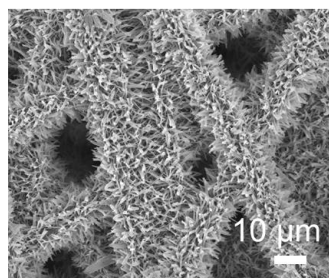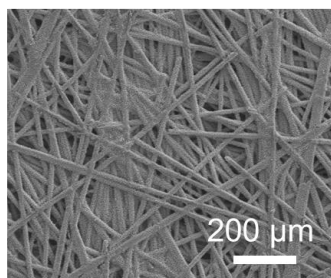
Figure 2.41 - SEM images of TiN$_x$O$_y$ (a) and TiO$_2$ (b) hollow nanorod coatings on CP substrates, which are prepared by etching away ZnO from the HSSN and ZnO@TiN$_x$O$_y$ anodes.
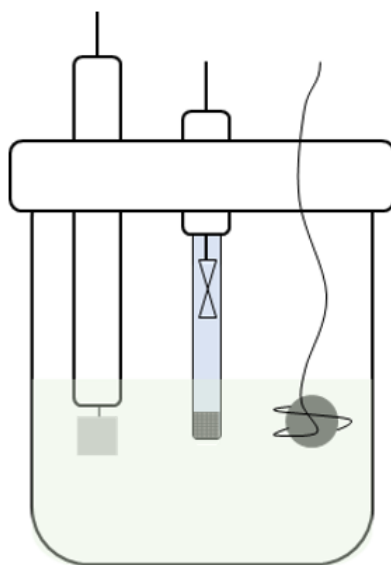
Figure 2.42 - Schematic diagram of the three-electrode cell in 4M KOH electrolyte with TiO$_2$ or TiN$_x$O$_y$ electrode as the working electrode, Hg/HgO electrode as the reference electrode, and Pt foil as the counter electrode.
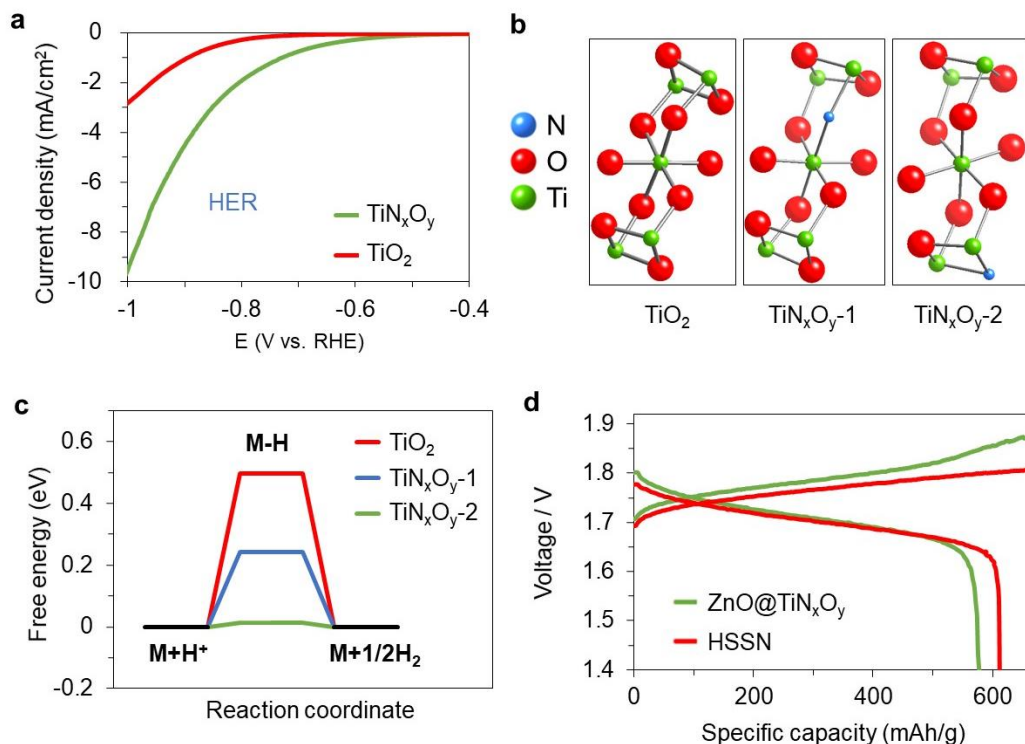
Figure 2.43 - Hydrogen suppressing property of TiO$_2$. a, IR-corrected polarization curves of TiN$_x$O$_y$ and TiO$_2$ electrodes. At any fixed potential, the hydrogen evolution on TiN$_x$O$_y$ electrode is severer than TiO$_2$ electrode. Scan rate: 2 mV/s. b,c, Basic models (b) and adsorption free energy diagram (c) of TiO$_2$, TiN$_x$O$_y$-1 and TiN$_x$O$_y$-2 clusters. d, Voltage profiles of Zn-Ni batteries with HSSN and ZnO@TiN$_x$O$_y$ as anodes. The Coulombic efficiency of the HSSN anode is higher with better HER suppressing capability.
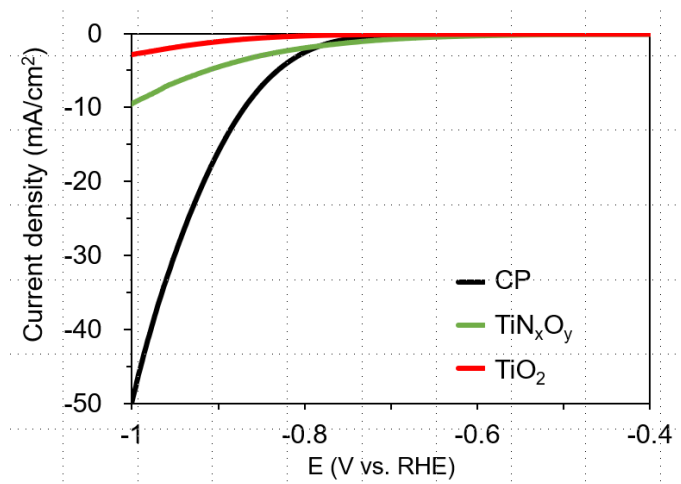
Figure 2.44 - IR-corrected polarization curves of CP substrate, TiN$_x$O$_y$ and TiO$_2$ electrodes. HER can be suppressed with the existence of TiO$_2$. CP: carbon paper. Scan rate: 2 mV/s.
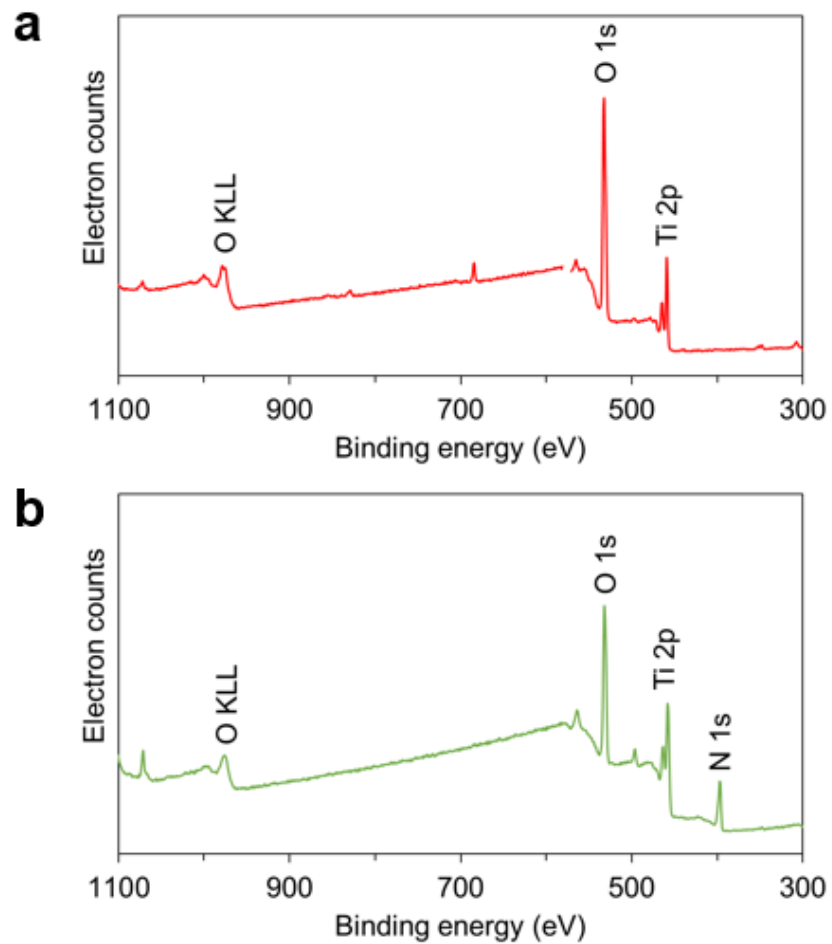
75

Figure 2.45 - TiNₓOᵧ and TiO₂ coatings. (a) XPS survey spectra of the TiO₂ coating. (b) XPS survey spectra of the TiNₓOᵧ coating. (c) Sheet resistance and resistivity of TiNₓOᵧ and TiO₂ coatings measured using a four-point probe system.
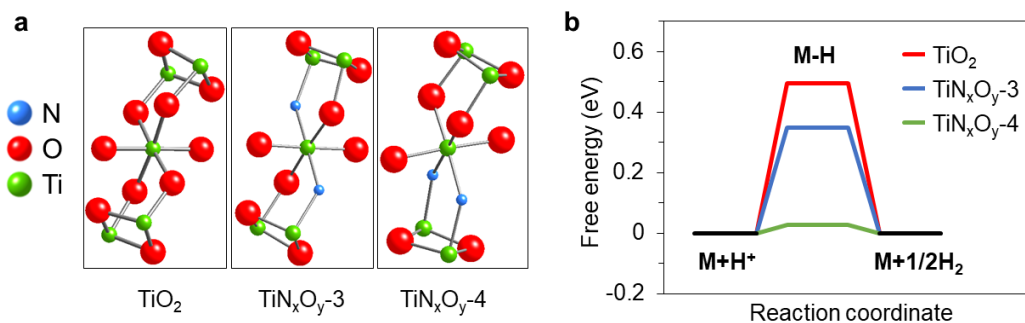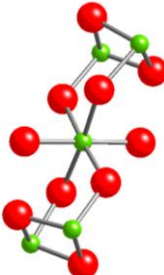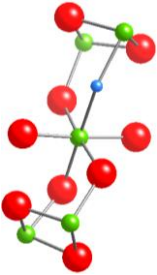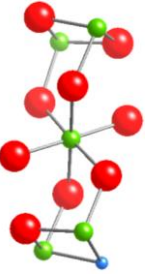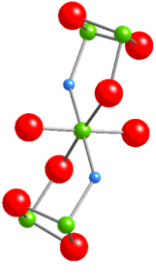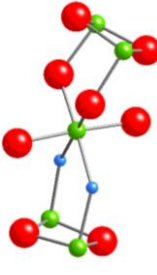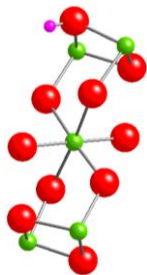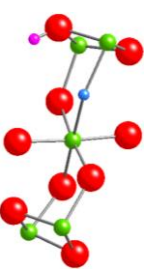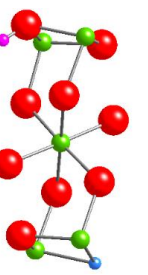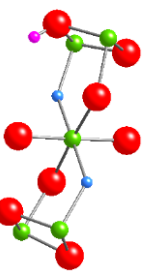
Figure 2.46 - Basic models (a) and adsorption free energy diagram (b) of TiO₂, TiNxOy-3 and TiNxOy-4 clusters.

Table 2.3 - Summary of simulated energy of clusters (M) and H adsorbed clusters (M-H), binding energy, and free energy.*

M	TiO₂	TiNxOy-1	TiNxOy-2	TiNxOy-3	TiNxOy-4
E_M	-12.282 eV	-14.865 eV	-14.378 eV	-18.086 eV	-18.058 eV
E_{M-H}	-13.547 eV	-16.382 eV	-16.125 eV	-19.498 eV	-19.792 eV
ΔE_H	0.255 eV	0.003 eV	-0.227 eV	0.108 eV	-0.214 eV
$\Delta G_H{}^*$	0.495 eV	0.243 eV	0.013 eV	0.348 eV	0.026 eV

*Atoms in clusters: pink, H; blue, N; red, O; green, Ti.

As shown in Figure 2.47 and Figure 2.48, HSSN and ZnO@TiN$_x$O$_y$ anodes have very similar ion-sieving capability. With hydrogen suppressing capability, the HSSN anode shows higher Coulombic efficiency compared to the ZnO@TiN$_x$O$_y$ counterpart. To specifically focus on Zn anodes, for all the cells shown below, cathodes with excess capacity were harvested to pair with Zn anodes. The calculation of the specific capacity of zinc anodes is based on the mass of ZnO (theoretical capacity: 658 mAh/g) if not otherwise specified. Cells were galvanostatically cycled at a charge rate of 1C and a discharge rate of 5C[136]. Anodes were cycled in pouch cells (Figure 2.49) instead of coin cells to avoid the HER on stainless steel coin cell cases[137]. They were cycled at 100% depth of discharge (DOD). Thus, the extent of side reactions on them can be directly indicated by the cell Coulombic efficiency. Higher "clean" Coulombic efficiency means fewer side reactions. The charge/discharge profiles of HSSN and ZnO@TiN$_x$O$_y$ anodes cycled in lean electrolyte (100 μL) are plotted in Figure 2.43d. Their cycling performance and rate-capability tests can be found in Figure 2.50 and Figure 2.51. The average Coulombic efficiency (93.50%) of the HSSN anode in the first 12 galvanostatic cycles is much higher than that of the ZnO@TiN$_x$O$_y$ anode (84.96%). Even though TiO$_2$ has lower electrical conductivity than TiN$_x$O$_y$, the HSSN anode showed slightly better rate capability than the ZnO@TiN$_x$O$_y$ anode, which may be because there are more pores on the HSSN anode and thus the faster OH$^-$/H$_2$O transport can be achieved through the TiO$_2$ shell (Figure 2.52). The HSSN anode achieves higher Coulombic efficiency of 93.09% than the ZnO@TiN$_x$O$_y$ anode (88.07%). In similar alkaline electrolytes with 100% DOD, most previous reports show Coulombic efficiency lower than 90% (Table 2.4).
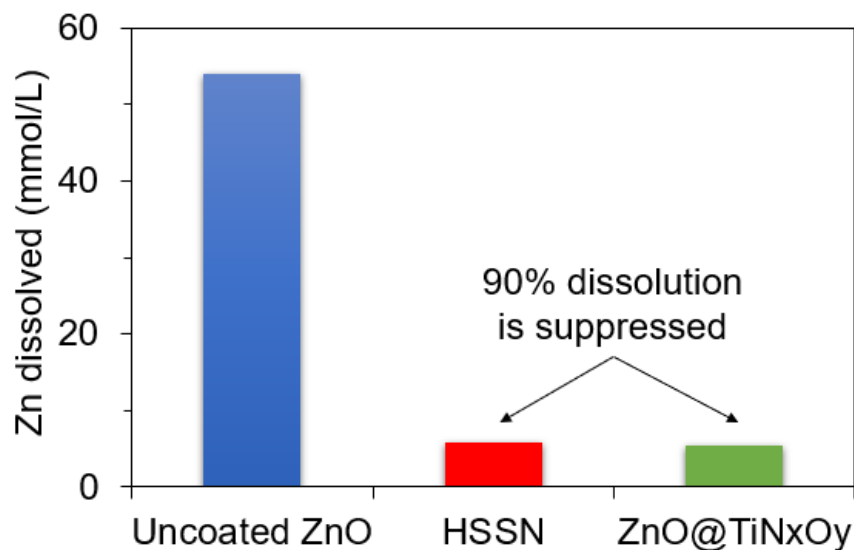
Figure 2.47 - ICP results showing dissolved Zn concentration after soaking the uncoated ZnO, HSSN and ZnO@TiN$_x$O$_y$ anodes in 4M KOH solution. 90% ZnO dissolution is suppressed in the HSSN and ZnO@TiN$_x$O$_y$ anodes. HSSN and ZnO@TiN$_x$O$_y$ anodes have very similar ion-sieving capability.
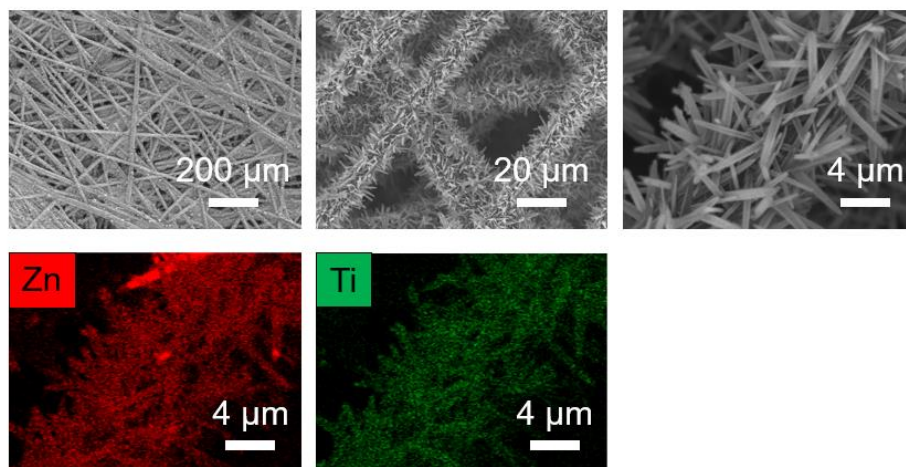
Figure 2.48 - SEM images and elemental mappings of the ZnO@TiN$_x$O$_y$ anode after soaking in 4M KOH solution. The reservation of Zn in the ZnO@TiN$_x$O$_y$ anode supports that TiN$_x$O$_y$ coating can effectively block zincate ions.
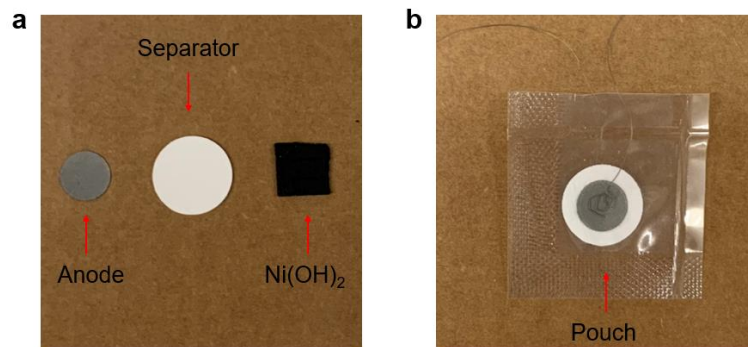
Figure 2.49 - The cell components (a) and assembled pouch cell (b). Separator has 1.5 cm diameter. The anode has 1 cm diameter.
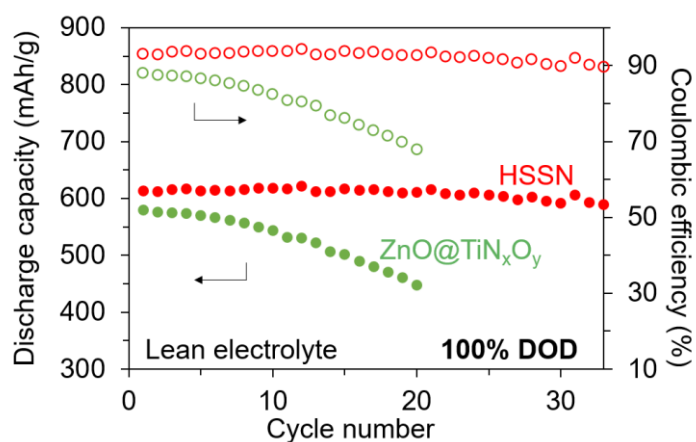
Figure 2.50 - Cycling performance of the ZnO@TiN$_x$O$_y$ and HSSN anodes in lean electrolyte at 100% DOD.
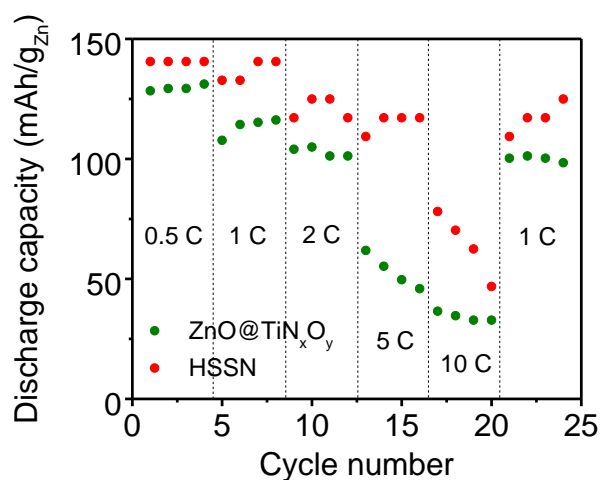
Figure 2.51 - Cycling performance of the HSSN and ZnO@TiN$_x$O$_y$ anodes at various C rates. State of charge: 20%.
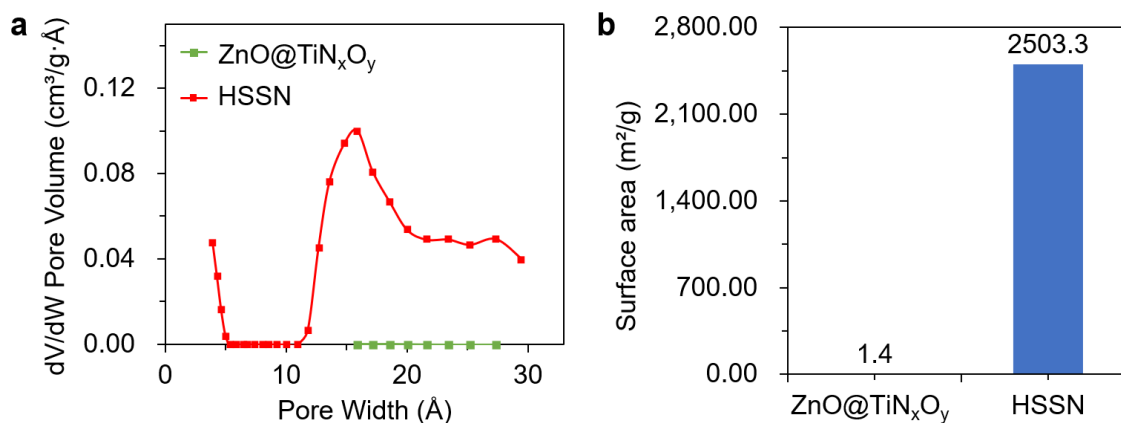
Figure 2.52 - BET pore width distribution (a) and surface areas (b) of HSSN and ZnO@TiN$_x$O$_y$ anodes.

Table 2.4 - Comparison of Coulombic efficiency of the HSSN anode with previously reported zinc-based anodes (100% depth of discharge) in alkaline electrolytes.

Anode material	Coulombic efficiency (%)
Ca(OH)$_2$-coated ZnO[138]	29.10
Sn$_6$O$_4$(OH)$_4$-coated ZnO[139]	37.50
ZnO nanoplate[114]	69.15
Ag-modified ZnO[140]	71.43
ZnAlSb-LDH[95]	78.10
ZnO/SnO$_2$[141]	84.62
ZnO@RGO[98]	85.00
ZnO microspheres[75]	86.63
ZnO@Ag@Polypyrrole[142]	89.00
LDOs[124]	89.42
Ag/ZnO[143]	89.67
IZO[121]	91.04
SnO$_2$@ZnO[144]	91.19
Ag-LDH[125]	93.19
This work	**93.50**

As shown in Figure 2.53a and Figure 2.54, when cycled at 40% DOD in lean electrolyte, the HSSN anode (with 1.05 mg/cm^2 ZnO) demonstrated long-term stable

cycling for more than 170 cycles. It was confirmed that there was no capacity contribution from the TiO$_2$ shell during the electrochemical reactions (Figure 2.55). When cycled at 100% DOD in lean electrolyte, the HSSN anode (with 1.5 mg/cm^2 ZnO) achieved an average Coulombic efficiency of 93.5% and average discharge capacity of 616 mAh/g in the first 12 galvanostatic cycles. The capacity fading occurs after 33 cycles. The battery failure can be attributed to (1) the structural collapse of the HSSN anode (Figure 2.56) due to the shape and volume changes of Zn/ZnO inside the shell, and (2) the limited mass transfer of Zn species caused by electrolyte decomposition and hydrogen accumulation. The HSSN anode was also evaluated in a beaker cell with a large amount of ZnO-saturated electrolyte. As shown in Figure 2.53b, the HSSN anode (with 1.6 mg/cm^2 ZnO) was cycled more than 350 times with Coulombic efficiency of 94.3% and a discharge capacity of 621 mAh/g. Voltage profiles for the batteries shown in Figure 2.53a and b can be found in Figure 2.57. From the above cycling results, it can be concluded that the cycle life of Zn anodes in lean electrolyte is much shorter than in a large amount of ZnO-saturated electrolyte. This can be explained by the electrochemistry of alkaline Zn anodes. In a large amount of ZnO-saturated electrolyte, the effect of minor electrolyte decomposition can be minimized with excess water. Moreover, there is excess zincate in the electrolyte, which is the active material for Zn anodes. With a large capacity contribution from the zincate supplied from the electrolyte, the long cycle life of Zn anodes can be achieved yet it is inauthentic. In lean electrolyte (100 μL), batteries fail quicker as a result of complicated synergistic effects caused by electrolyte decomposition and limited mass transfer of Zn species. However, it is still necessary to cycle anodes in lean electrolyte to evaluate their true performance which can represent practical situations despite their short cycle life.
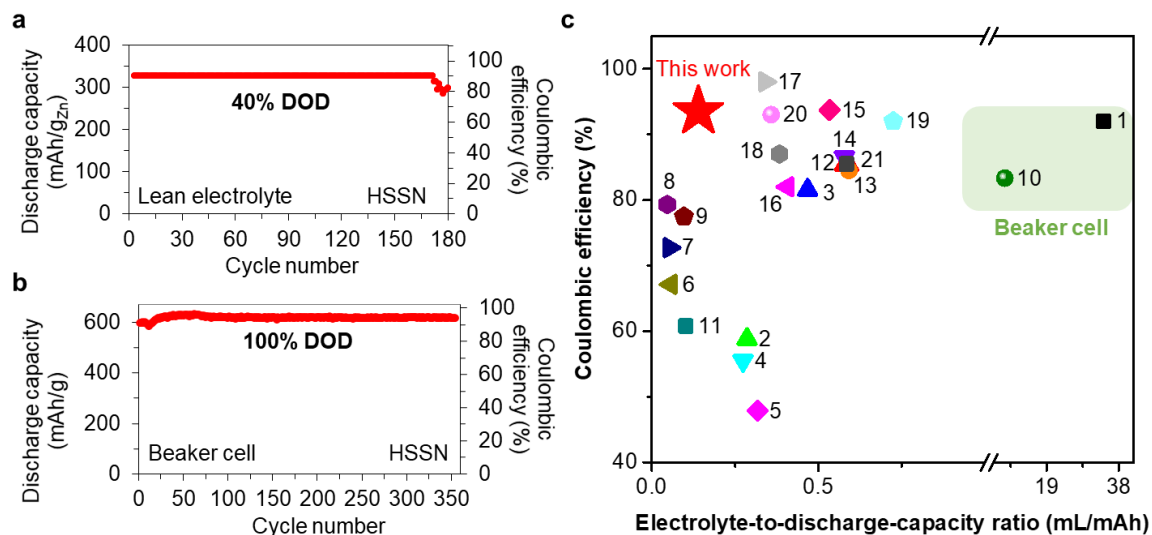
Figure 2.53 - Electrochemical performance of HSSN anodes. a, Cycling performance of the HSSN anode in lean electrolyte at 40% DOD. b, Cycling performance of the HSSN anode in a beaker cell with a large amount of electrolyte at 100% DOD. c, Comparison of the HSSN anode and previously reported anodes (with 100% DOD) in aspects of E/DC ratio and Coulombic efficiency.
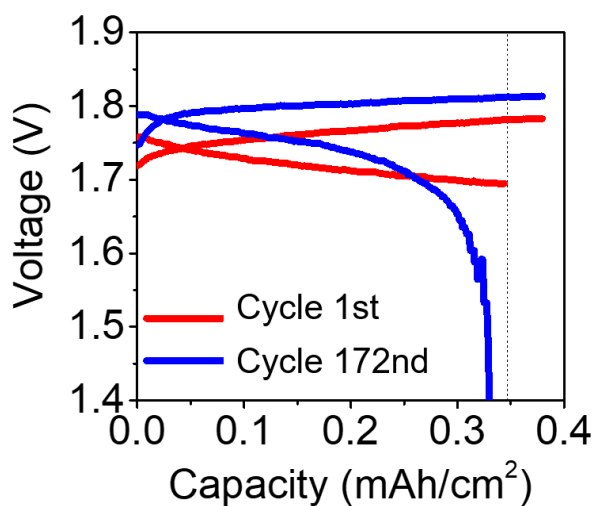
Figure 2.54 - Charge-discharge profiles of the HSSN anode in lean electrolyte at 40% DOD.
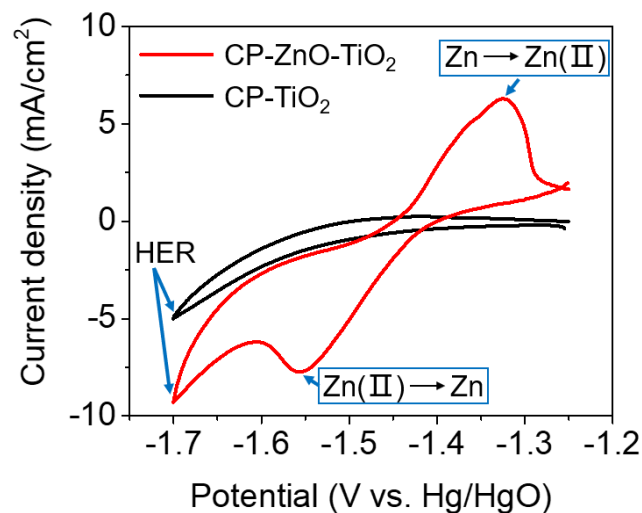
Figure 2.55 - CV curves of CP-TiO₂ and HSSN electrodes. There is no capacity contribution from TiO₂ during the electrochemical reaction. Scan rate: 10 mV/s.
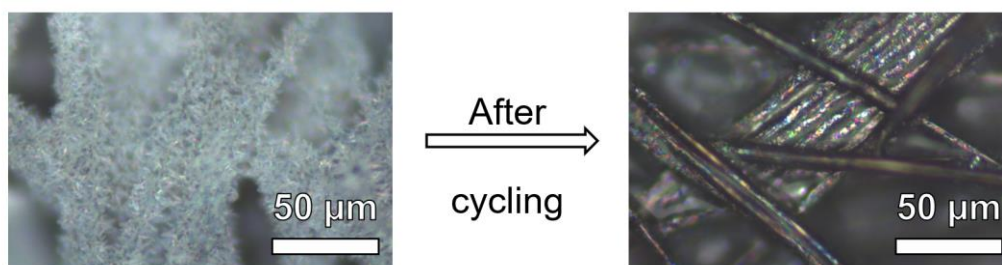
Figure 2.56 - Optic microscope images of the HSSN anode before and after battery failure.
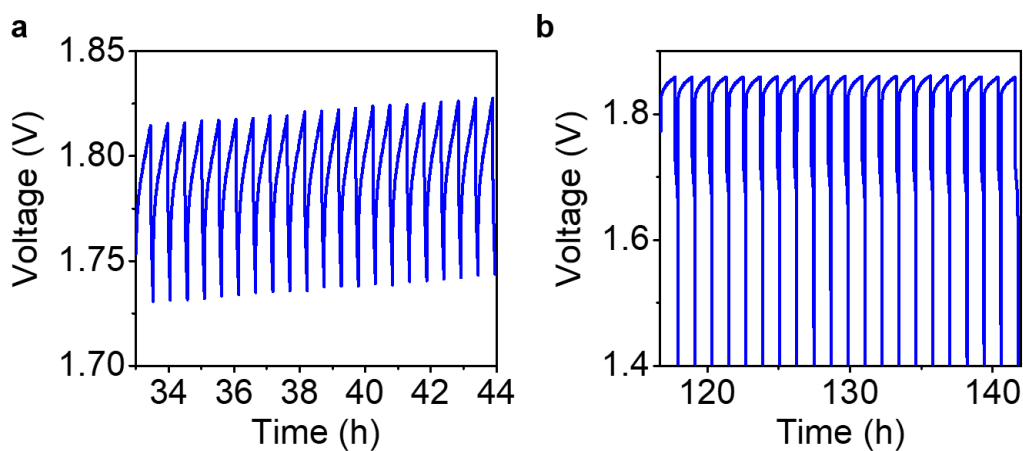
Figure 2.57 - Voltage profiles (from cycle 50th to 70th) of the HSSN anode cycled in lean electrolyte at 40% DOD (a) and a beaker cell with a large amount of electrolyte at 100% DOD (b).

Electrolyte-to-discharge-capacity (E/DC) ratio is also critical for device-level energy density and is crucial for practical applications. It has been paid attention in lithium-based non-aqueous batteries[145–147]. Recently, researchers in the zinc-based battery field have begun emphasizing the low E/DC ratio.[148,149] The tested Coulombic efficiency of alkaline Zn anodes is highly correlated to the E/DC ratio. Thus, it is necessary to provide E/DC ratios to get a fair comparison on the Coulombic efficiency of different Zn anode materials. However, only a few previous works (summarized in Table 2.5) reported this ratio or provided necessary information for its calculation. Here, they were summarized and compared to HSSN anode in terms of Coulombic efficiency and E/DC ratio in Figure 2.53c. Notably, to get a comparison on "clean" Coulombic efficiency of different Zn anodes, only deeply cycled Zn anodes with 100% DOD are listed above. Partially utilized (DOD<100%) metallic zinc anodes are not included in the comparison because their Coulombic efficiency cannot indicate the extent of side reactions occurring on Zn anodes. In comparison, HSSN anode achieves a superior Coulombic efficiency (93.5%) at a low E/DC ratio (0.14 mL/mAh), which suggests the advance of the designed functionally coated Zn anodes. With the featured HER suppressing core/shell Zn anode: (1) Zn species are confined inside the shell so there is minimized active material loss; (2) minimized HER and less electrolyte decomposition can be achieved with the HER suppressing property. These enable HSSN anode to achieve high Coulombic efficiency in lean electrolyte. The overall areal and specific discharge capacities of the HSSN anode were ~0.9 mAh/cm^2 and ~91 mAh/g, respectively, after considering the mass of the current collector. Due to its specially featured core/shell nanorod structure, its overall capacity is unable to meet the requirement for practical Zn anodes (11.7 mAh/cm^2)[149]. However, the design principal

presented here may help guide further research to achieve practically high energy-density

Zn anodes.

Table 2.5 - Comparison of HSSN anode with previously reported zinc-based anodes in aspects of electrolyte-to-discharge-capacity (E/DC) ratio and Coulombic efficiency in alkaline electrolyte. The depth of discharge of Anode No. 1 - Anode No. 22 are 100%. The depth of discharge of Anode No. 0 is 40%.

Anode No.	Anode material	E/DC ratio (mL/mAh)	Coulombic efficiency (%)
0	Zn sponge[79]	0.0062	~100
1	Backside-plating zinc[150]	34.09	92.0
2	ZnO@C[81]	0.29	58.8
3	ZnO@TiN$_x$O$_y$[9]	0.47	81.6
4	Zn-pome[82]	0.27	55.5
5	ZnO lasagna[151]	0.32	47.9
6	ZnO nanoparticle[152]	0.06	67.1
7	ZnO particle[152]	0.05	72.7
8	ZnO nanorod[152]	0.05	79.3
9	Calcium zincate[153]	0.10	77.5
10	Zn@Bi$_2$O$_3$-CaO-ZnO glass[154]	8.00	83.3
11	IHCP-ZnO/C[155]	0.10	60.8
12	Commercial ZnO[156]	0.58	85.5
13	TRIEN-ZnO[156]	0.59	84.5
14	EN-ZnO[156]	0.58	86.5
15	DIEN-ZnO[156]	0.53	93.7
16	Cr$_x$ZnO[157]	0.41	82.0
17	Ni$_x$Zn$_{(1-x)}$O[158]	0.34	98.0
18	Microcrystalline ZnO[159]	0.38	87.0
19	Fe$_{0.01}$ZnO[160]	0.72	92.0
20	ZnO-LiOH[161]	0.36	93.0
21	Mg$_x$Zn$_{1-x}$O[162]	0.58	85.5
22	**This work**	**0.14**	**93.5**

2.4.4 Conclusion

In summary, a zinc anode design has been reported , namely sealing sub-micron-sized ZnO with a HER suppressing and ion-sieving layer, to overcome simultaneously passivation, dissolution, and hydrogen evolution issues in alkaline electrolytes. A ZnO nanorod anode and TiO_2 shell were chosen to demonstrate this concept. The fabricated HSSN anode achieves superior reversible deep cycling performance at lean electrolyte. While the Coulombic efficiency of the HSSN anode is higher than that of most of the previously reported zinc anodes, it needs to be further improved to approach the efficiency of LIBs (99.9%). Optimization of the shell material, from aspects of pore size, porosity, and surface charge, may lead to further improvement of anode performance and stability. Other materials with controlled ion-sieving and HER suppressing properties also have the potential to be applied as the shell material. This design principle can potentially be applied to other morphologies (e.g. particles) of starting materials for large scale production. The mechanistic understanding and design principle reported in this study may also guide future design of other rechargeable high-energy aqueous batteries.

2.5 Conclusion

Passivation, shape change, dendrite growth, and hydrogen evolution are four main challenges for Zn anodes in alkaline electrolyte. In this chapter, four types of zinc anodes have been designed and synthesized to overcome multiple issues simultaneously (Table 2.6) and improve their reversibility. These anodes include graphene oxide-modified (Zn@GO), lasagna-inspired (ZnO@GO), sealed (ZnO@TiN$_x$O$_y$), and hydrogen-evolution-suppressing (HSSN) anodes, which show improved deep cycling performance

when cycled at lean electrolyte compared with control samples. The mechanistic understanding and design principle reported here may also guide future design of other rechargeable high-energy aqueous batteries. Dendrite growth issue will be discussed in *Chapter 3*.

Table 2.6 - Summary of four types of zinc anodes in this chapter.

Challenges	Zn@GO	Lasagna	ZnO@TiN$_x$O$_y$	HSSN
Passivation	-	Partially solved	Solved	Solved
Shape change	Solved	Solved	Solved	Solved
Hydrogen evolution	-	-	-	Solved

CHAPTER 3.   ELUCIDATING THE MECHANISM FOR SPATIALLY CONTROLLED DEPOSITION

In aqueous electrolytes, zinc anodes suffer from severe dendritic metal deposition. The regulation of Zn by inducing Zn-alloying metals has been reported. However, the underlying mechanisms have remained elusive. Here, the alloying mechanisms for the regulation of Zn were reported for the first time. Spatially controlled and nondendritic Zn deposition was achieved by introducing a Zn-alloying and soluble metal (Ag) on Zn anodes to nucleate and accommodate Zn. The Ag-modified Zn anode exhibited superior overall cycling performance compared with previously reported deeply cycled Zn anodes in alkaline electrolytes. Furthermore, the spatially controlled Zn deposition was visualized in operando for the first time using an optical microscope. The alloy-seeding design principle can potentially be applied to improve the rechargeability of other metal anodes.

3.1   Introduction

In aqueous electrolytes, zinc anodes suffer from severe nonuniform and dendritic metal deposition[163], which results in the capacity decay over cycling. Spatially controlled metal deposition using alloy anodes has been demonstrated to be effective in solving dendrite problems of lithium metal anodes[164,165]. For Zn anodes, the addition of Ag[123,125,140,143,166,167], Au[168], or Cu[169] has been reported to improve the cycle life. However, the mechanisms associated with alloy properties for the regulation of Zn by inducing these Zn-alloying metals have not been investigated yet. Moreover, even though scanning electron microscopy (SEM) images have shown uniform Zn deposition, selective Zn

deposition has not been clearly visualized on those anodes. Therefore, the origin of the spatial control of Zn deposition on alloy anodes remains elusive.

Here, the alloying mechanisms for the regulation of Zn were reported for the first time. It is discovered experimentally and computationally that in an alkaline electrolyte: (1) the Zn metal nucleation barrier substantially differs among different substrates, with some Zn-soluble materials showing zero potential barrier; (2) the formation of alloys between Zn and Zn-alloying materials is spontaneous during the electrochemical reduction of Zn(II), as a result of a negative Gibbs free energy of formation of zinc alloys. These discoveries suggest it feasible to nucleate and accommodate Zn metal. As a proof of concept, a spatially controlled and uniform Zn deposition through heterogeneous seeded growth has been achieved using Ag seeds. The spatially controlled Zn deposition has also been visualized in operando for the first time using an optical microscope. When the molar ratio between deposited Zn and Ag was controlled at 1, 2, and 3, the resultant Ag-nanoparticle-loaded carbon paper (C-Ag) achieved superior cycle lives of 75, 187, 2,501, and 752 cycles, respectively, compared with 273, 33, and 38 cycles for C electrodes, respectively. In addition, the Ag-modified Zn anode exhibits superior overall cycling performance compared with previously reported deeply cycled Zn anodes in alkaline electrolytes.

3.2   Experimental Section

Preparation of metal thin films. A Cu foil (35 μm) was rinsed with 1% nitric acid to remove surface coatings and oxides before it was used as a substrate in experiments. First, a 10 nm-thick Ti layer was deposited onto Cu foils as the adhesion layer. Thin films

of Ag, Au, Cu, Ti, Fe, Pt and Ni with a thickness of 100 nm were then directly deposited onto the Cu foils by e-beam deposition.

Preparation of Ag patterned substrates. Carbon paper, stainless steel and Ni foils were used as substrates for the Ag-patterned coatings. Stainless steel meshes (Dexmet) were used as masks for the substrates. A Ag/Ti film (100 nm/10 nm) was then evaporated onto the substrates by e-beam deposition. Finally, the mask was removed to obtain Ag-patterned substrates. For the high-magnification Ag-patterned C substrate, a ~50 nm-thick C layer was first evaporated onto a Cu foil. Stainless steel meshes (TWP) were used as a substrate mask. A Ag/Ti film (100 nm/10 nm) was then evaporated onto the substrate by e-beam deposition. Finally, the mask was removed to obtain Ag-patterned substrates.

Preparation of the C-Ag electrode. To prepare the Ag slurry, Ag nanoparticles (Aldrich) and polyvinylidene difluoride binder (PVDF, Aldrich) were mixed with a mass ratio of 8:1 in *N*-methylpyrrolidone (NMP, Aldrich). The slurry was then stirred overnight to be uniform. After the slurry was cast onto a carbon paper substrate, the electrode was dried on a hotplate (90°C) overnight.

Preparation of the C electrode loaded with carbon black. To make a carbon black slurry, carbon black (MTI) and PVDF were mixed with a mass ratio of 8:1 in NMP. The slurry was then stirred overnight to be uniform. After the slurry was cast onto a carbon paper substrate, the electrode was dried on a hotplate (90°C) overnight.

Material characterization and measurements. The morphological and compositional analyses were carried out using scanning electron microscopy (SEM, Hitachi SU 8230), transmission electron microscopy (TEM, Hitachi HT7700, FEI Tecnai

F30, and JEOL 100 CX-II), and scanning transmission electron microscopy (STEM, Hitachi HD-2700). The X-ray diffraction patterns (XRD, Panalytical XPert PRO Alpha-1) were collected with Cu Kα radiation. X-ray photoelectron spectroscopy (XPS) was performed with a Thermo Scientific K-Alpha system. All ex situ studies with SEM, TEM and XRD were conducted after the tested electrodes were disassembled and thoroughly washed with deionized water. Electrochemical Zn plating/stripping and cyclic voltammetry were conducted using a VSP system (BioLogic). Battery cycling tests were carried out using a LANHE system operating in galvanostatic mode.

Measurement of Zn nucleation barrier. Three-electrode electrochemical cells were constructed that consisted of the substrate of interest as the working electrode, Hg/HgO as the reference electrode and Zn foil (Alfa Aesar) as the counter electrode. Zn metal was galvanostatically deposited onto the working electrode at 3 mA cm^{-2} in 5 mL of a ZnO-saturated 4 M KOH (Sigma Aldrich) aqueous electrolyte.

Operando optical microscope characterization. Two-electrode electrochemical cells were constructed that consisted of the substrate of interest as the working electrode and Zn foil as the counter electrode. A ZnO-saturated 4 M KOH aqueous solution was used as the electrolyte. The cells were probed using a Leica DMC2700 microscope with reflected dark-field illumination. Most of the images and videos were captured through an air-immersion objective (Leica N PLAN L 5X 0.50 BD). All the in-operando experiments were performed at room temperature and ambient pressure.

Electrochemistry. The zinc anodes were cut into round disks with diameters of 1 or 1.6 cm. The counter electrodes (cathodes) were Ni(OH)$_2$ harvested from commercial Ni-

Zn AA batteries (PowerGenix). To specifically focus on the Zn anodes, $Ni(OH)_2$ cathodes with excess capacity (~40 mAh cm^{-2}) was paired with the prepared anode. The diameter of the separator disks was 1.6 cm.

Pouch-type batteries were assembled using Ampac's SealPAK. The aqueous electrolyte consisted of 4 M KOH (Sigma Aldrich), 2 M KF (Alfa Aesar) and 2 M K_2CO_3 (Alfa Aesar) and was saturated with ZnO. Ti wires were used as electrode terminals.

For the ex situ XRD studies of C-Ag electrodes (1 cm diameter disk) in different charge/discharge states, Celgard 3501 and glass fiber/Freudenberg 700/28K separators were used with 300 µL of electrolyte. The mass loading of the Ag nanoparticles was approximately 0.45 mg cm^{-2}. Cells were galvanostatically precycled for 9 cycles. The C-Ag electrodes were charged at 1.491 mA mg_{Ag}^{-1} until a 2 V cut-off voltage was reached or when their charge capacities reached the desired values. These anodes were then discharged at 1.491 mA mg_{Ag}^{-1} to a cut-off voltage of 1.2 V or to the desired voltages for XRD studies.

For the battery cycling tests with the C and C-Ag anodes, Celgard 3501 and Freudenberg 700/28K separators were used with 300 µL of electrolyte. During charging, zincates in the electrolyte were electrochemically reduced at the anode. Electrochemically reducing all of the zincate in the electrolyte corresponded to a capacity of ~2.7 mAh. The anodes were round disks with a diameter of 1 cm. The mass loading of Ag nanoparticles and carbon black (CB) powders was approximately 0.2 mg cm^{-2}. The calculation of specific capacity was based on the mass of Ag/CB if not otherwise specified because the quantity of deposited Zn varied over cycles. Cells were galvanostatically activated for 20 cycles.

The electrodes were charged at 14.91 mA $mg_{Ag/CB}^{-1}$ until a 2 V cut-off voltage was reached or their charge capacities reached 497, 994, and 1,491 mAh $g_{Ag/CB}^{-1}$ ("Zn:Ag=1", "Zn:Ag=2" and "Zn:Ag=3" were used to represent charge conditions on both electrodes). Correspondingly, the areal capacities were ~0.1 mAh cm^{-2}, ~0.2 mAh cm^{-2}, and ~0.3 mAh cm^{-2}, in which ~2.5%, ~5%, ~7.5% of the electrolyte capacity was utilized. These anodes were fully discharged at 14.91 mA $mg_{Ag/CB}^{-1}$ to a cut-off voltage of 1.2 V. The charge/discharge current density was ~2.4 mA cm^{-2}. To minimize the effect of hydrogen evolution on cyclic stability, ~7.5% of zincates from the electrolyte were consumed at most because the depletion of zincates would make water decomposition more severe.

For the battery cycling tests with the C-Zn and C-Ag-Zn anodes, glass fiber separators were used with 100 μL of electrolyte. The anodes were round disks with a diameter of 1.6 cm. The mass loading of the Ag nanoparticles was approximately 1.2 mg cm^{-2}. Cells were fully discharged and then recycled. During charging, a constant current charge (CCC, 0.625 mA cm^{-2})-constant voltage charge (CVC, 1.85 V) protocol was employed until the areal charge capacity exceeded 0.625 mAh cm^{-2} or the CVC current decreased to less than 0.05 mA cm^{-2}. The procedure was switched from CCC to CVC when the cell voltage reached 1.85 V. Charging was followed by a discharge at 0.625 mA cm^{-2} until the cell voltage reached 1.2 V.

In beaker-type batteries, 5 mL of ZnO-saturated 4 M KOH was used as the electrolyte. A cyclic voltammogram experiment was carried out in the beaker cell using a three-electrode setup that consisted of the substrate of interest as the working electrode, Hg/HgO as the reference electrode, and Zn foil as the counter electrode. To make the C-

Zn and C-Ag-Zn anodes, ~1 mAh cm^{-2} Zn was deposited onto the C and C-Ag electrodes after 12 activation cycles. Zn foil was used as the counter electrode.

Calculations. The theoretical specific capacity of the Ag electrode was calculated by Equation 8.

$$C_T\left(mAh\ g_{Ag}^{-1}\right) = \chi * \frac{1}{MW_{Ag}} * \frac{nF}{3.6}$$ (8)

where χ is the number of Zn atoms that can alloy with a Ag atom. MW_{Ag} is the molar weight of Ag element, n is the number of electrons transferred in the relevant reaction, and F is the Faraday's constant. For the Zn-Ag alloy, $n = 2$, χ ranges from 1 to 3.

Discharge-capacity-to-electrolyte (DC/E) ratio (Equation 9):

$$DC/E\ ratio = measured\ discharge\ capacity/electrolyte\ volume$$ (9)

Statistical analysis of discharge capacities over cycling. To best present cyclic stabilities of anodes over cycling, relative standard deviations of their discharge capacities over cycling were calculated. According to statistical theory, the mean value $(\overline{DC})$, standard deviation (SD) and relative standard deviation (RSD) were calculated by the following formulas (Equation 10-12).

$$\overline{DC} = \frac{DC_1 + DC_2 + \cdots + DC_n}{n}$$ (10)

$$SD = \sqrt{\frac{\sum_{i=1}^{n}(DC_i - \overline{DC})^2}{n-1}} \tag{11}$$

$$RSD = \frac{SD}{\overline{DC}} \times 100\% = \frac{\sqrt{\dfrac{\sum_{i=1}^{n}(DC_i - \overline{DC})^2}{n-1}}}{\overline{DC}} \times 100\% \tag{12}$$

where n is the cycle number. DC_i is the discharge capacity at cycle i[th], and $\overline{DC}$ is the average discharge capacity.

Density functional theory (DFT) calculations. DFT calculations were performed using VASP[170,171] within the generalized gradient approximation treatment of exchange and correlation effects of Perdew, Burke, and Ernzerhof.[172] Projector-augmented wave pseudopotentials were used for all calculations[173] with all forces converged to be less than 0.01 eV/Å with a planewave basis set cutoff energy of 500 eV. K-point sampling of the first Brillouin zone in the bulk materials was converged with a $10 \times 10 \times 10$ mesh using the sampling scheme of Monkhorst and Pack[174] for simple cubic $Zn_{0.5}Ag_{0.5}$ and a $10 \times 10 \times 6$ mesh for Zn. Sampling for slab surface models was scaled for relative size of the unit cell based on the convergence found for the bulk materials. For Zn, the 001 and 100 surfaces were studied; these models were both converged at **7** layers of slab thickness. For $Zn_{0.5}Ag_{0.5}$, the 110 and 001 surfaces were studied; these models were converged at 9 and 7.5 layers of slab thickness, respectively.

Dissolution energies of Zn atoms were calculated relative to converged slab supercell models with reference to an isolated Zn atom in a box with 25 Å side length. Supercell models were constructed such that Zn vacancies in the Zn-deficient supercell

models were at least 8 Å apart from one another. Dissolution energy was computed as follows (Equation 13):

$$E_{diss} = (E_{slab-Zn} + E_{Zn}) - E_{slab} \tag{13}$$

Where E_{diss} is the energetic cost to remove a Zn atom, E_{slab} is the energy of the pristine slab model, E_{Zn} is the energy of the isolated Zn atom, and $E_{slab-Zn}$ is the energy of the Zn-deficient slab model. With this convention, and endothermic removal event corresponds to a positive energy.

Thermodynamic assessment of Ag-Zn. The Gibbs free energy of formations at room temperature of Zn and multiple Zn_xAg_{1-x} alloy phases were calculated using the CALPHAD technique[175].

3.3 Results and Discussion

3.3.1 Choice of seed materials

7 common metallic substrates (Ag, Au, Cu, Ti, Fe, Pt and Ni) were screened that can potentially alloy with Zn. These substrates were prepared by evaporating the corresponding metal to a thickness of 100 nm onto Cu foils. The corresponding binary phase diagrams[176] are shown in Figure 3.1a and Figure 3.2. The solubility zone is labeled as (Zn). Carbon-fiber paper, which does not alloy with or dissolve in zinc [176], was also added in the above series as a control sample. A three-electrode electrochemical cell was constructed that consisted of the substrate of interest as the working electrode, Hg/HgO as the reference electrode and Zn foil as the counter electrode. Zn metal was galvanostatically

deposited onto the working electrode at 3 mA cm^{-2} in an alkaline electrolyte (ZnO-saturated[136] 4 M KOH aqueous solution).
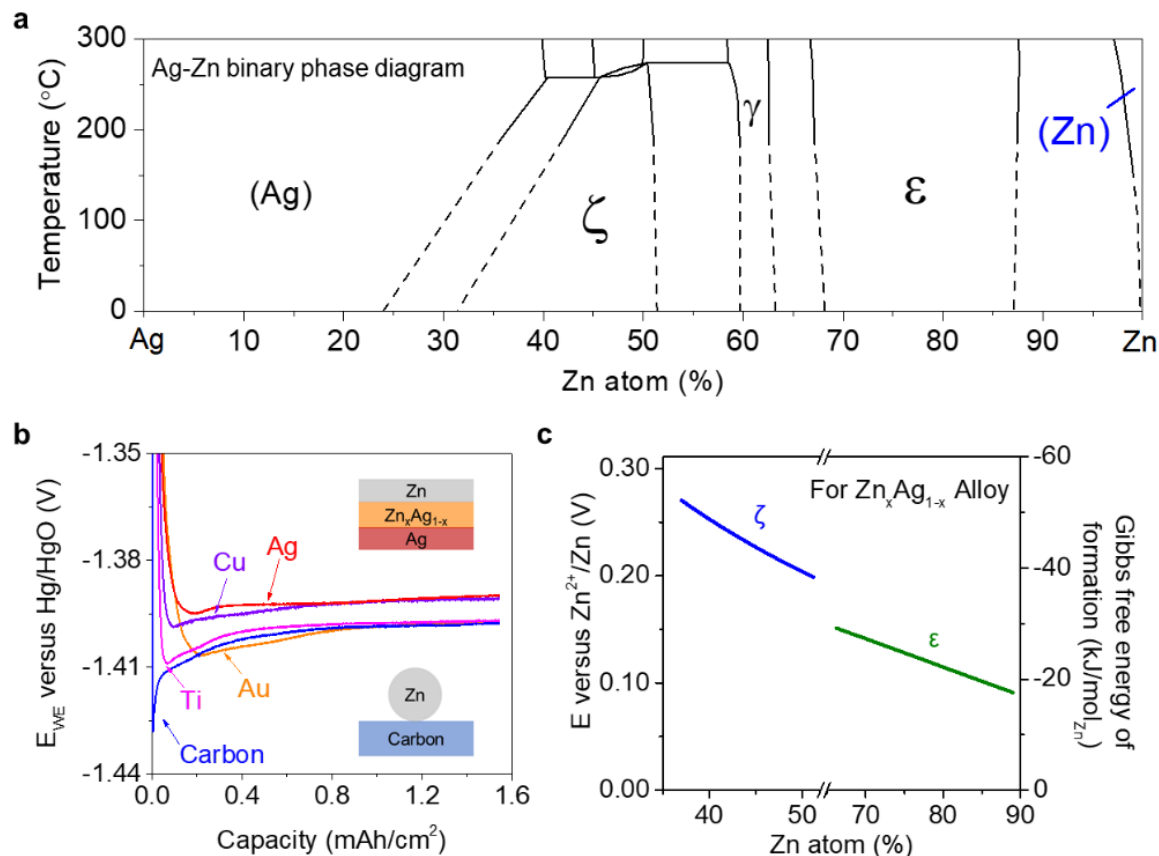
Figure 3.1 - Ag as the seed for electrochemical Zn plating. a, Phase diagram of Zn with Ag. The region where Ag dissolved in Zn is labeled as (Zn) with a blue color. b, Voltage profiles of galvanostatic Zn deposition on various substrates at 3 mA cm^{-2}. E$_{WE}$ refers to the potential of the working electrode. Ag showed the lowest potential barrier (~4 mV), and carbon showed the highest potential barrier (~30 mV) for Zn deposition. The insets show the schematic mechanisms of Zn nucleation on Ag and C, which explain the extra energy involved in Zn nucleation on C. Due to the solid solution buffer layer of Ag dissolved in Zn, the nucleation energy was reduced. c, Calculated Gibbs free energy of formation at room temperature of Zn, ζ- and ε-Zn$_x$Ag$_{1-x}$ alloy phases and the corresponding electrochemical potential shift of Zn^{2+}/Zn$_x$Ag$_{1-x}$ compared with that of Zn^{2+}/Zn.
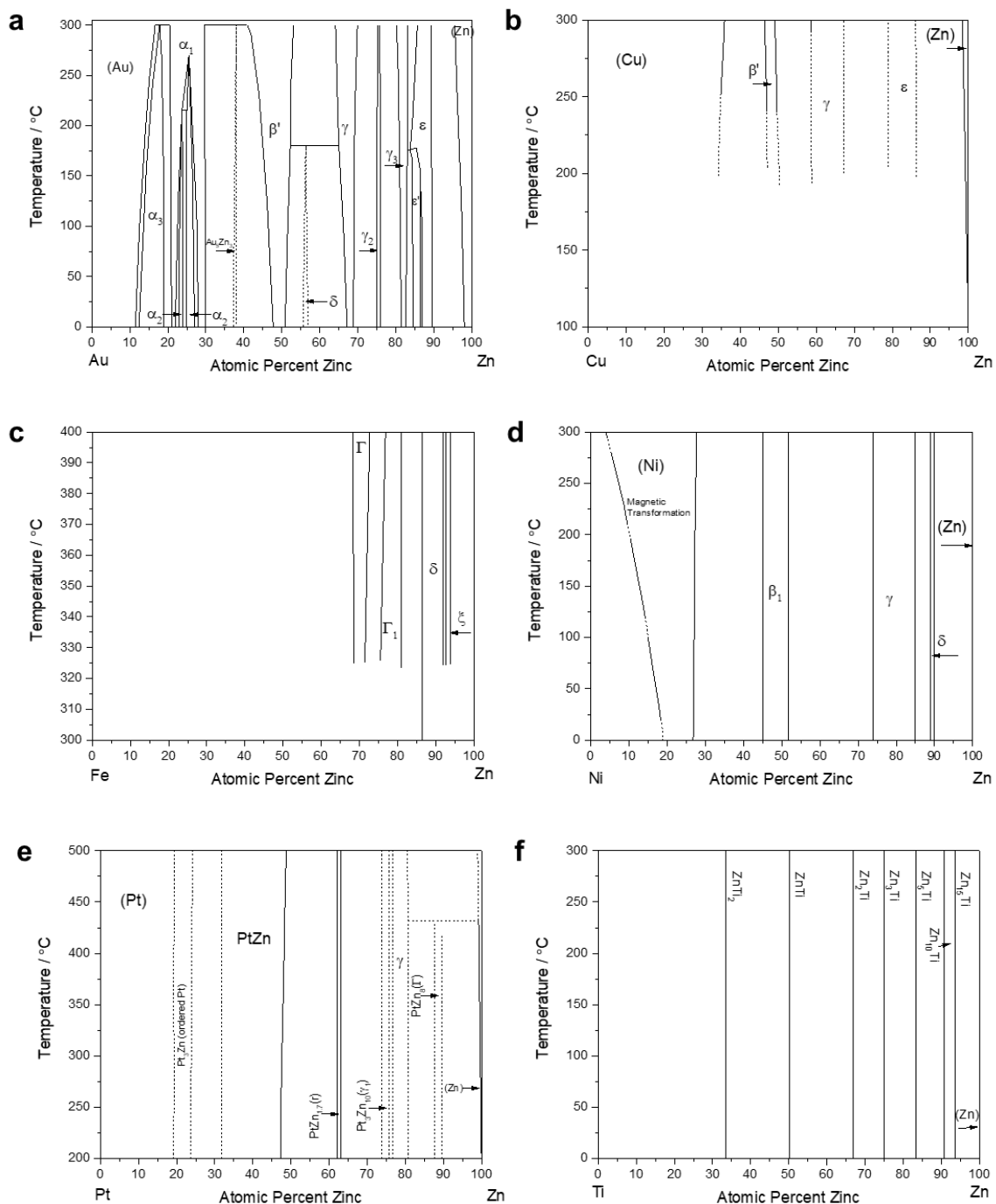
Figure 3.2 - Phase diagrams of selected materials with Zn, including Au (a), Cu (b), Fe (c), Ni (d), Pt (e) and Ti (f).

Figure 3.1b shows the voltage profiles of Zn metal deposition onto various substrates (Ag, Au, Cu, Ti, carbon). The Zn metal nucleation barrier is defined as the difference between the initial voltage dip and the later part of the voltage plateau, which is

related to the miscibility of these materials with Zn[164]. Some materials have definite solubilities in Zn according to the phase diagrams, including Ag (~0.5 at.% at 100°C), Au (~2 at.% at 0°C), and Cu (~0.1 at.% at 100°C). The solubility of Ti in Zn is negligible. Although the solubility of Ag and Cu in Zn at room temperature are not directly available from the phase diagrams, it is reasonable to extrapolate that there will still be some solubility at room temperature. A high potential barrier (~30 mV) is observed on carbon, which is due to the heterogeneous nucleation barrier (Figure 3.1b, bottom inset). Ti with slight solubility in Zn shows a relatively low potential barrier of 12 mV. Metals including Ag, Cu, and Au exhibit low potential barriers (4 mV for Ag, 7 mV for Cu, and 8 mV for Au) for Zn deposition, which can be attributed to their higher solubilities in Zn. Take Ag as an example, the dissolution of surface Ag into Zn forms a solid-solution surface layer (Figure 3.1b, top inset), which has an identical crystal structure to that of pure Zn metal (hcp) and thus can serve as a buffer layer and eliminate nucleation barriers for subsequent Zn deposition. Pt, Ni and Fe have drastically different voltage profiles from above metals, due to their high activities towards hydrogen evolution reaction in alkaline electrolytes[177]. Even though Pt, Ni and Fe can form alloy phases with Zn or are soluble in Zn according to the phase diagrams, no Zn is plated on them as evidenced by their lack of Zn stripping capacity (Figure 3.3).
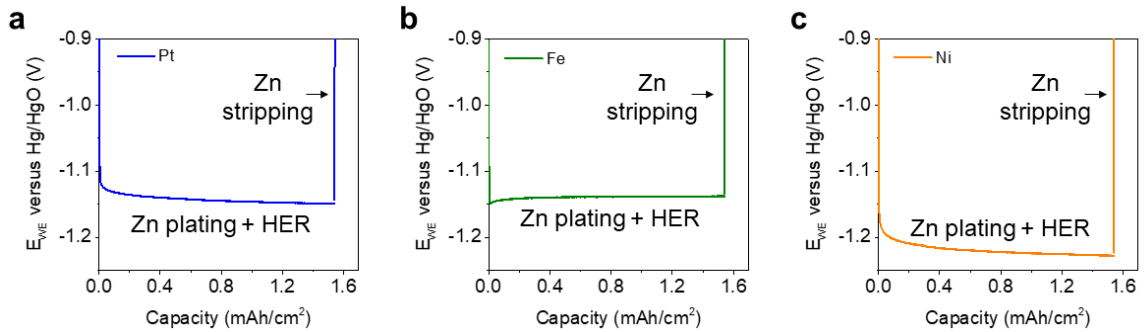
Figure 3.3 - Voltage profiles of galvanostatic Zn plating and stripping on Pt (a), Fe (b), and Ni (c) substrates at 3 mA cm^{-2}. E$_{WE}$ refers to the potential of the working electrode. Fe, Ni, and Pt exhibited high hydrogen evolution reaction (HER) activity with negligible Zn plated.

It is hypothesized that Zn-soluble materials with low nucleation barriers can regulate the deposition of Zn metal. Among the materials being tested, Ag exhibits the lowest potential barrier of Zn nucleation. Thus, it was chosen to demonstrate the concept. In addition, Ag can react with Zn to form crystalline ζ-, γ-, and ε-Zn$_x$Ag$_{1-x}$ alloy phases, as indicated by the Ag-Zn phase diagram. A computerized calculation of phase diagrams (CALPHAD) technique[175] was used to obtain the Gibbs free energy of formations (Figure 3.1c) at room temperature of Zn, ζ- and ε-Zn$_x$Ag$_{1-x}$ alloy phases observed in the experiments. The corresponding electrochemical potential shift of Zn^{2+}/Zn$_x$Ag$_{1-x}$ compared with that of Zn^{2+}/Zn was also computed. All of the Zn$_x$Ag$_{1-x}$ alloy phases possess a negative Gibbs free energy of formation, which means that the formation of Zn$_x$Ag$_{1-x}$ is spontaneous during Zn plating. As a result, Ag can potentially be used as a seed to (1) nucleate Zn with a low potential barrier, and (2) accommodate Zn by forming alloy phases.

3.3.2   *Spatially controlled and uniform Zn deposition*

To evaluate the possibility of Ag as a seed to spatially control the Zn electrodeposition (Figure 3.4a), Ag islands were patterned as the seeding material on the C

substrate (Figure 3.5), onto which Zn was galvanostatically deposited at 2.4 mA cm^{-2}. As shown in the operando optical microscopy images (Figure 3.4b), most of the Zn was preferentially deposited onto the Ag patterns. A set of operando images with high magnification is shown in Figure 3.6. EDS mapping (Figure 3.4c) of the electrode after the Zn deposition process further confirmed the spatially controlled Zn deposition.
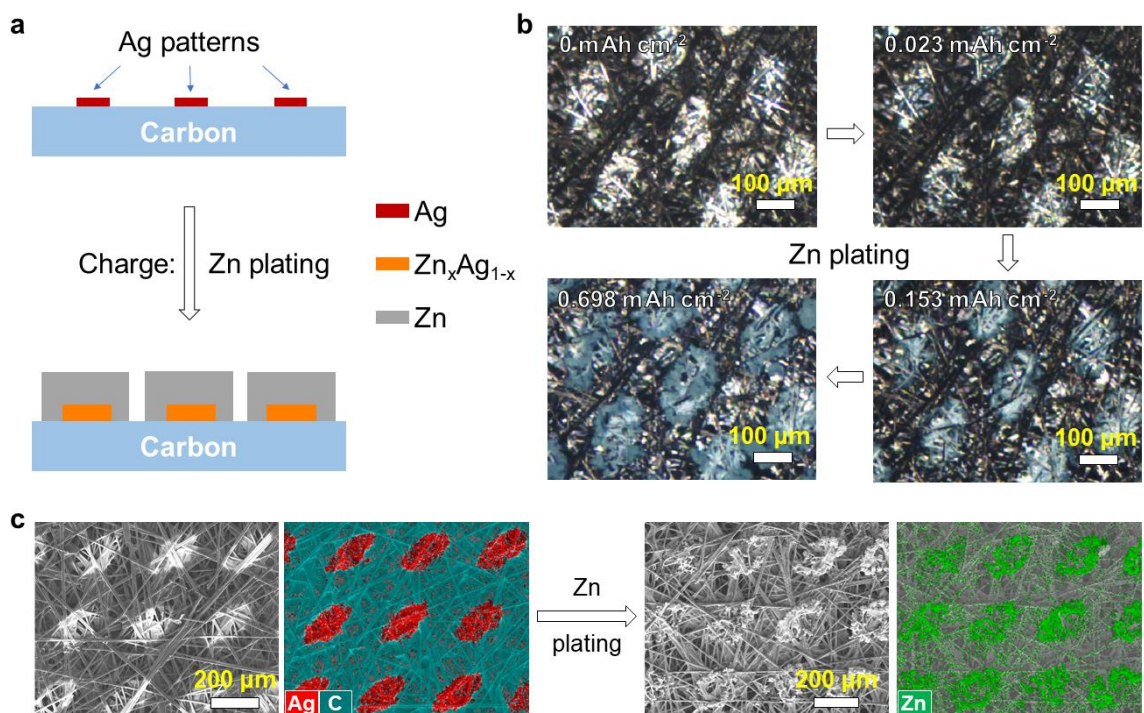
Figure 3.4 - Spatial control of Zn deposition using Ag nuclei. a, Schematic of the spatially controlled Zn plating on the Ag islands patterned on carbon paper. b, Operando optical microscopy of the Zn plating (2.4 mA cm^{-2}) on the Ag islands patterned on carbon paper. c, SEM images and elemental mapping images of the carbon paper coated with patterned Ag islands before and after Zn plating. A spatially controlled deposition of Zn was achieved due to the preferential Zn deposition on Ag.
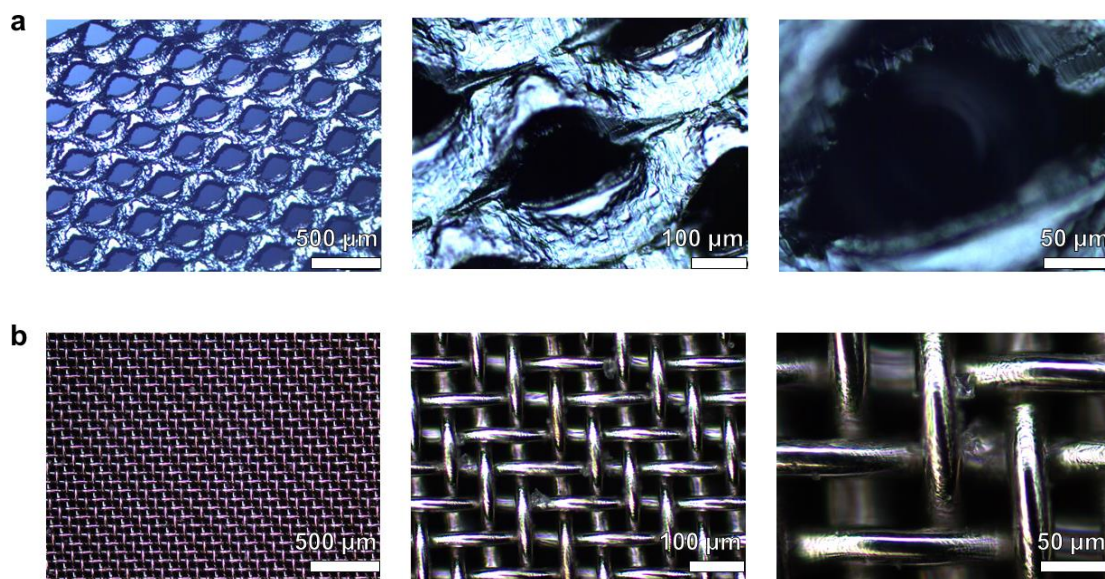
Figure 3.5 - Optical microscopy images of stainless steel meshes purchased from Dexmet (a) and TWP (b). These meshes were used as masks during Ag evaporation, to pattern Ag on various substrates.
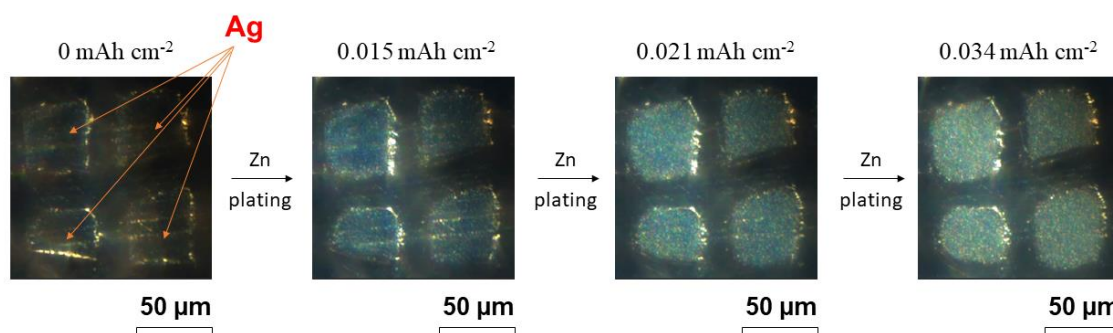
Figure 3.6 - Operando optical microscopy analysis of Zn plating (1 mA cm^{-2}) on the Ag patterned C substrate. The square area is coated with Ag. Most of Zn was preferentially deposited onto Ag patterns. The transitions (Ag-Zn$_x$Ag$_{1-x}$-Zn) can be observed.

Nonuniform and dendritic metal deposition is a well-known problem for Zn anodes (Figure 3.7a). By spatially controlling and accommodating Zn deposition, a uniform Zn plating is expected to be achieved (Figure 3.7b). To demonstrate this, Ag nanoparticles were firstly loaded onto the inert carbon-fiber paper substrate (C-Ag, Figure 3.8, Figure

3.9). Ag nanoparticles and polyvinylidene difluoride (PVDF) binder were mixed in *N*-methylpyrrolidone, and the resultant slurry was drop cast onto carbon paper substrates. The diameter of the Ag nanoparticles, which exhibited a face-centered cubic (FCC) structure, was less than 50 nm (Figure 3.10, Figure 3.11). The carbon paper and C-Ag electrodes were then galvanostatically cycled in ZnO-saturated 4 M KOH electrolyte and monitored the electrodes in operando using an optical microscope. As shown in Figure 3.7c, mossy and dendritic Zn deposits could be observed on the bare carbon paper during charging at the 2nd cycle. In addition, dead Zn that remained from the 1st cycle was observed on the carbon paper at the beginning of the 2nd charge, and grew in charging, which meant that the dead Zn reconnected to the carbon paper and served as the core for further Zn deposition. The break and reconnection of dead Zn could lead to the instability of Zn anodes (fluctuation of capacity) during battery cycling. In contrast, the Zn deposited onto the C-Ag electrode was uniform, and no dead Zn was observed in the fully discharged state (Figure 3.7d).
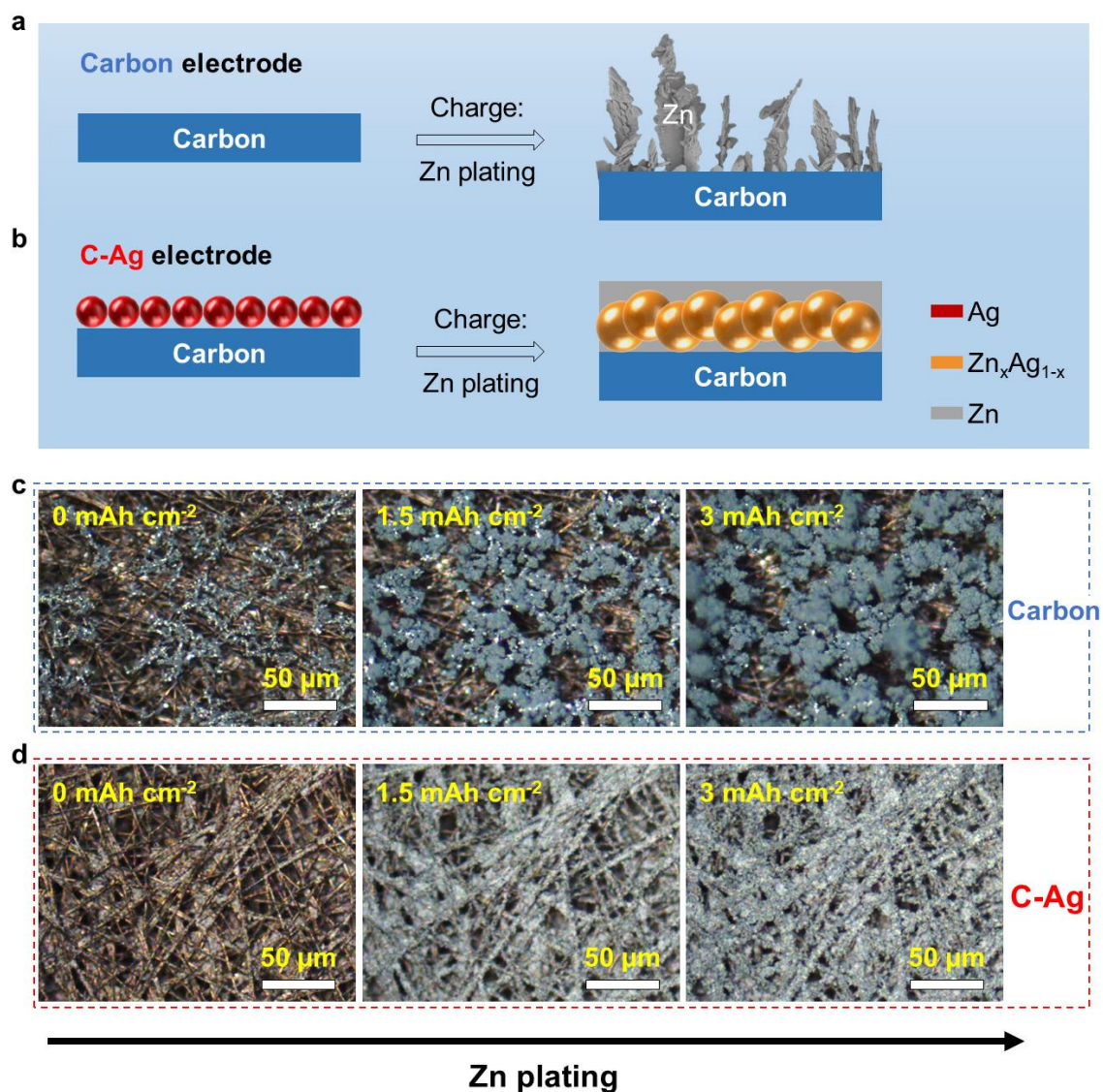
Figure 3.7 - Morphology control of Zn deposition using Ag nuclei. a, Schematic of nonuniform and dendritic Zn deposition on the carbon paper substrate, which has no solubility in Zn. **b,** Schematic of uniform Zn deposition on the carbon paper slurry-coated with Ag nanoparticles. Ag nanoparticles serve as the nucleation sites for the Zn_xAg_{1-x} alloy formation and Zn deposition. **c,d,** Operando optical microscopy analysis of Zn plating (18 mA cm^{-2}) on the carbon (c) and C-Ag (d) electrodes. Zn plating on the carbon electrode is mossy, while it is uniform on the C-Ag electrode.
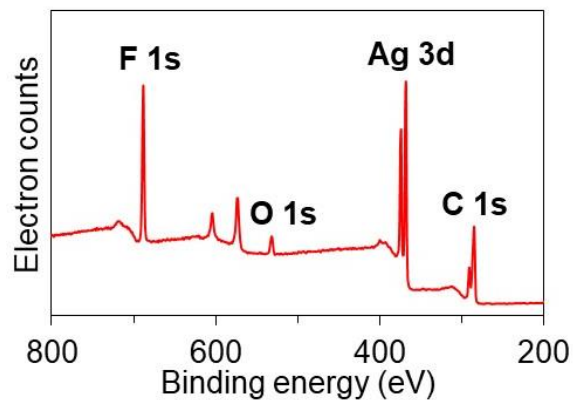
Figure 3.8 - XPS survey spectra of the C-Ag electrode.
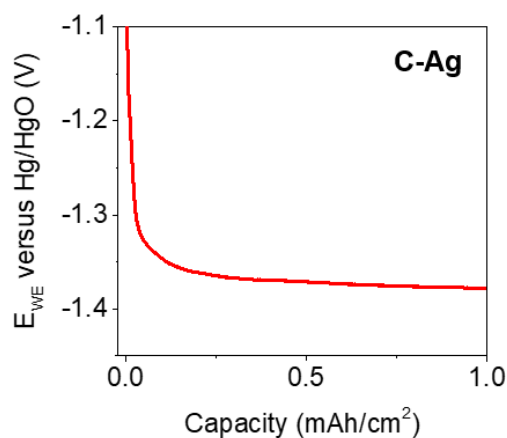
Figure 3.9 - Voltage profile of galvanostatic Zn deposition on C-Ag at 3 mA cm⁻². No potential barrier was observed at the onset of Zn deposition, which indicates that the loading of Ag nanoparticles eliminates the nucleation barrier.
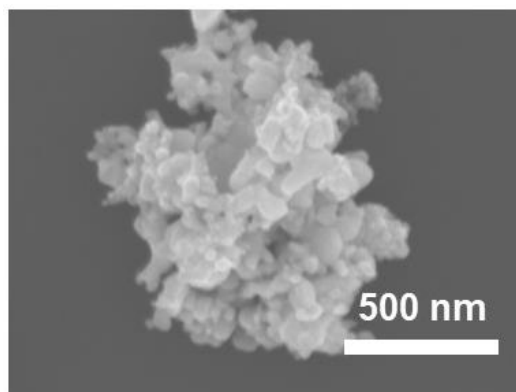
Figure 3.10 - SEM image of Ag nanoparticles.
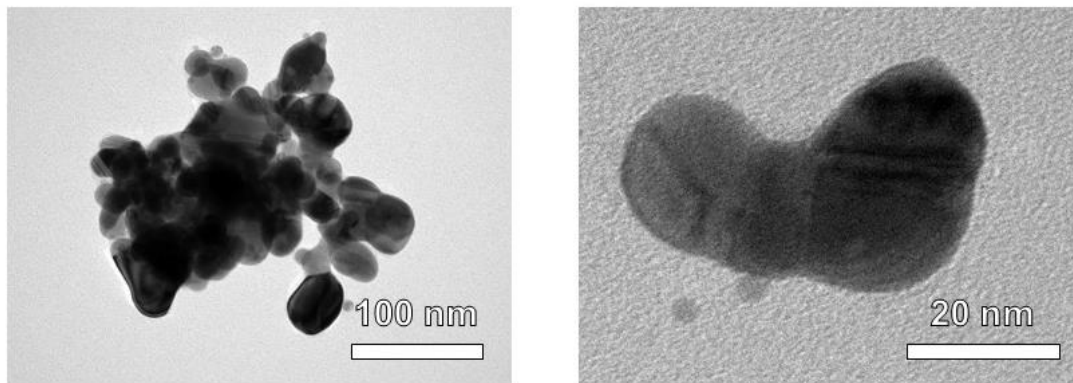
Figure 3.11 - TEM images of Ag nanoparticles.

3.3.3   Mechanism of Zn plating/stripping in the presence of alloying seeds

The C-Ag electrode was assembled into a full Ni-Zn battery using $Ni(OH)_2$ as the cathode and ZnO-saturated 4 M KOH as the electrolyte. The charge capacities were controlled to be 497, 994 and 1,491 mAh g_{Ag}^{-1}, so that the molar ratios of deposited Zn to Ag (Zn:Ag) are 1, 2 and 3 assuming no side reaction. In the rest of this article, "Zn:Ag=1", "Zn:Ag=2" and "Zn:Ag=3" were used to represent charging conditions. The actual Zn:Ag are approximately 0.7, 1.7 and 2.8, respectively, when Coulombic inefficiency is considered. To characterize crystalline Zn_xAg_{1-x} alloys under different charging conditions, ex situ X-ray diffraction (XRD) was performed for the C-Ag electrode and observed that Zn_xAg_{1-x} alloy phases (ε-, ζ-) were formed successfully (see Figure 3.12, Table 3.1 for detailed description of alloy phases and compositions). When Zn:Ag increased from 1 to 3, the Ag peak intensity decreased while the Zn and hexagonal ε-Zn_xAg_{1-x} peak intensities increased, because Ag turns into alloys with Zn. The cubic ζ- Zn_xAg_{1-x} alloy phase diminished when the Zn:Ag ratio was increased from 1 to 2, which was due to the further zincation of ζ- Zn_xAg_{1-x} to ε-Zn_xAg_{1-x}. In addition, the positive shift of the characteristic peak positions of the ε-Zn_xAg_{1-x} phase also indicated the formation of Zn-richer alloys at

107

high Zn:Ag ratios. For ζ-Zn_xAg_{1-x} (0.342<x<0.513), $Zn_{0.5}Ag_{0.5}$ was detected. For ε-Zn_xAg_{1-x} (0.679<x<0.873), $Zn_{0.695}Ag_{0.305}$, $Zn_{0.74}Ag_{0.26}$, $Zn_{0.75}Ag_{0.25}$, $Zn_{0.78}Ag_{0.22}$, and $Zn_{0.84}Ag_{0.16}$ were detected. Additional ζ- and ε-alloy phases with different x values may also exist, but they cannot be identified by XRD due to their absence in the Powder Diffraction File database. The XRD results shown above confirm the formation of alloy phases and reveal alloy compositions on the C-Ag electrode under different Zn deposition conditions. The formation of Zn_xAg_{1-x} alloys was also confirmed by energy-dispersive X-ray spectroscopy (EDS) mappings (Figure 3.13, Figure 3.14).
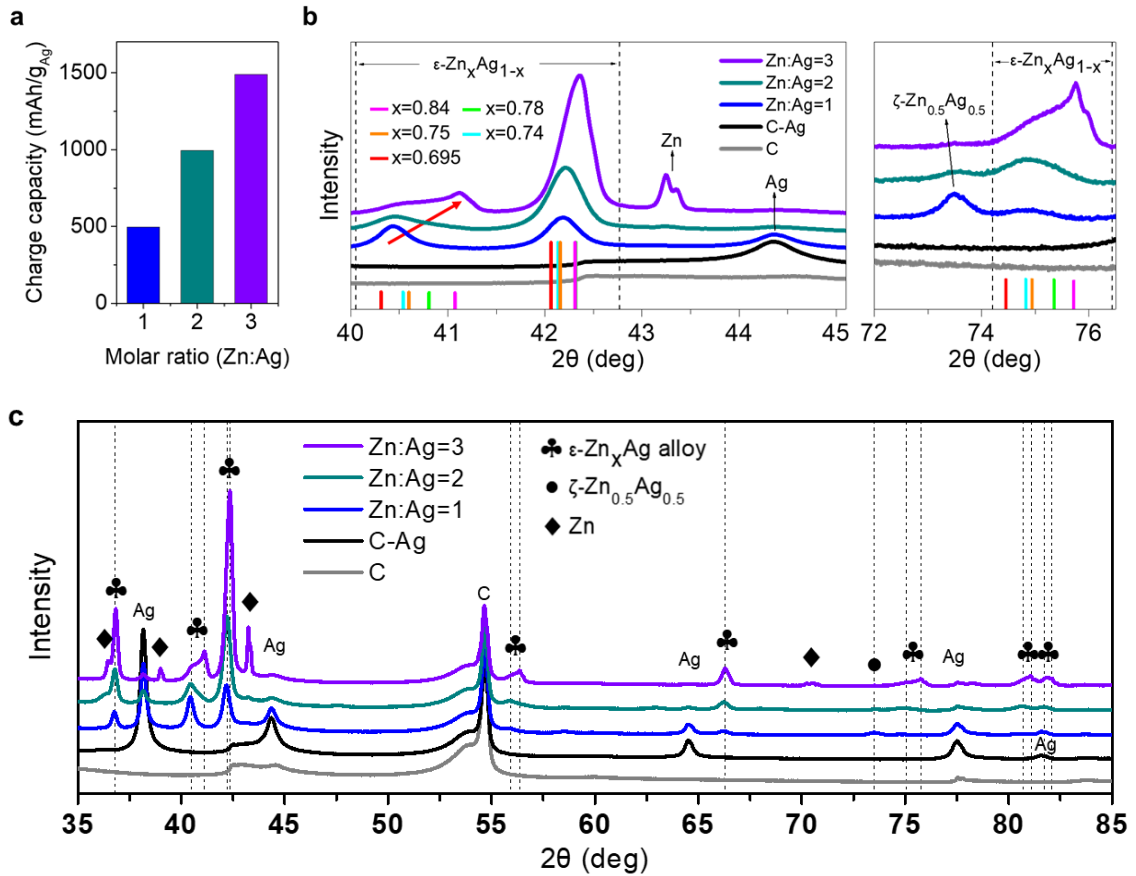
Figure 3.12 - Characterization of products from electrochemical deposition of Zn on Ag. a, Corresponding charge capacities at different molar ratios of plated Zn to Ag ranging from 1 to 3 on the C-Ag electrode. b,c, Zoom (b) of XRD patterns (c) of the C-Ag electrode at different molar ratios of plated Zn to Ag ranging from 1 to 3.

Characteristic peaks of the $Zn_{0.695}Ag_{0.305}$, $Zn_{0.74}Ag_{0.26}$, $Zn_{0.75}Ag_{0.25}$, $Zn_{0.78}Ag_{0.22}$, and $Zn_{0.84}Ag_{0.16}$ hexagonal alloy phases are labeled.

Table 3.1 - Calculated Gibbs free energy of formations at room temperature of Zn and multiple Zn_xAg_{1-x} alloy phases and corresponding electrochemical potential shifts of Zn^{2+}/Zn_xAg_{1-x} compared with that of Zn^{2+}/Zn, including ζ-$Zn_{0.5}Ag_{0.5}$, ε-$Zn_{0.695}Ag_{0.305}$, ε-$Zn_{0.74}Ag_{0.26}$, ε-$Zn_{0.75}Ag_{0.25}$, ε-$Zn_{0.78}Ag_{0.22}$ and ε-$Zn_{0.84}Ag_{0.16}$.

Zn_xAg_{1-x}	Gibbs free energy of formation (kJ/mol$_{Zn}$)	Electrochemical potential shift (V)
ζ-$Zn_{0.5}Ag_{0.5}$	-39.34	+0.20
ε-$Zn_{0.695}Ag_{0.305}$	-27.72	+0.14
ε-$Zn_{0.74}Ag_{0.26}$	-25.24	+0.13
ε-$Zn_{0.75}Ag_{0.25}$	-24.73	+0.13
ε-$Zn_{0.78}Ag_{0.22}$	-23.19	+0.12
ε-$Zn_{0.84}Ag_{0.16}$	-20.12	+0.10
Zn	0	0
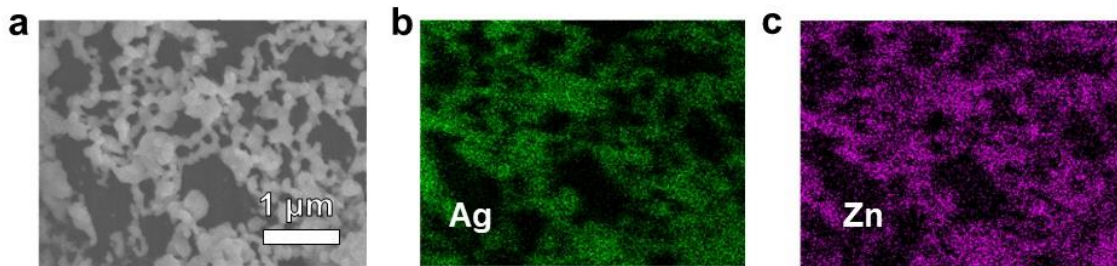
Figure 3.13 - SEM image (a) and elemental mappings (b, c) of the C-Ag electrode after Zn deposition.
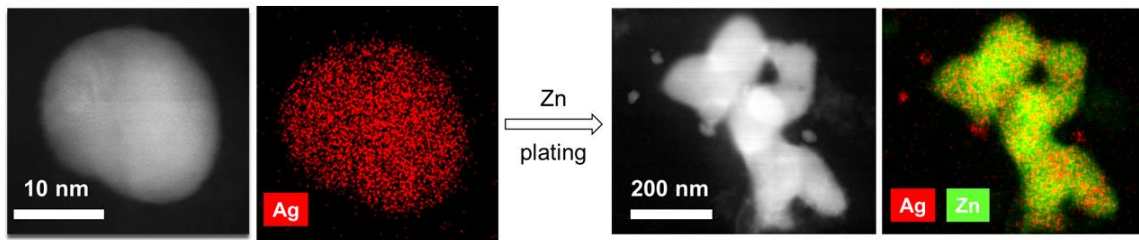
Figure 3.14 - STEM images and elemental mapping images of Ag nanoparticles before and after Zn deposition. The $Zn_{2.2}Ag$ alloy was identified after Zn plating.

Upon galvanostatic cycling, the voltage profile (Figure 3.15a) showed one charge plateau and two apparent discharge plateaus (1.8-1.6 V and 1.6-1.4 V). To probe the phase transitions of the C-Ag electrode during cycling at Zn:Ag=3, ex situ XRD analysis (Figure 3.15b) of the C-Ag anode was conducted at 5 different charge/discharge states, as noted in Figure 3.15a. In charged states (1) and (2), the Zn and Zn_xAg_{1-x} alloy phases coexist. During charging from (1) to (2), the peak intensities of Zn increased while the Zn_xAg_{1-x} alloy peaks remained almost unchanged. This result indicates that alloy phases formed prior to the formation of the Zn phase, which is reasonable because alloy phases possess a negative Gibbs free energy of formation. It is counterintuitive that only one charge plateau exists while both Zn and Zn_xAg_{1-x} form. It is speculated that the alloy formation rate may be kinetically slower than the Zn deposition rate, which results in only one charge plateau attributed to the Zn^{2+}/Zn redox. Afterward, the Zn and Ag atoms may diffuse slowly to spontaneously form the Zn_xAg_{1-x} alloy. When discharged to state (3), the end of the first discharge plateau, the Zn peak intensity in the corresponding XRD pattern dramatically decreased, while the Zn_xAg_{1-x} alloy peak intensities remained almost unchanged. This result implies that the first discharge plateau (1.8-1.6 V) is mainly attributable to Zn stripping from Zn metal. Upon further discharging, the Zn_xAg_{1-x} alloy peaks decreased at state (4) and their intensities clearly decreased when the battery reached the fully discharged state (5). It is concluded that the second discharge plateau (1.6-1.4 V) was associated mainly with Zn stripping from the Zn_xAg_{1-x} alloys, which is consistent with CALPHAD results that the Zn^{2+}/Zn_xAg_{1-x} redox had a higher potential than Zn^{2+}/Zn. In addition, alloy phases became Zn-leaner during discharging, as evidenced by the negative shift in the characteristic peak positions of the $\varepsilon\text{-}Zn_xAg_{1-x}$ phase, which also matched

CALPHAD results indicating that Zn-lean alloy phases possessed larger electrochemical potential. It was observed that the Ag nanoparticles could not recover to their original crystal structure after cycling, as evidenced by the unrecovered Ag peaks and the existence of Zn-lean Zn_xAg_{1-x} alloy phases in the fully discharged state (5). The remaining Ag peaks in both the charged and discharged states belong to unreacted Ag nanoparticles, which might be encapsulated by PVDF and thus inactive.
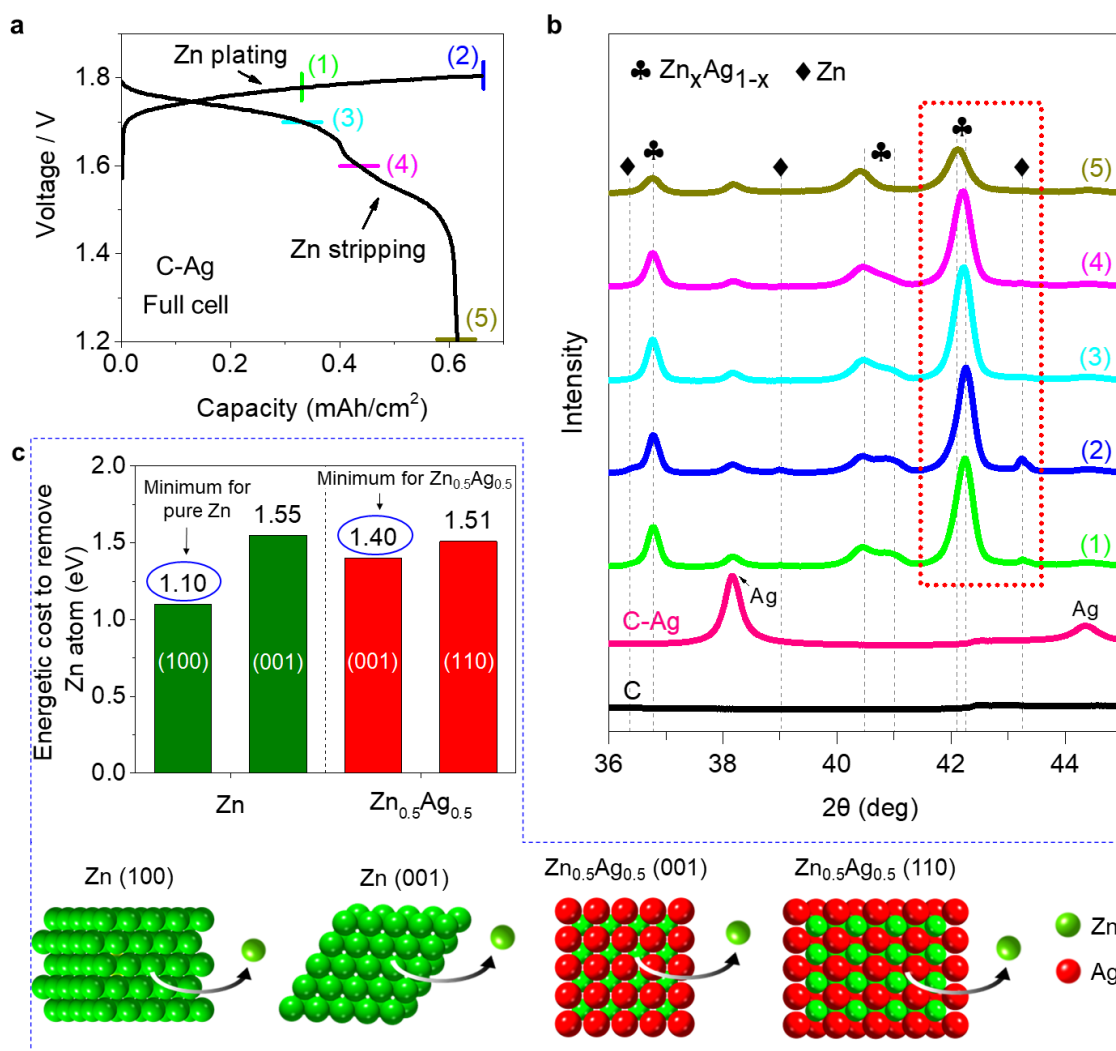
Figure 3.15 - Shift of the stripping potential due to the presence of alloy. a, Voltage profiles of a full cell containing a C-Ag anode, Ni(OH)₂ cathode, and ZnO-saturated 4 M KOH electrolyte. b, XRD results of the C-Ag electrode at different

charge/discharge states, as labeled in (a). The first (1.8-1.6 V) and the second (1.6-1.4 V) discharge plateaus correspond to Zn stripping from the pure Zn metal and the Zn_xAg_{1-x} alloys, respectively (see the red-dashed frame for the reader's convenience). c, DFT simulation results showing the energetic cost of removing a Zn atom from the pure Zn metal and $Zn_{0.5}Ag_{0.5}$ alloy. Constructed models: Zn with 001 and 100 surfaces; $Zn_{0.5}Ag_{0.5}$ with 110 and 001 surfaces.

To further understand the Zn stripping process at the atomic level, models of pure Zn metal and $Zn_{0.5}Ag_{0.5}$ alloy crystals were simulated *in silico* and investigated the relative energetic cost of Zn removal from various termination environments using density functional theory (DFT)[170–174]. The $Zn_{0.5}Ag_{0.5}$ alloy phase was chosen for the DFT study because it was the phase detected during experiments; furthermore, its crystal structure is relatively simple. Nanoparticles under cyclic dissolution and reformation in a battery environment display a range of morphologies and surface environments. Therefore, two surfaces for each material (Zn metal and $Zn_{0.5}Ag_{0.5}$ alloy) were selected to represent a low-coordination-number environment (100 and 001 surfaces for Zn and $Zn_{0.5}Ag_{0.5}$, respectively) and a high-coordination-number environment (001 and 110 surfaces for Zn and $Zn_{0.5}Ag_{0.5}$, respectively) (Figure 3.16). Multiple possibilities for Zn removal for each slab model were considered to probe the various thermodynamic states in cases of chemically unique Zn atoms. A full report of all of data is available in Table 3.2. For the 001 surface termination of $Zn_{0.5}Ag_{0.5}$, both the Zn-terminated and Ag-terminated surfaces were studied, although the Ag-terminated surface was found to be much more energetically stable and thus was the one being considered in the data. The minimum energy to remove Zn from each material/termination environment was reported in Figure 3.15c. The minimum energy to remove Zn was 1.10 eV for Zn with a 100 surface termination and 1.40 eV for $Zn_{0.5}Ag_{0.5}$ with a 001 surface termination, which indicates the Zn atom is less reactive in the $Zn_{0.5}Ag_{0.5}$ alloy than in the pure Zn metal. These DFT results provide some

insight into the more energetic Zn stripping process from Zn_xAg_{1-x} alloys and thus higher

electrochemical potential of the Zn^{2+}/Zn_xAg_{1-x} redox than the Zn^{2+}/Zn redox.
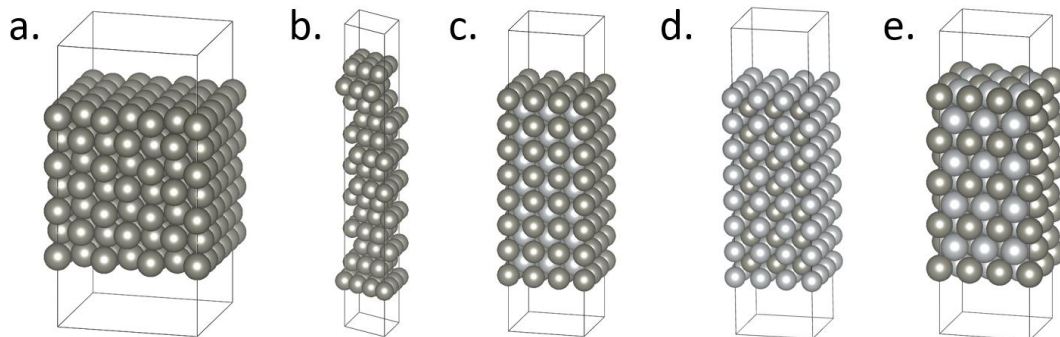
Figure 3.16 - Images of various computational slab models of Zn metal and $Zn_{0.5}Ag_{0.5}$ alloys. a. Zn metal 100 surface (low coordination) b. Zn metal 001 surface (high coordination) c. $Zn_{0.5}Ag_{0.5}$ alloy with Zn surface termination 001 surface (low coordination) d. $Zn_{0.5}Ag_{0.5}$ alloy with Ag termination 001 surface (low coordination) e. $Zn_{0.5}Ag_{0.5}$ alloy 110 surface (high coordination).

Table 3.2 - DFT simulation results showing the energetic cost to remove a Zn atom from pure Zn metal and $Zn_{0.5}Ag_{0.5}$ alloy. Models of Zn with 001 and 100 surfaces and $Zn_{0.5}Ag_{0.5}$ with 110 and 001 surfaces were constructed.

Material and terminated surface	Remove Zn from	Energetic cost (eV)
Zn 001	Surface	1.545
Zn 100	Surface	1.104
$Zn_{0.5}Ag_{0.5}$ 110	Surface	1.578
$Zn_{0.5}Ag_{0.5}$ 110	First sublayer	1.511
$Zn_{0.5}Ag_{0.5}$ 110	Second sublayer	1.528
$Zn_{0.5}Ag_{0.5}$ 110	Center	1.622
$Zn_{0.5}Ag_{0.5}$ 001 Zn terminated	Surface	0.646[*]
$Zn_{0.5}Ag_{0.5}$ 001 Ag terminated	Sublayer	1.667
$Zn_{0.5}Ag_{0.5}$ 001 Ag terminated	Core	1.403

* For the 001 surface termination of $Zn_{0.5}Ag_{0.5}$, both the Zn-terminated and Ag-terminated

surfaces were studied, although the Ag-terminated surface was found to be much more

energetically stable and thus is the one being considered in the data. In addition, even though Zn-terminated surface exists, it will further change to Ag-terminated once surface Zn is removed, which still cost more energy to further remove Zn.

To confirm that the two discharge plateaus of the full battery were caused by the C-Ag anode instead of the $Ni(OH)_2$ cathode, the voltage profile of a full Ni-Zn battery using the carbon paper as the anode is presented in Figure 3.17. Only one discharge plateau was observed when Ag was not added to the anode. Cyclic voltammetry (CV) of the C-Ag electrode was also carried out using a three-electrode electrochemical cell that consisted of the substrate of interest as the working electrode, Hg/HgO as the reference electrode, Zn foil as the counter electrode and a ZnO-saturated 4 M KOH aqueous solution as the electrolyte. The result was in good agreement with the analysis that the two discharge plateaus were due to the different electrochemical potentials of the Zn^{2+}/Zn and Zn^{2+}/Zn_xAg_{1-x} redox reactions on the C-Ag electrode (Figure 3.18).
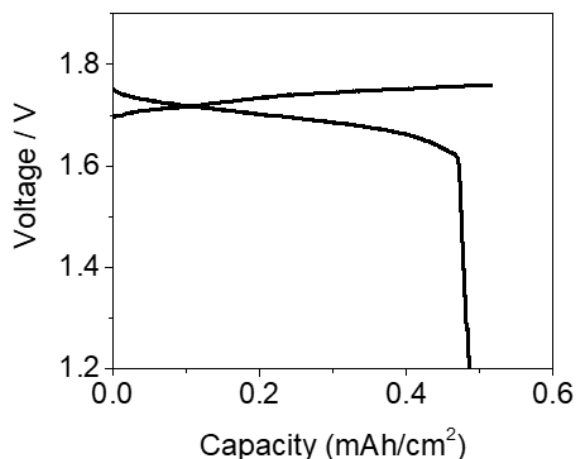
Figure 3.17 - Charge and discharge curves of a Zn-Ni full cell with C anode, $Ni(OH)_2$ cathode, and ZnO-saturated 4M KOH electrolyte.
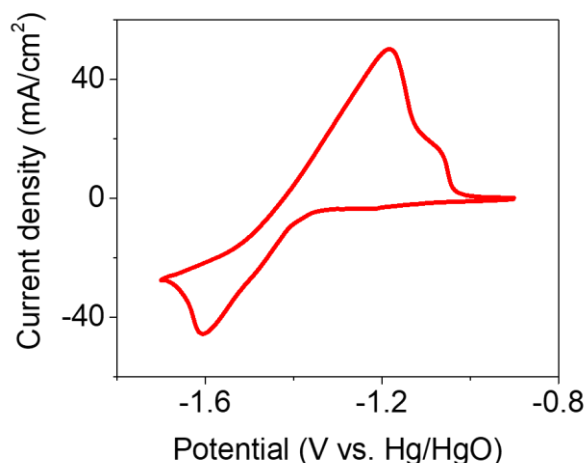
Figure 3.18 - Cyclic voltammogram of the C-Ag electrode at 10 mV s^{-1} scan rate in ZnO saturated 4M KOH electrolyte.

3.3.4   Stable cycling of Ag-seeded Zn anodes

In previous sections, the spatially controlled and uniform Zn deposition on the Ag seeds was demonstrated and investigated. To further evaluate the cyclic stability of Ag-seeded Zn anodes (C-Ag), pouch-type Ni-Zn batteries were assembled and tested. Batteries with bare C anodes were also assembled and tested under the same conditions. During charging, zincates dissolved in the electrolyte were electrochemically reduced at the anode. Less than 7.5% of zincates from the electrolyte were consumed in each cycle, to minimize the hydrogen evolution side reaction.

As shown in the cycling results (Figure 3.19a, Figure 3.20, Figure 3.21, Figure 3.22), instead of steady capacity decay, batteries undergo irregular capacity decay with intensified fluctuations of capacity over cycling, which is indicative of battery degradation. To better analyze the cyclic stabilities of the C-Ag and C electrodes, a box-and-whisker plot was constructed to show the statistic distributions of their discharge capacities over cycling (Figure 3.19b), where a summary of five numbers is displayed, including the

"minimum", first quartile, median, third quartile, and "maximum" discharge capacities. At all Zn:Ag ratios (1, 2, and 3), the C-Ag electrodes demonstrated higher cyclic stability with less fluctuation of capacity than the C electrodes. In addition, the C-Ag electrodes also achieved a higher average discharge capacity and Coulombic efficiency than the C electrodes: 491.7 mAh g^{-1} and 99.0% for C-Ag vs. 487.3 mAh g^{-1} and 98.1% for C at Zn:Ag=1; 983.7 mAh g^{-1} and 99.1% for C-Ag vs. 893.1 mAh g^{-1} and 97.3% for C at Zn:Ag=2; 1,458.9 mAh g^{-1} and 98.0% for C-Ag vs. 1,175.4 mAh g^{-1} and 96.7% for C at Zn:Ag=3. The above statistical analysis was done within limited cycle ranges for C-Ag and C electrodes: 14,980 cycles for Zn:Ag=1, 1,480 cycles for Zn:Ag=2, and 630 cycles for Zn:Ag=3. Due to the irregular capacity decay, the cycle life was defined as the cycle number when the relative standard deviation of discharge capacities exceeds 1%. As shown in Figure 3.19c, the C-Ag electrodes exhibited superior cycle lives of 75,187, 2,501, and 752 cycles when cycled at Zn:Ag ratios ranging from 1 to 3, respectively, while the C electrodes exhibited 273, 33, and 38 cycles, respectively. The dendritic Zn plating and break/reconnection of partial dead Zn could have led to the capacity fluctuation of C electrodes, which was visualized under the optical microscope. In addition, the resultant unstable electrode–electrolyte interface and severe electrolyte decomposition (reacting with dead Zn and evolving H$_2$) might explain for the capacity decay of C electrodes. With a simple Ag nanoparticle loading process, a spatially controlled and uniform Zn deposition through heterogeneous seeded growth is achieved, leading to the superior long-term cyclic stability of the C-Ag electrodes.
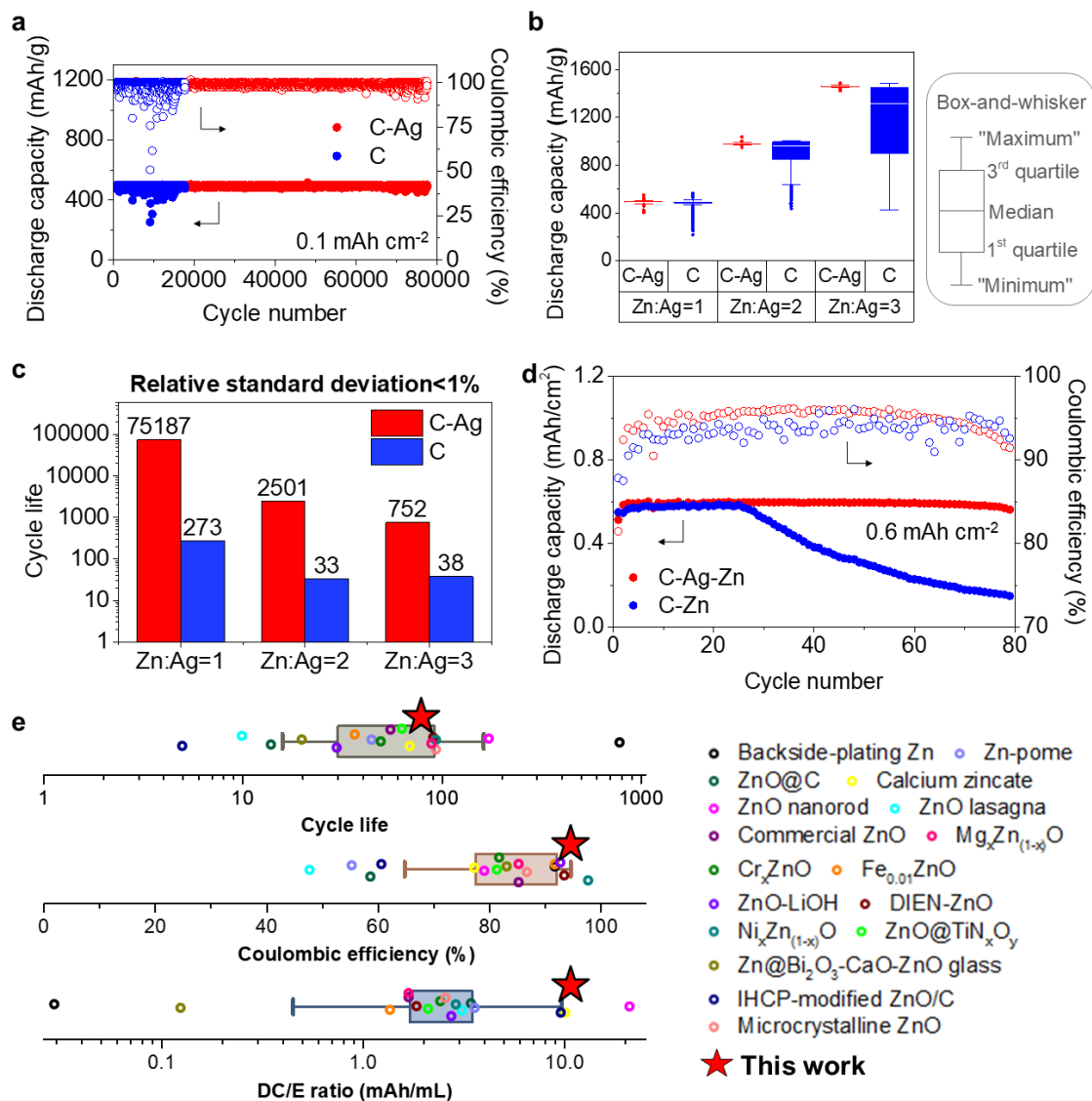
Figure 3.19 - Electrochemical performance of anodes. a, Cycling performance of the C-Ag and C electrodes at Zn:Ag=1. **b,** Box-and-whisker plot showing distributions of discharge capacities of the C-Ag and C electrodes at Zn:Ag molar ratios ranging from 1 to 3. For Zn:Ag=1, discharge capacities from the 1st cycle to the 14,980th cycle were used in the box-and-whisker plot. Similarly, the 1st cycle to the 1,480th cycle for Zn:Ag=2 and the 1st cycle to the 630th cycle for Zn:Ag=3 were used. A summary of five numbers is displayed, including the "minimum" (Q1-1.5*IQR), first quartile (Q1), median, third quartile (Q3), and "maximum" (Q3+1.5*IQR). Interquartile range (IQR): 1st to the 3rd quartile. Outliers (values that are located outside the whiskers of the box plot) are marked as red circles. **c,** Cycle life comparison of the C-Ag and C electrodes with relative standard deviations of the discharge capacities over cycling being less than 1%. This result shows that the electrochemical cycling of the C-Ag electrode is more stable than that of the C electrode. **d,** Cycling performance of the C-Ag-Zn and C-Zn anodes. **e,** Box-and-whisker plot showing a comparison

between the C-Ag-Zn anode and previously published works in terms of cycle life, Coulombic efficiency, and DC/E ratio.
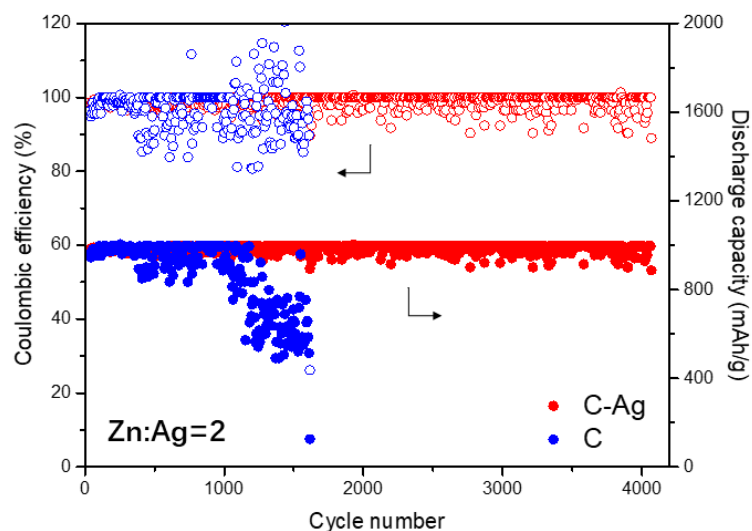
Figure 3.20 - Cycling performance of the C-Ag and C electrodes at Zn:Ag=2.
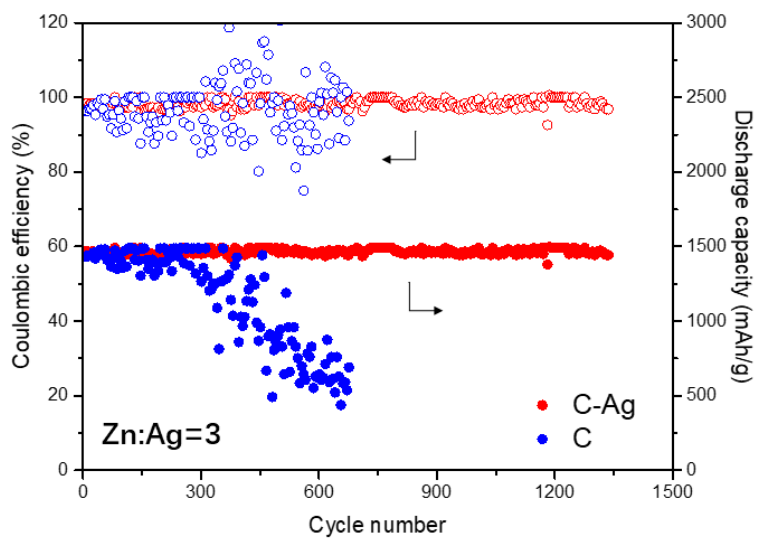
Figure 3.21 - Cycling performance of the C-Ag and C electrodes at Zn:Ag=3.
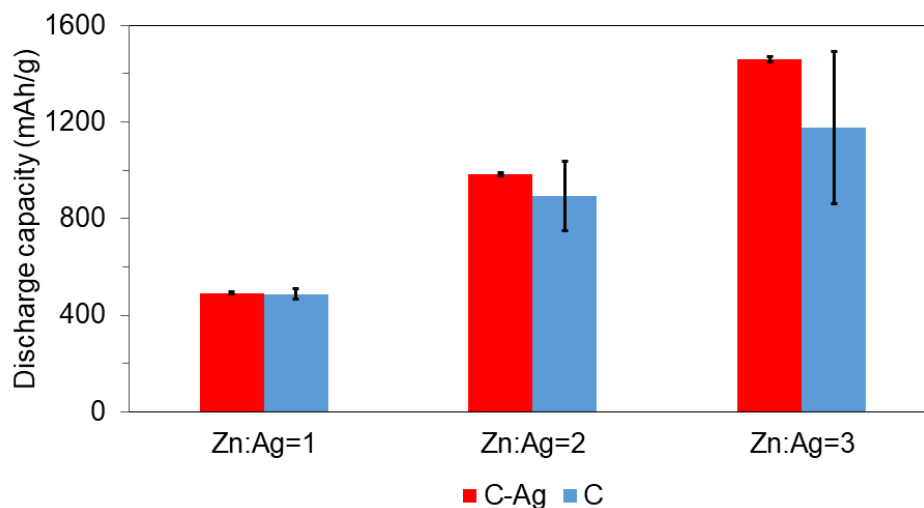
Figure 3.22 - Average discharge capacities over cycling with standard deviation bars of C-Ag and C electrodes at Zn:Ag ranging from 1 to 3.

The discharge capacity/electrolyte (DC/E) ratio is an important indicator for device-level energy density[148,149,178]. The DC/E ratio of the cells shown in Figure 3.19a-c was lower than 0.8 mAh mL^{-1} because they utilized a small percentage of the zincates available from the electrolyte. To demonstrate the effect of Ag seeds on Zn anodes at a higher DC/E ratio, ~1 mAh cm^{-2} Zn was pre-deposited onto the C and C-Ag electrodes and assembled Ni-Zn full cells. As shown in Figure 3.19d, the C-Ag-Zn anode achieved superior cycling performance, with a Coulombic efficiency of 95% for 78 cycles; the C-Zn anode performed with a Coulombic efficiency of 92.6% for 25 cycles, which implied that the Ag addition also improved the Zn anode even at a high DC/E ratio (12 mAh mL^{-1}). The simple loading of Ag nanoparticles onto the Zn anode, without any complex structural or molecular design, improved its cycling performance to be comprehensively superior to that of previously reported, deeply cycled Zn anodes with 100% depth-of-discharge in alkaline electrolytes (Figure 3.19e). Three parameters (cycle life, Coulombic efficiency, and DC/E ratio) were considered in the comparison (Table 3.3). Notably, it was

less meaningful to compare only one or two parameters; thus, only publications that reported all three values or provided necessary information to calculate them were included in the comparison. Partially discharged metallic zinc anodes were not included for comparison either, because their discharge capacity (and therefore Coulombic efficiency) is artificially controlled and cannot reflect the intrinsic property of the anodes.

Table 3.3 - Comparison of the C-Ag-Zn anode with previously reported zinc-based anodes in aspects of cycle life (with >80% retained capacity), Coulombic efficiency, and discharge capacity/electrolyte (DC/E) ratio in alkaline electrolytes. It is less meaningful to compare only one or two terms, thus, only works that reported these values or provided necessary information for their calculations are included in the comparison. Also, partially discharged metallic zinc anodes are not included because their Coulombic efficiency can be controlled by the cycling protocol and cannot reflect the extent of side reactions happened on Zn anodes.

Anode label	Anode material	Cycle life	Coulombic efficiency (%)	DC/E ratio (mAh/mL)
●	Backside-plating zinc[179]	800	92.00	0.03
●	ZnO@C[81]	14	58.81	3.50
●	ZnO@TiN$_x$O$_y$[9]	64	81.57	2.14
●	Zn-pome[82]	45	55.47	3.65
●	ZnO lasagna[151]	10	47.87	3.15
●	ZnO nanorod[180]	175	79.31	21.54
●	Calcium zincate[153]	70	77.50	10.33
●	Zn@Bi$_2$O$_3$-CaO-ZnO glass[154]	20	83.33	0.13
●	IHCP-modified ZnO/C[155]	5	60.79	9.80
●	Commercial ZnO[156]	56	85.50	1.71
●	DIEN-ZnO[156]	92	93.70	1.87
●	Cr$_x$ZnO[157]	50	82.00	2.46
●	Ni$_x$Zn$_{(1-x)}$O[158]	95	98.00	2.94
●	Microcrystalline ZnO[159]	95	87.00	2.61

⊙	$Fe_{0.01}ZnO$[160]	37	92.00	1.38
⊙	$ZnO-LiOH$[161]	30	93.00	2.79
⊙	$Mg_xZn_{1-x}O$[162]	90	85.50	1.71
★	**This work**	82	95.26	11.95

When considering the mass of the carbon paper substrate, the overall areal and specific discharge capacities of the C-Ag-Zn anode were ~0.6 mAh cm^{-2} and ~52 mAh g^{-1}, respectively, which are not ready for practical application[149]. However, the mechanistic understanding and design principles of spatial control of Zn deposition reported here may be adopted in state-of-the-art Zn anodes, particularly those with high areal loading, to approach a practically relevant Zn anode for rechargeable aqueous batteries.

Besides carbon paper substrate, spatially controlled Zn deposition was also achieved on Ag-patterned stainless steel and Ni substrates (Figure 3.23, Figure 3.24). Yet the self-discharge of Zn and the hydrogen evolution on these patterned substrates were severe due to the high hydrogen evolution activities of stainless steel and Ni in alkaline electrolytes. Regarding the choice of seeding materials that can alloy with Zn, Cu lowers the potential barrier for Zn deposition as well, and has lower cost than Ag. Thus, Cu is a promising choice of Zn-alloying seed for large-scale applications.
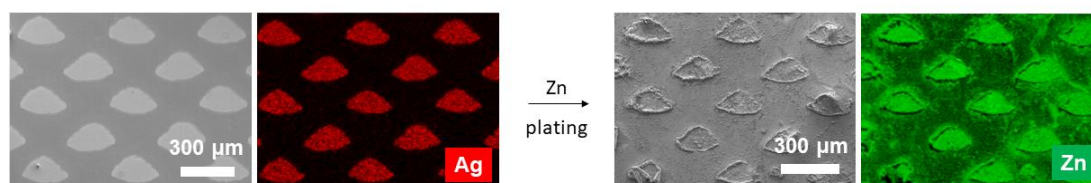
Figure 3.23 - SEM images and elemental mappings of stainless steel foil with patterned Ag islands before and after Zn plating (2.4 mA cm^{-2}). Patterned deposition of Zn is achieved due to the preferential Zn deposition on Ag.
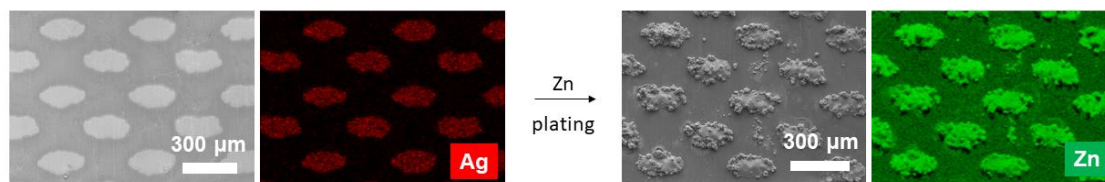
Figure 3.24 - SEM images and elemental mappings of Ni foil with patterned Ag islands before and after Zn plating (2.4 mA cm^{-2}). Patterned deposition of Zn is achieved due to the preferential Zn deposition on Ag.

Even though this study was conducted using alkaline electrolytes, the mechanistic understandings might also be applicable to Zn anode operating in neutral electrolytes. Zn metal deposition onto various substrates has been investigated in neutral electrolytes, including Ag, Cu, Fe, Ni, Au, Pt, Ti and C. Specifically, 100 nm of the corresponding metal film was evaporated onto a Cu foil. Then, three-electrode electrochemical cells were constructed that consisted of the substrate of interest as the working electrode, Zn foil as the reference electrode and Zn foil as the counter electrode. Zn metal was galvanostatically plated and stripped in a 2 M ZnSO$_4$ electrolyte. As shown in the voltage profiles (Figure 3.25), Cu, Ag, and Fe might be good candidates to modify Zn anodes for use in neutral electrolytes in terms of both Zn nucleation barrier and Coulombic efficiency.
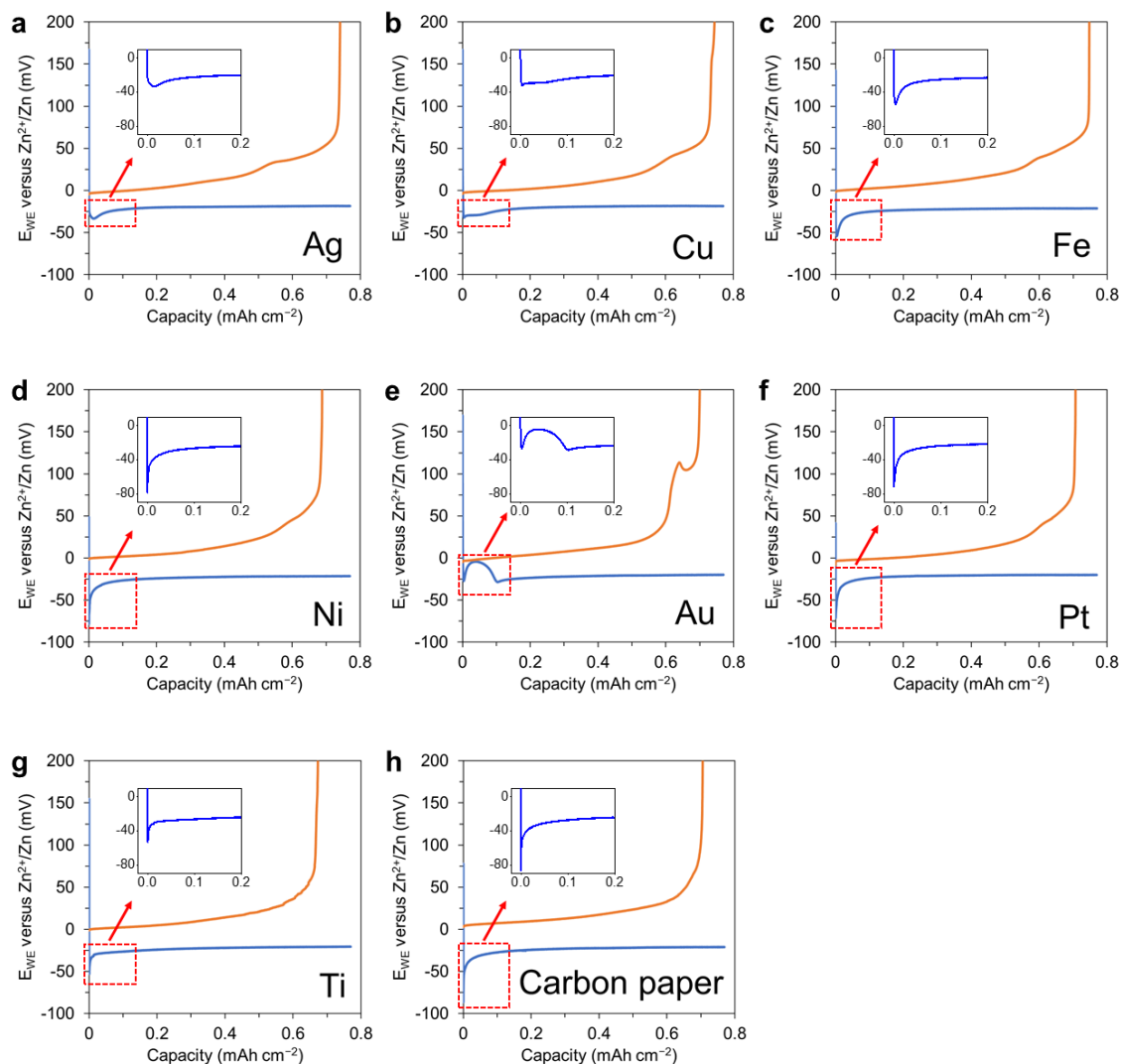
Figure 3.25 - Voltage profiles of galvanostatic Zn plating and stripping in 2 M ZnSO₄ electrolyte on various substrates at 3 mA cm⁻². The insets show the potential barrier of Zn nucleation. Three-electrode electrochemical cells were constructed: substrate of interest as the working electrode, Zn foil as the reference electrode and Zn foil as the counter electrode. Zn metal was galvanostatically deposited on the working electrode at 0.77 mA cm⁻² and stripped at 1.54 mA cm⁻².

3.4 Conclusion

In this work, the alloying mechanisms for the regulation of Zn electrodeposition were reported for the first time and achieved spatial control of Zn deposition by introducing metals that can alloy with and dissolve in Zn. As a proof of concept, Ag loaded on an inert

carbon paper substrate achieved a spatially controlled and uniform Zn deposition through heterogeneous seeded growth. Ag has two functions: (1) Ag, with a definite solubility in Zn, could help eliminate the heterogeneous Zn nucleation barrier and (2) the formation of Zn_xAg_{1-x} alloy phases occurs preferentially during Zn plating because of their negative Gibbs free energy of formation. As a result, the Ag nanoparticle-loaded carbon paper (C-Ag) achieved superior long-term cyclic stability compared with the C electrode. In addition, the spatially controlled Zn deposition was visualized in operando for the first time using an optical microscope. These findings can potentially guide the future design of high-performance Zn anodes in alkaline electrolytes. Similar mechanisms are expected for Zn anodes operating in neutral electrolytes as well as other metal anodes (e.g. Al, Mg, Na, K).

CHAPTER 4.   DEVICE CONSTRUCTION FOR ZINC ANODES

Zinc anodes suffer from severe hydrogen evolution issues in alkaline electrolytes, which are kinetically favorable for air cathodes. Through an electrochemical cell–gas chromatography setup, it was quantitatively identified that the capacity loss on the zinc anode is mainly caused by hydrogen evolution. Most previous research has focused on material design to suppress hydrogen evolution, while less attention has been paid to the device level. In this chapter, I demonstrate that the testing device material has an apparent effect on the hydrogen evolution reaction in an alkaline electrolyte. Stainless-steel coin cells, as common devices used in research laboratories, accelerate hydrogen evolution due to the synergistic effects of galvanic corrosion and a high hydrogen evolution activity, which cause a low Coulombic efficiency and short cycling life for alkaline Zn-based batteries. Plastic cells were successfully constructed to minimize hydrogen evolution, which demonstrate a higher Coulombic efficiency and longer cycling life than the stainless-steel coin cells. Specifically, the plastic cell with a zinc foil anode and NiOOH/Ni(OH)$_2$ cathode achieved stable long-term cycling for 816 cycles compared with ~100 cycles for the stainless-steel cell. The findings provide experimental insight into the choice of proper testing devices for Zn-based batteries.

4.1   Introduction

Zinc anodes suffer from passivation, shape change, and dendrite growth in alkaline electrolytes, which have recently been addressed to some extent[9,77,81,82,151,181]. However, the hydrogen evolution issue remains the main cause of the low Coulombic efficiency (CE) of zinc-based alkaline batteries. Hydrogen evolution follows two reactions: self-discharge

of zinc (electrons directly from the external circuit) and water electroreduction. Zinc is active in alkaline electrolytes and can thus react with them, which is known as self-discharge and decreases the shelf life of zinc batteries. Water electroreduction is a thermodynamically favored side reaction on the zinc anode during charging. The hydrogen gas evolved from these two reactions will dry the electrolyte and cause cell failure and even battery explosion.

Self-discharge: $Zn + 2OH^- + 2H_2O \rightarrow Zn(OH)_4{}^{2-} + H_2 \uparrow$

Water electroreduction: $2H_2O + 2e^- \rightarrow H_2 + 2OH^-$
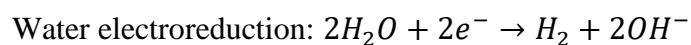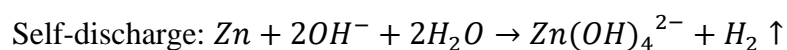
The hydrogen evolution reaction (HER) is a general problem for all aqueous battery anodes, which are of significant research interest. Over the years, in order to suppress the HER on zinc anodes, much research has been performed, resulting in approaches including anode surface treatments[84,85,182] and additives[86,183,184]. Most of these previous studies focused on material design to improve zinc anodes. However, less attention has been paid to the device level, which is demonstrated in this study to have an apparent effect on the HER in alkaline electrolytes. Coin cells made of stainless steel (SS) are widely used in research laboratories for zinc-based alkaline batteries[120,185–192] with the benefits of being small, fast and easy to assemble, and requiring small amounts of active materials. However, it was discovered that (1) the coin cell case made of SS accelerates the HER due to the synergistic effects of galvanic corrosion and a high HER activity, which cause a low CE and short cycling life for zinc-based batteries; and (2) a plastic cell case, in contrast, minimizes the HER and improves the electrochemical performance of zinc anodes.

4.2   Experimental Section

Material characterization and measurements. The morphological analyses were carried out using scanning electron microscopy (SEM, Hitachi SU 8230). Operando analyses and cyclic voltammetry were conducted using a VSP system (BioLogic). Battery cycling tests were carried out using LANHE operated in galvanostatic mode.

In the electrochemical cell–gas chromatography (GC) setup, an airtight battery system was connected to a GC with a thermal conductivity detector (TCD) (MG#5, SRI Instruments), and the system was purged with Ar before measurements. A stainless-steel (SS) rod was used as the anode and ZnO-saturated 4 M KOH (Sigma Aldrich) as the electrolyte. A 4 cm^2 cathode from a commercial Ni–Zn AA battery (PowerGenix), which is a mixture of NiOOH (~8 mAh/cm^2) and $Ni(OH)_2$ (~32 mAh/cm^2), was harvested to pair with the anode. The battery was charged at 20 mA for 15 min and then fully discharged (20 mA) to 0.8 V for 1 cycle. Then, H_2 and O_2 measurements were conducted using the GC-TCD with Ar as the carrier gas. The capacity loss on the zinc anode is almost fully caused by the HER.

Operando optical microscope characterization. Two-electrode electrochemical cells were constructed with the substrate of interest as the working electrode and zinc foil as the counter electrode. A ZnO-saturated 4 M KOH (Sigma Aldrich) aqueous solution was used as the electrolyte. The cells were observed using a Leica DMC2700 microscope with reflected dark-field illumination. Most of the images and videos were captured through an air-immersion objective (Leica N PLAN L 5×0.50 BD). All the operando experiments were performed at room temperature and ambient pressure.

Electrochemistry. The carbon paper (CP) and zinc foil anodes were cut to round disks with a diameter of 1 cm. The glass fiber (GE Healthcare, Whatman 10370003) separators were round disks with a diameter of 1.6 cm. The counter electrodes (cathodes) were NiOOH/Ni(OH)$_2$ harvested from commercial Ni–Zn AA batteries (PowerGenix). In order to specifically focus on the zinc anodes, they were paired with a NiOOH/Ni(OH)$_2$ cathode with excess capacity. The electrolyte was 100 µL of ZnO-saturated 4 M KOH (Sigma Aldrich). CR2032 cases (Kelude) made of 304 SS were used to assemble the SS coin cells. Plastic cell cases made of polytetrafluoroethylene were used to assemble the plastic cells. Ti wires were used as electrode terminals for the plastic cells.

The plastic cells and SS coin cells with CP anodes were galvanostatically charged to the cut-off voltage of 2 V or a charge capacity of 0.106 or 0.212 mAh/cm^2, followed by full discharge to 1.2 V. The plastic cells and SS coin cells with zinc foil anodes were galvanostatically discharged/charged to the cut-off voltage of 1.2 V/2 V or a discharge/charge capacity of 0.32 mAh/cm^2.

4.3   Results and Discussion

4.3.1   *SS coin cell case induces severe HER and low CE*

To focus on zinc anodes, NiOOH/Ni(OH)$_2$ cathodes with excess capacity of both NiOOH and Ni(OH)$_2$ was used to make full Ni–Zn batteries in this study. Therefore, the Coulombic inefficiency of the batteries can be directly correlated to side reactions on the zinc anode. NiOOH/Ni(OH)$_2$, a mixture of NiOOH (~8 mAh/cm^2) and Ni(OH)$_2$ (~32 mAh/cm^2), was harvested from the cathode of a commercial Ni–Zn AA battery (PowerGenix). To illustrate the HER problem when using SS coin cell cases, a SS coin cell

was assembled with a zinc foil round disk (1-cm diameter) as the anode, $NiOOH/Ni(OH)_2$ (~0.7 cm^2) as the cathode, and 100 μL of 4 M KOH as the electrolyte. The cell was galvanostatically cycled at 1.27 mA/cm^2 to the cut-off voltage of 1.2 V/2 V or a charge/discharge capacity of 0.32 mAh/cm^2. The calculation of areal parameters was based on the area of the anode if not otherwise specified. As shown in Error! Reference source not found.a and Figure 4.2, the SS coin cell gradually expanded over cycling, which indicates that gas accumulated in the sealed battery. After cycling for only 77 h, the cell components (electrodes, spacer, and spring) lost contact due to the cell expansion, which resulted in battery failure. With excess cathode materials in both the charged and discharged states ($NiOOH$ and $Ni(OH)_2$), the side reactions (e.g., oxygen evolution) on the cathode should be minimized. Thus, it was hypothesized that H_2 is the main gas component that causes cell expansion. To prove this hypothesis, an air-tight electrochemical cell was custom-made with an SS rod anode and excess $NiOOH/Ni(OH)_2$ cathode (4 cm^2), which was connected to a gas chromatograph (GC, Error! Reference source not found.b). The whole cell was purged with Ar before operation. Then, the cell was charged at 20 mA for 15 min and discharged at 20 mA to a cut-off voltage of 0.8 V in a ZnO-saturated 4 M KOH electrolyte, followed by gas-phase measurement through the GC with a thermal conductivity detector (TCD). It is worth mentioning that there was no initial active material on the anode. During charging, in addition to side reactions, zincates in the electrolyte are electrochemically reduced to zinc on the anode. During discharging, zinc is oxidized back to zincates. As shown in Error! Reference source not found.c, H_2 was produced after cycling, while a small amount of O_2 was detected, which, to some extent, proves that severe

HER is the main reason for the SS cell expansion shown in Error! Reference source not found.a.
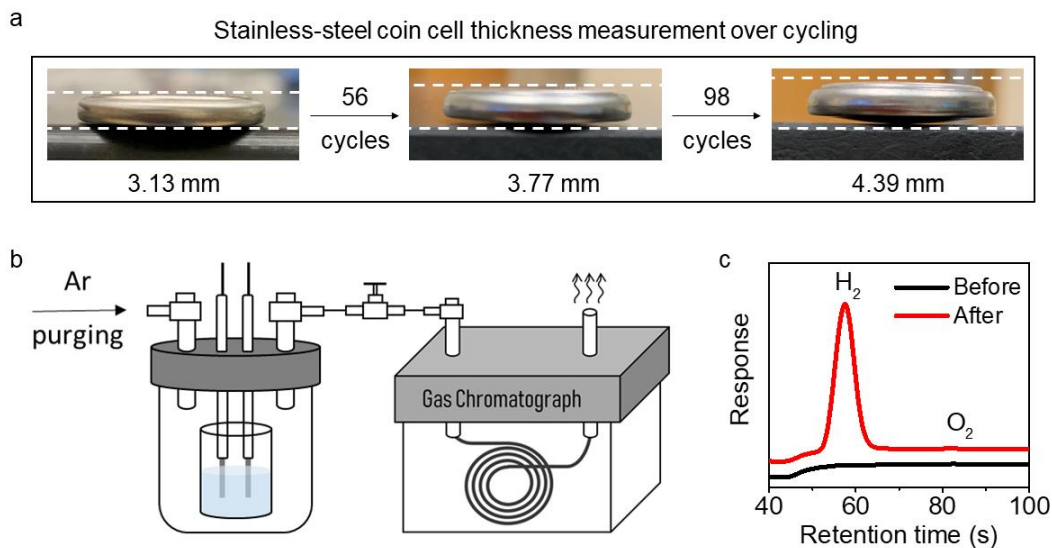
Figure 4.1 - SS coin cell expansion caused by the HER. a, Thickness measurement of a Ni–Zn coin cell over cycling with zinc foil as the anode. The coin cell case is SS. b, Schematic diagram of the battery–GC quantitative analysis method. c, GC-TCD analysis of the gas phase of the Ni–Zn battery before and after cycling in a ZnO-saturated 4 M KOH electrolyte. An SS rod was used as the anode.

Figure 4.2 - Thickness measurement of a Ni–Zn SS coin cell over cycling with zinc foil as the anode.

The influence of the HER on the capacity loss of zinc anodes was also quantitatively identified with the above electrochemical cell–GC setup. Figure 4.3 shows voltage profiles of the Ni–Zn battery, from which the capacity loss of the zinc anode was calculated by subtracting the discharge capacity from the charge capacity. The amount of

H$_2$ produced from the anode was determined by GC-TCD. The results show that 99.5% (87.34%/87.81%) of the capacity loss of the zinc anode was caused by the HER (Figure 4.4a). The other 0.5% of capacity loss was mainly attributed to the oxidation of Zn metal through reacting with trace O$_2$ generated from the cathode (oxygen reduction reaction (ORR)). Thus, it is concluded that the HER is the main side reaction occurring on the zinc anode. In other words, a high-CE zinc anode can be achieved by minimizing the HER.
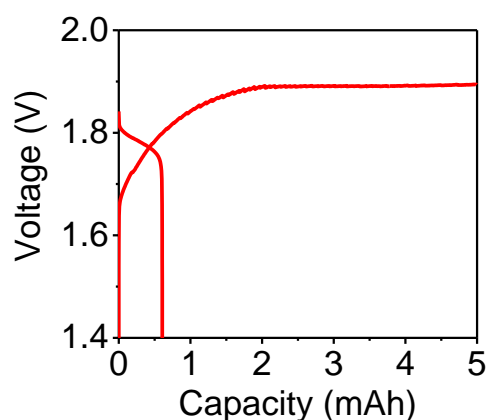
Figure 4.3 - Voltage profiles of the Ni–Zn battery connected to a GC.
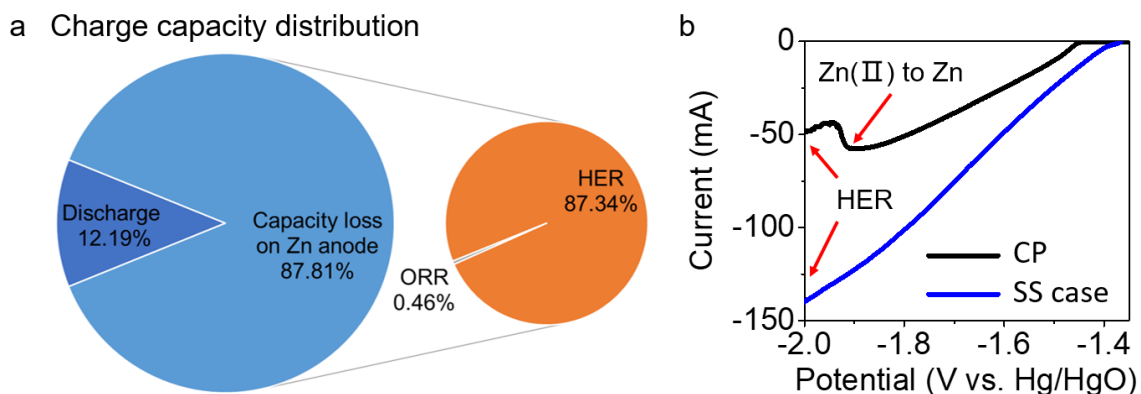
Figure 4.4 - Quantification of the HER on zinc anodes. a, Distribution of charge capacity on the anode in the Ni–Zn battery; 99.5% of the capacity loss on the zinc anode was caused by the HER. b, Cyclic voltammograms of the CP electrode and anode-side SS coin cell case at a 20-mV s^{-1} scan rate in a ZnO-saturated 4 M KOH electrolyte.

131

To study the effect of the SS coin cell case on the HER, cyclic voltammetry (CV) was carried out in a three-electrode electrochemical cell with a carbon paper round disk (1 cm diameter) or the anode-side SS coin cell case as the working electrode, Hg/HgO as the reference electrode, a graphite rod as the counter electrode, and ZnO-saturated 4 M KOH as the electrolyte (Figure 4.5). Carbon paper (CP) was used in this study as the current collector for the zinc anodes. As shown in Figure 4.4b, CP exhibits a clear zinc reduction peak at −1.9 V, while the SS case does not. Additionally, the absolute current of the SS case was much higher than that of the CP when the potential was more negative than −1.9 V. These results indicate that the HER on the SS case is more severe than on the CP. Notably, here, current instead of current density was used in order to directly illustrate the HER-related effect of the whole SS case on the anode instead of comparing the SS case and CP. Therefore, the HER on zinc anodes is accelerated by the use of an SS coin cell as the device to test alkaline zinc-based batteries. As a result, SS coin cells will show low CEs and short cycle lives.
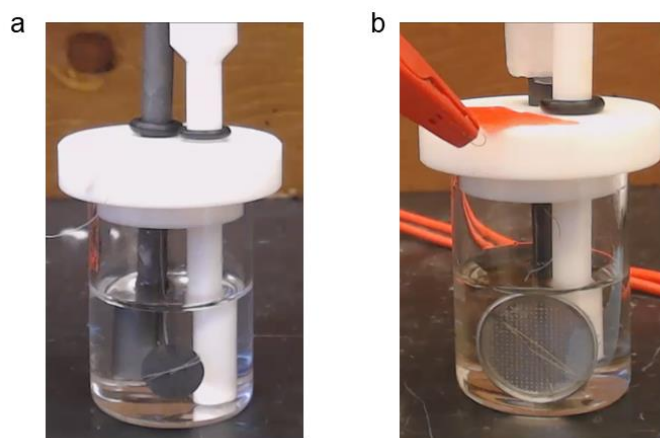
Figure 4.5 - Photos of beaker cell setup for cyclic voltammetry of the CP electrode (a) and the anode-side SS coin cell case (b). Ti wires were used as electrode terminals.

4.3.2   Plastic cell minimizes the HER

132

To minimize the HER induced by the testing device, plastic cell cases made of polytetrafluoroethylene (PTFE, Figure 4.6a and Error! Reference source not found.) were constructed. Ti wires were used as electrode terminals. Plastic cells and SS coin cells for comparison were then assembled containing CP anodes, excess NiOOH/Ni(OH)$_2$ cathodes, and a ZnO-saturated 4 M KOH electrolyte. The cells were cycled under charge–rest–discharge conditions (Figure 4.6b). Specifically, they were galvanostatically charged to the 2 V cut-off voltage or a charge capacity of 0.32 mAh/cm^2, followed by a rest period (0 or 30 min) and full discharge to 1.2 V. As shown in Figure 4.6c–d, plastic cells achieved higher CEs and discharge capacities than the SS coin cells in both rest periods, which demonstrates that the HER can be minimized using a plastic cell device. In addition, after 30 min of rest, the CE of the SS coin cells decayed from 70.1% to 50.3%. In contrast, there was only a slight decrease in the CE of the plastic cells from 92.7% to 91.9%. The dramatically decreased CE (~20%) after only 30 min of rest for the SS coin cells indicates that the self-discharge of zinc was accelerated by the SS case, which was believed to be due to galvanic corrosion. During charging, zinc is plated onto both the CP and anode-side SS case. Thus, zinc metal contacts the SS in the electrolyte and corrodes. In other words, the self-discharge of zinc is accelerated. To visualize the self-discharge of zinc on the SS case, operando optical microscopy analysis on a zinc-plated SS case (Figure 4.6e) was conducted. During the rest period, zinc corroded and thus hydrogen formed gradually on the SS case surface (Figure 4.6f).
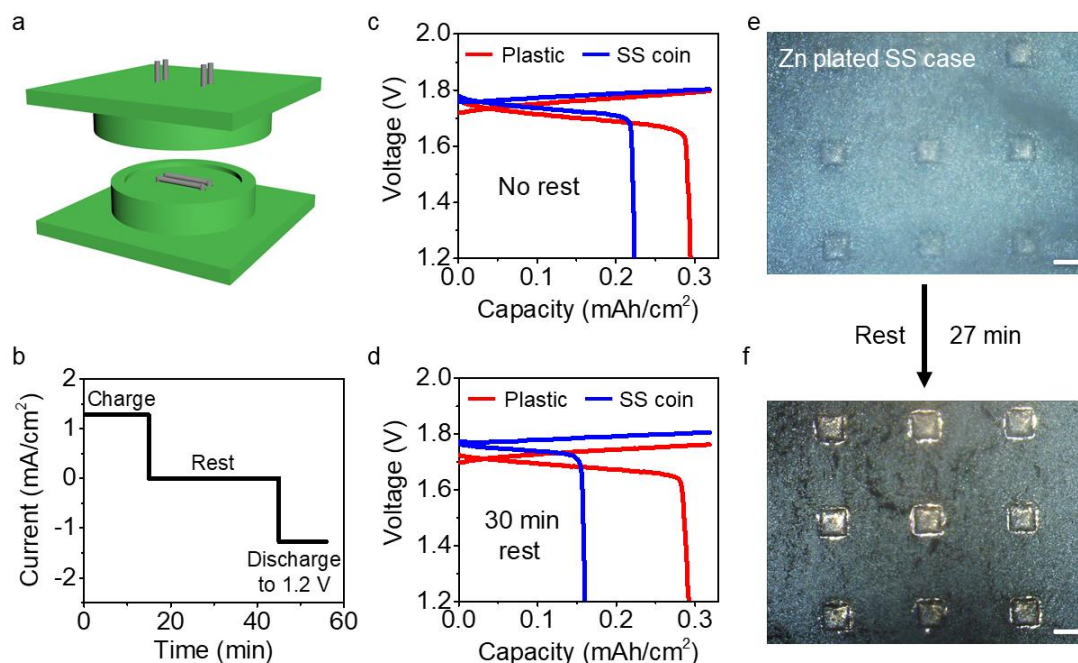
Figure 4.6 - Plastic cell increases the Coulombic efficiency. a, Device construction diagram of the plastic cell. b, Current density profiles as cycled under charge–rest–discharge conditions. c,d, Voltage profiles of Ni–Zn batteries tested in both plastic cells and SS coin cells with a rest time of 0 (c) and 30 min (d). CP electrodes were used as anodes. e,f, Operando optical microscopy images of the zinc-plated SS coin cell case before (e) and after (f) resting in ZnO-saturated 4 M KOH electrolyte for ~27 min. Scale bars: 200 μm.
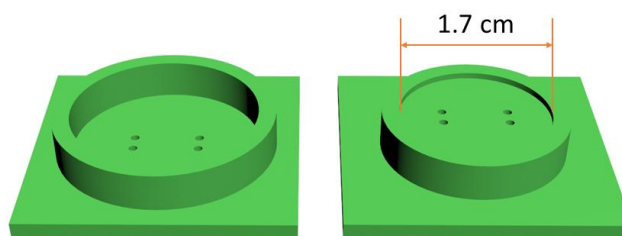
Figure 4.7 - Device diagram of plastic cell case. The holes were designed for the Ti wire electrode terminals.

In addition, operando visualization of the zinc-plating process on the SS case was also performed. Numerous bubbles formed along with zinc deposition. This result is in good agreement with the CV analysis showing that the HER is severe on SS, which may be due to the presence of nickel[193] in the 304 SS used in this study (Error! Reference source

134

not found.). Coin cells made of 316 SS also showed a low CE of ~70% (Figure 4.9). Thus, when using SS coin cell devices for alkaline zinc-based batteries, the HER will be accelerated by the synergistic effects of galvanic corrosion and the high HER activity of SS. In contrast, the use of non-conductive plastic cells with Ti wires as electrode terminals could minimize the HER.
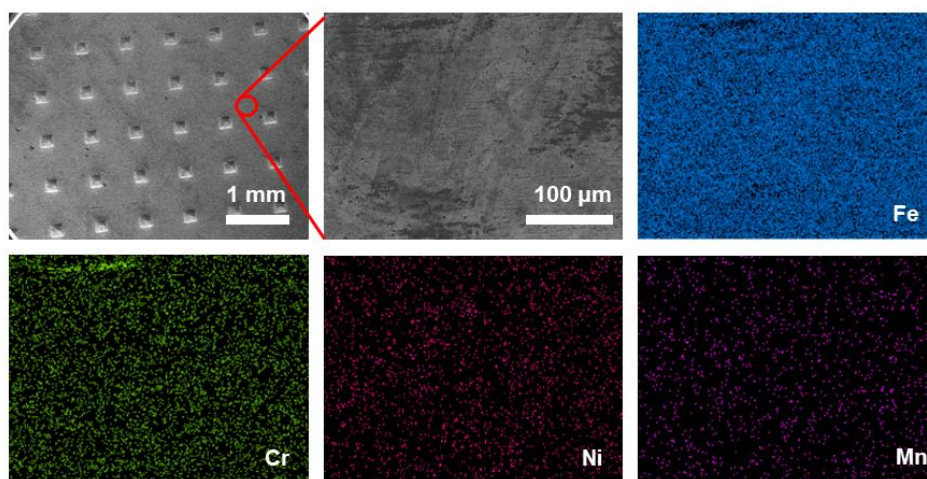
Figure 4.8 - SEM images and elemental mappings of the CR2032 coin cell case made of 304 SS.
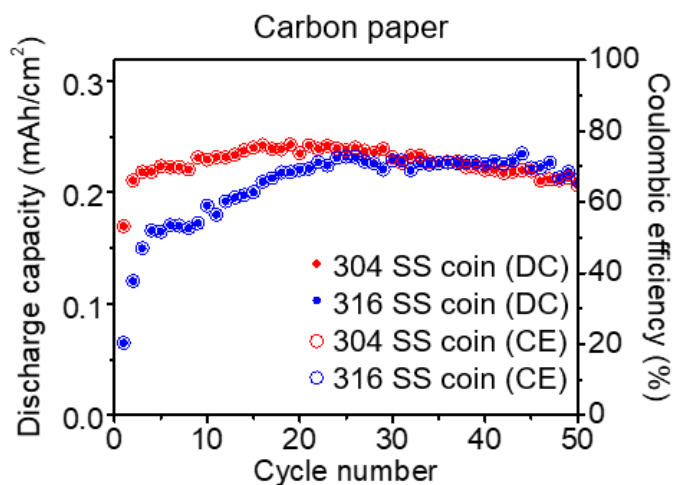
Figure 4.9 - Cycling performance of CP anodes in coin cells made with 304 and 316 SS. The cells were galvanostatically charged to the cut-off voltage of 2 V or a charge

capacity of 0.32 mAh/cm^2, followed by full discharge to 1.2 V in a ZnO-saturated 4 M KOH electrolyte. The 316 SS coin cell cases were purchased from Hohsen.

4.3.3   Superior cycling performance of plastic cells

The cycling performance of plastic cells and SS coin cells with CP anodes was also tested. Similar to previous experiments, the cells were galvanostatically charged to the cut-off voltage of 2 V or a charge capacity of 0.106 (Figure 4.10a) or 0.212 mAh/cm^2 (Figure 4.10b), followed by full discharge to 1.2 V. The plastic cells demonstrated a better electrochemical performance than the SS coin cells. When the charge capacity was limited to 0.106 mAh/cm^2, the plastic cells achieved a higher average CE of 95.1% compared with 74.0% for the SS coin cells. With a charge capacity limit of 0.212 mAh/cm^2, the plastic cells also exhibited a higher average CE (94.8%) than the SS coin cells (49.8%). Because the CP anodes were cycled at 100% DOD and paired with excess cathode material, the extent of the side reactions occurring on the CP anode can be directly correlated to the cell Coulombic inefficiency. In addition, as discussed above, the HER is the main side reaction on the zinc anode. Thus, it can be concluded that the high CE of the plastic cells is attributable to the minimized HER on the plastic cell case. Instead of CP anodes with no loaded active materials, both plastic cells and SS coin cells with zinc foil anodes (Figure 4.10c) were also galvanostatically cycled. They were discharged/charged to the cut-off voltage of 1.2 V/2 V or a discharge/charge capacity of 0.32 mAh/cm^2. With the minimized HER, the plastic cells achieved stable long-term cycling for 816 cycles compared with ~100 cycles for the SS coin cell. Voltage profiles of the plastic cells with CP and zinc foil anodes are shown in Figure 4.11 and Figure 4.12 - Voltage profile of a Ni–Zn battery with a zinc foil anode in a plastic cell. The cell was galvanostatically discharged/charged to the cut-off voltage of 1.2 V/2 V or a discharge/charge capacity of 0.32 mAh/cm^2 in a ZnO-saturated 4 M KOH electrolyte. Cycle range: 50th–60th.

. Instead of PTFE, plastic cell cases using a cheaper material, Delrin, were also

constructed. Similarly, the Delrin plastic cells also demonstrated a better electrochemical

performance than the SS coin cells (Figure 4.13). Thus, even though the battery components were the same, the plastic cells achieved a better electrochemical performance than the SS coin cells. These results reveal that the choice of testing device is important for analyzing zinc-based alkaline batteries.
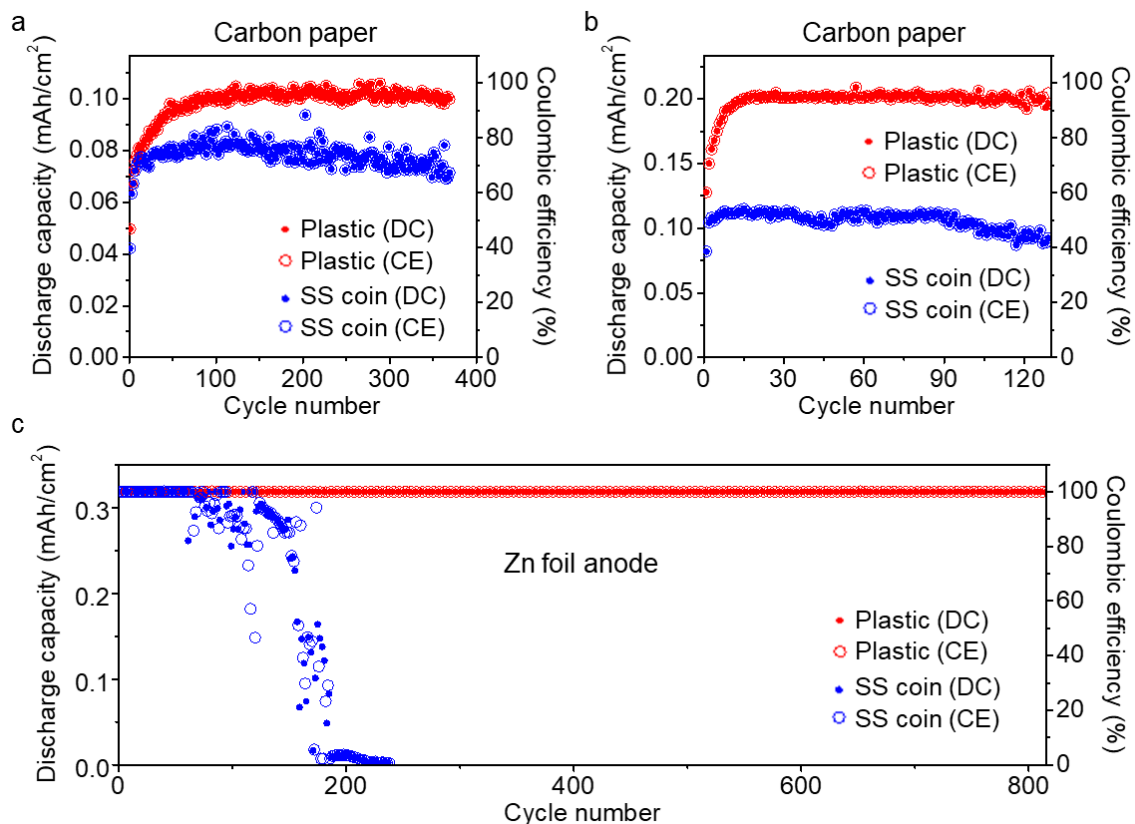
Figure 4.10 - Electrochemical performance of plastic cells and SS coin cells. a,b, Cycling performance of CP anodes in ZnO-saturated 4 M KOH electrolyte when galvanostatically charged to the 2 V cut-off voltage or charge capacities of 0.106 (a) and 0.212 mAh/cm^2 (b), followed by full discharge to 1.2 V. c, Cycling performance of zinc foil anodes in a 4 M KOH electrolyte when galvanostatically discharged/charged to the 1.2 V/2 V cut-off voltage or a discharge/charge capacity of 0.32 mAh/cm^2. Anode current density in all cells: 1.27 mA/cm^2. DC: discharge capacity. CE: Coulombic efficiency.
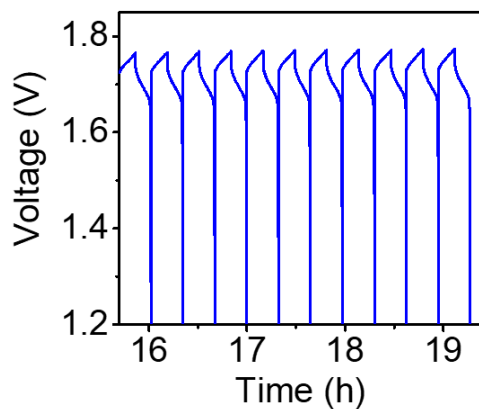
Figure 4.11 - Voltage profile of a Ni–Zn battery with a CP anode in a plastic cell. The cell was galvanostatically charged to the cut-off voltage of 2 V or a charge capacity of 0.212 mAh/cm^2, followed by full discharge to 1.2 V in a ZnO-saturated 4 M KOH electrolyte. Cycle range: 50th–60th.
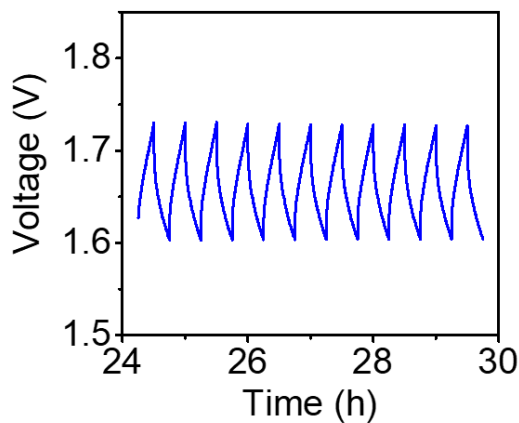
Figure 4.12 - Voltage profile of a Ni–Zn battery with a zinc foil anode in a plastic cell. The cell was galvanostatically discharged/charged to the cut-off voltage of 1.2 V/2 V or a discharge/charge capacity of 0.32 mAh/cm^2 in a ZnO-saturated 4 M KOH electrolyte. Cycle range: 50th–60th.
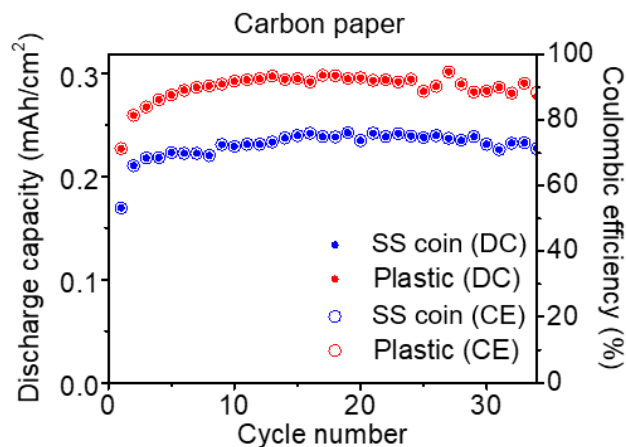
Figure 4.13 - Cycling performance of CP anodes in a Delrin plastic cell and SS coin cell. The cells were galvanostatically charged to the cut-off voltage of 2 V or a charge capacity of 0.32 mAh/cm², followed by full discharge to 1.2 V in a ZnO-saturated 4 M KOH electrolyte.

4.4   Conclusion

In this work, through an electrochemical cell–GC setup, it was quantitatively identified that the capacity loss on zinc anodes is mainly caused by the HER. It was also demonstrated that the testing device has a notable influence on the HER in alkaline zinc-based batteries. SS coin cells, as widely used devices in research laboratories, accelerate the HER due to the synergistic effects of galvanic corrosion and a high HER activity, which cause a low CE and short cycling life. Plastic cells were successfully constructed to minimize the HER. As a result, the plastic cells demonstrated a higher CE and longer cycling life than the SS coin cells. These findings provide insights into choosing proper testing devices for zinc-based batteries.

CHAPTER 5.   CONCLUSIONS AND FUTURE DIRECTIONS

Batteries with aqueous electrolytes generally feature better intrinsic safety, higher ionic conductivity and lower cost compared with flammable organic electrolytes. Metallic zinc as a rechargeable anode material for aqueous batteries has gained tremendous attention with merits of intrinsic safety, low cost, and high theoretical volumetric capacity (5854 mAh cm^{-3}). Among zinc-based batteries, Zn-air batteries are promising with highest theoretical volumetric energy density (~3x of traditional LIBs). Rechargeable zinc anode has achieved big progress in neutral electrolytes, yet developed slowly in alkaline electrolytes, which are kinetically favorable for air cathodes. Passivation, dissolution, hydrogen evolution reaction (HER), and dendrite formation are four reasons for irreversibility of zinc anodes in alkaline electrolytes.

5.1   Conclusions

This thesis describes systematic approaches to understand and improve zinc anodes for high-energy rechargeable alkaline batteries from three aspects, which are material, mechanism, and device.

From the aspect of material (**_Chapter 2_**), 4 types of zinc anodes have been designed and synthesized to overcome multiple issues simultaneously and improve their reversibility. These anodes include graphene oxide-modified (Zn@GO), lasagna-inspired (ZnO@GO), sealed (ZnO@TiN$_x$O$_y$), and hydrogen-evolution-suppressing (ZnO@TiO$_2$) anodes, which improve the deep cycling performance when cycled at lean electrolyte.

(1) Zn@GO structure has the following advantages: (i) During cycling, $Zn(OH)_4^{2-}$ will be blocked by the GO compared to H_2O and OH^-. Thus, the active material loss of anodes can be minimized. (ii) zincate can form hydrogen bonds with oxygen-containing groups on the GO surface and thus has a good affinity with GO, which results in a relatively uniform distribution of zincate among GO layers during the reaction. Once the zincate reaches its solubility, it will decompose to ZnO, which will be encapsulated by GO. The GO encapsulation of ZnO can create the desirable environment for free transportation of electrons and therefore makes ZnO electrochemically active.

(2) ZnO lasagna structure has three features: (i) the size of ZnO nanoparticles is smaller than the critical size of passivation; (ii) the fabrication of ZnO lasagna anode starts with commercially available ZnO nanoparticles (~100 nm), and is compatible with the roll-to-roll process, which is ideal for large-scale manufacturing; (iii) GO allows permeation of OH^- and H_2O, and prevents loss of Zn active material through blocking bigger $Zn(OH)_4^{2-}$.

(3) $ZnO@TiN_xO_y$ structure has a few advantages: (i) the feature size of ZnO nanorod is smaller than critical passivation size; (ii) the carbon paper framework and TiN_xO_y coating, which encapsulates ZnO nanorod, function as an electrical pathway so that all ZnO nanorods are electrochemically active; (iii) the TiN_xO_y coating enables fast hydroxide/water diffusion as well as blocks large zincates from escaping during electrochemical cycling, thus prevents anode structure fracture.

(4) $ZnO@TiO_2$ features the following advantages: (i) sub-micron-sized ZnO avoids passivation and allows complete utilization of the active materials; (ii) ion-sieving coating layer confines zincate inside and mitigates shape changes of the electrode; and (iii) the

coating layer is made of HER suppressing material, which represses side reactions. The results demonstrate that HER suppressing sealed nanorod (HSSN) zinc anodes exhibit long cycle life, high Coulombic efficiency, and high specific discharge capacity.

From the aspect of mechanism (***Chapter 3***), the underlying mechanism of the spatial control of zinc deposition on zinc alloy anodes has been elucidated for the first time. The thermodynamic and atomic mechanisms of heterogeneous seeded growth were studied both experimentally and computationally (CALPHAD and DFT). Spatially controlled and nondendritic Zn deposition was achieved by inducing Zn alloying and soluble metals on Zn anodes to nucleate and accommodate Zn. The spatially controlled Zn deposition was visualized for the first time by operando optical microscopy. As a result, the Ag-loaded Zn anode exhibited comprehensively superior cycling performance compared with previously reported deeply cycled Zn anodes in alkaline electrolytes.

From the aspect of device (***Chapter 4***), it was demonstrated that the testing device material has a clear effect on the HER in alkaline zinc-based batteries. In addition, the capacity loss on the zinc anode is mainly caused by the HER as identified quantitatively HER through an electrochemical cell–gas chromatography analysis method. Specifically, stainless-steel coin cells, as widely used devices in research laboratories, accelerate the HER due to the synergistic effects of galvanic corrosion and a high HER activity. Plastic cells were successfully constructed and HER was minimized, resulting in a higher Coulombic efficiency and longer cycling life than the stainless-steel coin cell.

5.2   Future Directions

Previously reported Zn–air cell data shows that secondary Zn–air systems may achieve high specific energies ranging between 200–450 Wh kg_{sys}^{-1}, which is competitive with projections for up-and-coming Li-based battery systems. In order for rechargeable Zn–air batteries to achieve such projected specific-energy values and demonstrate device-appropriate cycle lives, both rechargeable Zn anodes and air cathodes need to be improved.

Depth of discharge, areal discharge capacity, and solid-volume fraction of the porous Zn electrode are the most sensitive parameters to increase specific energy. With lower depth of discharge, higher theoretical areal capacity is required, which means lower specific energy density. It is vital to improve the depth of discharge while maintain the reversibility of Zn anodes. Porosity or solid-volume fraction should also be designed in order to achieve sufficient electrode-electrolyte contact while maintain high volumetric energy density. Future rechargeable Zn anode design can be focused on achieving high-energy Zn anodes, with high practical areal discharge capacity of >50 mAh/cm^2 for over 100 cycles. Design principles shown in this thesis can be applied, such as ion-sieving and hydrogen evolution coatings and alloy seeded Zn anode design.

For air cathodes, future research can be focused on investigating novel, inexpensive bifunctional electrocatalysts that exhibit bifunctionality, versatility, and scalability. Bifunctional catalysts are needed to boost both the oxygen reduction reaction and oxygen evolution reaction kinetics to practically usable levels in zinc–air batteries because the kinetics for the electrochemical oxygen reactions are generally rather slow. These catalysts should be able to function in a wide range of temperatures, voltages, and in both aqueous

143

and nonaqueous electrolytes. Moreover, they should be easy to be incorporated into the air-electrode structure and enable commercialization and widespread adoption.

REFERENCES

1. Obama, B. The irreversible momentum of clean energy. *Science (80-.).* **355**, 126–129 (2017).

2. Chu, S., Cui, Y. & Liu, N. The path towards sustainable energy. *Nat. Mater.* **16**, 16–22 (2017).

3. Zhang, Y. & Liu, N. Nanostructured Electrode Materials for High-Energy Rechargeable Li, Na and Zn Batteries. *Chem. Mater.* **29**, 9589–9604 (2017).

4. Wu, Y. & Liu, N. Visualizing Battery Reactions and Processes by Using In Situ and In Operando Microscopies. *Chem* **4**, 438–465 (2018).

5. Liu, N. *et al.* A pomegranate-inspired nanoscale design for large-volume-change lithium battery anodes. *Nat. Nanotechnol.* **9**, 187–192 (2014).

6. Jin, Y., Zhu, B., Lu, Z., Liu, N. & Zhu, J. Challenges and Recent Progress in the Development of Si Anodes for Lithium-Ion Battery. *Adv. Energy Mater.* **7**, 1700715 (2017).

7. Lin, D. *et al.* A Silica-Aerogel-Reinforced Composite Polymer Electrolyte with High Ionic Conductivity and High Modulus. *Adv. Mater.* **30**, 1802661 (2018).

8. Wan, J. *et al.* Status, promises, and challenges of nanocomposite solid-state electrolytes for safe and high performance lithium batteries. *Mater. Today Nano* **4**, 1–16 (2018).

9. Zhang, Y. *et al.* Sealing ZnO nanorods for deeply rechargeable high-energy aqueous battery anodes. *Nano Energy* **53**, 666–674 (2018).

10. Liang, Y. *et al.* Universal quinone electrodes for long cycle life aqueous rechargeable batteries. *Nat. Mater.* **16**, 841–848 (2017).

11. Kim, H. *et al.* Aqueous rechargeable Li and Na ion batteries. *Chem. Rev.* **114**, 11788–11827 (2014).

12. Kundu, D., Adams, B. D., Duffort, V., Vajargah, S. H. & Nazar, L. F. A high-capacity and long-life aqueous rechargeable zinc battery using a metal oxide intercalation cathode. *Nat. Energy* **1**, 16119 (2016).

13. Liu, P., Ross, R. & Newman, A. Long-range, low-cost electric vehicles enabled by robust energy storage. *MRS Energy Sustain.* **2**, E12 (2015).

14. Pan, H. *et al.* Reversible aqueous zinc/manganese oxide energy storage from conversion reactions. *Nat. Energy* **1**, 16039 (2016).

15. Zhang, N. *et al.* Rechargeable aqueous zinc-manganese dioxide batteries with high energy and power densities. *Nat. Commun.* **8**, 405 (2017).

16. Luo, J.-Y., Cui, W.-J., He, P. & Xia, Y.-Y. Raising the cycling stability of aqueous lithium-ion batteries by eliminating oxygen in the electrolyte. *Nat. Chem.* **2**, 760–765 (2010).

17. Pasta, M. *et al.* Full open-framework batteries for stationary energy storage. *Nat. Commun.* **5**, 3007 (2014).

18. USGS. *Mineral Commodity Summaries 2019*. (2019).

19. Wan, F. *et al.* Aqueous rechargeable zinc/sodium vanadate batteries with enhanced performance from simultaneous insertion of dual carriers. *Nat. Commun.* **9**, 1656 (2018).

20. Huang, J. *et al.* Polyaniline-intercalated manganese dioxide nanolayers as a high-performance cathode material for an aqueous zinc-ion battery. *Nat. Commun.* **9**, 2906 (2018).

21. Yuan, Z. *et al.* Negatively charged nanoporous membrane for a dendrite-free alkaline zinc-based flow battery with long cycle life. *Nat. Commun.* **9**, 3731 (2018).

22. Verma, V., Kumar, S., Manalastas Jr., W., Satish, R. & Srinivasan, M. Progress in Rechargeable Aqueous Zinc- and Aluminum-Ion Battery Electrodes: Challenges and Outlook. *Adv. Sustain. Syst.* **3**, 1800111 (2019).

23. Khor, A. *et al.* Review of zinc-based hybrid flow batteries: From fundamentals to applications. *Mater. Today Energy* **8**, 80–108 (2018).

24. Yang, Y. *et al.* Li + intercalated V 2 O 5 · n H 2 O with enlarged layer spacing and fast ion diffusion as an aqueous zinc-ion battery cathode. *Energy Environ. Sci.* **11**, 3157–3162 (2018).

25. Biswas, S. *et al.* Minimal architecture zinc-bromine battery for low cost electrochemical energy storage. *Energy Environ. Sci.* **10**, 114–120 (2017).

26. Li, H. *et al.* An extremely safe and wearable solid-state zinc ion battery based on a hierarchical structured polymer electrolyte. *Energy Environ. Sci.* **11**, 941–951 (2018).

27. Mo, F. *et al.* A flexible rechargeable aqueous zinc manganese-dioxide battery working at -20 °C. *Energy Environ. Sci.* (2019). doi:2019/EE/C8EE02892C

28. Zhao, Q. *et al.* High-capacity aqueous zinc batteries using sustainable quinone electrodes. *Sci. Adv.* **4**, eaao1761 (2018).

29. Fu, J. *et al.* Electrically Rechargeable Zinc–Air Batteries: Progress, Challenges, and

Perspectives. *Adv. Mater.* **29**, (2017).

30. Li, Y. & Dai, H. Recent advances in zinc–air batteries. *Chem. Soc. Rev.* **43**, 5257–5275 (2014).

31. Xu, M., Ivey, D. G., Xie, Z. & Qu, W. Rechargeable Zn-air batteries: Progress in electrolyte development and cell configuration advancement. *J. Power Sources* **283**, 358–371 (2015).

32. Zeng, Z. *et al.* Exploration of nanowire- and nanotube-based electrocatalysts for oxygen reduction and oxygen evolution reaction. *Mater. Today Nano* **3**, 54–68 (2018).

33. Su, C.-Y. *et al.* Atomic Modulation of FeCo–Nitrogen–Carbon Bifunctional Oxygen Electrodes for Rechargeable and Flexible All-Solid-State Zinc–Air Battery. *Adv. Energy Mater.* **7**, 1602420 (2017).

34. Pan, J. *et al.* Advanced Architectures and Relatives of Air Electrodes in Zn-Air Batteries. *Adv. Sci.* **1700691**, (2018).

35. Li, Y. & Lu, J. Metal–Air Batteries: Will They Be the Future Electrochemical Energy Storage Device of Choice? *ACS Energy Lett.* **2**, 1370–1377 (2017).

36. Zhang, N. *et al.* Rechargeable aqueous zinc-manganese dioxide batteries with high energy and power densities. *Nat. Commun.* **8**, 405 (2017).

37. Wang, F. *et al.* A rechargeable aqueous Zn 2+ -battery with high power density and a long cycle-life. *Energy Environ. Sci.* **11**, 3168–3175 (2018).

38. Wang, F. *et al.* Highly reversible zinc metal anode for aqueous batteries. *Nat. Mater.* **17**, 543–549 (2018).

39. Chen, C.-Y., Matsumoto, K., Kubota, K., Hagiwara, R. & Xu, Q. A Room-Temperature Molten Hydrate Electrolyte for Rechargeable Zinc–Air Batteries. *Adv. Energy Mater.* **9**, 1900196 (2019).

40. Yi, J. *et al.* Challenges, mitigation strategies and perspectives in development of zinc-electrode materials and fabrication for rechargeable zinc-air batteries. *Energy Environ. Sci.* **11**, 3075–3095 (2018).

41. Li, Y. *et al.* Advanced zinc-air batteries based on high-performance hybrid electrocatalysts. *Nat. Commun.* **4**, 1805–1807 (2013).

42. Rojas-Carbonell, S. *et al.* Effect of pH on the Activity of Platinum Group Metal-Free Catalysts in Oxygen Reduction Reaction. *ACS Catal.* **8**, 3041–3053 (2018).

43. Zhang, J., Zhou, Q., Tang, Y., Zhang, L. & Li, Y. Zinc–air batteries: are they ready for prime time? *Chem. Sci.* **10**, 8924–8929 (2019).

44. Liu, M.-B. Passivation of Zinc Anodes in KOH Electrolytes. *Journal of The Electrochemical Society* **128**, 1663 (1981).

45. McBreen, J. & Gannon, E. Bismuth oxide as an additive in pasted zinc electrodes. *J. Power Sources* **15**, 169–177 (1985).

46. Diomidis, N. & Celis, J.-P. Anodic Film Formation on Zinc in Alkaline Electrolytes Containing Silicate and Tetraborate Ions. *J. Electrochem. Soc.* **154**, C711 (2007).

47. Hampson, N. A. & Tarbox, M. J. The Anodic Behavior of Zinc in Potassium Hydroxide Solution I Horizontal Anodes. *J. Electrochem. Soc.* **110**, 95–98 (1963).

48. Baugh, L. M. & Higginson, A. Passivation of zinc in concentrated alkaline solution-I. Characteristics of active dissolution prior to passivation. *Electrochim. Acta* **30**, 1163–1172 (1985).

49. Jung, C. Y., Kim, T. H., Kim, W. J. & Yi, S. C. Computational analysis of the zinc utilization in the primary zinc-air batteries. *Energy* **102**, 694–704 (2016).

50. Parker, J. F., Ko, J. S., Rolison, D. R. & Long, J. W. Translating Materials-Level Performance into Device-Relevant Metrics for Zinc-Based Batteries. *Joule* (2018). doi:https://doi.org/10.1016/j.joule.2018.11.007

51. Chang, T. S., Wang, Y. Y. & Wan, C. C. Structural effect of the zinc electrode on its discharge performance. *J. Power Sources* **10**, 167–177 (1983).

52. Einerhand, R. E. F., Visscher, W., de Goeij, J. J. M. & Barendrecht, E. Zinc Electrode Shape Change I. In Situ Monitoring. *J. Electrochem. Soc.* **138**, 1 (1991).

53. Deiss, E., Holzer, F. & Haas, O. Modeling of an electrically rechargeable alkaline Zn-air battery. *Electrochim. Acta* **47**, 3995–4010 (2002).

54. McBreen, J. Zinc Electrode Shape Change in Secondary Cells. *J. Electrochem. Soc.* **119**, 1620 (1972).

55. Choi, K. W. Engineering Analysis of Shape Change in Zinc Secondary Electrodes. *J. Electrochem. Soc.* **123**, 1628 (1976).

56. Einerhand, R. E. F., Visscher, W., de Goeij, J. J. M. & Barendrecht, E. Zn Electrode Shape Chang II. Process and Mechanism. *J. Electrochem. Soc.* **138**, 7–17 (1991).

57. Otani, T., Fukunaka, Y. & Homma, T. Effect of lead and tin additives on surface morphology evolution of electrodeposited zinc. *Electrochim. Acta* **242**, 364–372 (2017).

58. DIRKSE, T. P. & Hampson, N. A. The Zn(II) Zn exchange reaction in KOH solution—II. exchange current density measurements using the double-impulse method. *Electrochim. Acta* **17**, 383–386 (1972).

59. Gagnon, E. G. Effects of KOH Concentration on the Shape Change and Cycle Life of Zn / NiOOH Cells. *Journal of The Electrochemical Society* 1989–1995 (1989).

60. Nichols, J. T., Mclarnon, F. R. & Cairns, E. J. Zinc electrode cycle-life performance in alkaline electrolytes having reduced zinc species solubility. *Chem. Eng. Commun.* **38**, 357–381 (1985).

61. McBreen, J. Rechargeable zinc batteries. *J. Electroanal. Chem.* **168**, 415–432 (1984).

62. Banik, S. J. & Akolkar, R. Suppressing Dendritic Growth during Alkaline Zinc Electrodeposition using Polyethylenimine Additive. *Electrochim. Acta* **179**, 475–481 (2015).

63. Wranglén, G. Dendrites and growth layers in the electrocrystallization of metals. *Electrochim. Acta* **2**, 130–143 (1960).

64. Diggle, J. W., Despic, A. R. & Bockris, J. O. The Mechanism of the Dendritic Electrocrystallization of Zinc. *J. Electrochem. Soc.* **116**, 1503 (1969).

65. Sun, K. E. K. *et al.* Suppression of Dendrite Formation and Corrosion on Zinc Anode of Secondary Aqueous Batteries. *ACS Appl. Mater. Interfaces* **9**, 9681–9687 (2017).

66. Aleksandra Gavrilović-Wohlmuther, Andreas Laskos, Christian Zelger, Bernhard Gollas & Adam Harding Whitehead. Effects of Electrolyte Concentration, Temperature, Flow Velocity and Current Density on Zn Deposit Morphology. *J. Energy Power Eng.* **9**, 1019–1028 (2015).

67. Li, Y. & Dai, H. Recent advances in Zinc-air batteries. *Chem. Soc. Rev.* **43**, 5257–5275 (2014).

68. Popov, K. I., Maksimović, M. D., Trnjančev, J. D. & Pavlović, M. G. Dendritic electrocrystallization and the mechanism of powder formation in the potentiostatic electrodeposition of metals. *J. Appl. Electrochem.* **11**, 239–246 (1981).

69. Despic, A. R., Diggle, J. & Bockris, J. O. Mechanism of the Formation of Zinc Dendrites. *J. Electrochem. Soc.* **115**, 507 (1968).

70. Parker, J. F. *et al.* Rechargeable nickel–3D zinc batteries: An energy-dense, safer alternative to lithium-ion. *Science (80-.).* **356**, 415–418 (2017).

71. Einerhand, R. E. F., Visscher, W. H. M. & Barendrecht, E. Hydrogen production during zinc deposition from alkaline zincate solutions. *J. Appl. Electrochem.* **18**, 799–806 (1988).

72. Kim, H. *et al.* Metallic anodes for next generation secondary batteries. *Chem. Soc. Rev.* **42**, 9011–9034 (2013).

73. Gu, P. *et al.* Rechargeable zinc–air batteries a promising way to green energy. *J. Mater. Chem. A* **5**, 7651–7666 (2017).

74. Liu, J. *et al.* A Flexible Quasi-Solid-State Nickel–Zinc Battery with High Energy and Power Densities Based on 3D Electrode Design. *Adv. Mater.* **28**, 8732–8739 (2016).

75. Wang, L., Yang, Z., Chen, X., Qin, H. & Yan, P. Formation of porous ZnO microspheres and its application as anode material with superior cycle stability in zinc-nickel secondary batteries. *J. Power Sources* **396**, 615–620 (2018).

76. Yan, X., Chen, Z., Wang, Y., Li, H. & Zhang, J. In-situ growth of ZnO nanoplates on graphene for the application of high rate flexible quasi-solid-state Ni-Zn secondary battery. *J. Power Sources* **407**, 137–146 (2018).

77. Zhou, Z. *et al.* Graphene oxide-modified zinc anode for rechargeable aqueous batteries. *Chem. Eng. Sci.* **194**, 142–147 (2019).

78. Yan, Y. *et al.* A Lasagna-Inspired Nanoscale ZnO Anode Design for High-Energy Rechargeable Aqueous Batteries. *ACS Appl. Energy Mater.* **1**, 6345–6351 (2018).

79. Parker, J. F. *et al.* Rechargeable nickel–3D zinc batteries: An energy-dense, safer alternative to lithium-ion. *Science (80-.).* **356**, 415–418 (2017).

80. Ko, J. S. *et al.* Robust 3D Zn Sponges Enable High-Power, Energy-Dense Alkaline Batteries. *ACS Appl. Energy Mater.* **2**, 212–216 (2019).

81. Wu, Y. *et al.* Ion-Sieving Carbon Nanoshells for Deeply Rechargeable Zn-Based Aqueous Batteries. *Adv. Energy Mater.* **8**, 1802470 (2018).

82. Chen, P. *et al.* A deeply rechargeable zinc anode with pomegranate-inspired nanostructure for high-energy aqueous batteries. *J. Mater. Chem. A* **6**, 21933–21940 (2018).

83. Wang, J. M., Zhang, L., Zhang, C. & Zhang, J. Q. Effects of bismuth ion and tetrabutylammonium bromide on the dendritic growth of zinc in alkaline zincate solutions. *J. Power Sources* **102**, 139–143 (2001).

84. Lee, S.-M. *et al.* Improvement in self-discharge of Zn anode by applying surface modification for Zn–air batteries with high energy density. *J. Power Sources* **227**, 177–184 (2013).

85. Cho, Y.-D. & Fey, G. T.-K. Surface treatment of zinc anodes to improve discharge capacity and suppress hydrogen gas evolution. *J. Power Sources* **184**, 610–616 (2008).

86. Zhang, Z., Yang, Z., Huang, J., Feng, Z. & Xie, X. Enhancement of electrochemical performance with Zn-Al-Bi layered hydrotalcites as anode material for Zn/Ni

secondary battery. *Electrochim. Acta* **155**, 61–68 (2015).

87.   Dikin, D. A. *et al.* Preparation and characterization of graphene oxide paper. *Nature* **448**, 457–460 (2007).

88.   Mi, B. Graphene Oxide Membranes for Ionic and Molecular Sieving. *Science (80-.).* **343**, 740–742 (2014).

89.   Fan, X. *et al.* Deoxygenation of exfoliated graphite oxide under alkaline conditions: a green route to graphene preparation. *Adv. Mater.* **20**, 4490–4493 (2008).

90.   Marcano, D. . C. *et al.* Improved Synthesis of Graphene Oxide. *ACS Nano* **4**, 4806–4814 (2010).

91.   Rashidi, F., Kevlich, N. S., Sinquefield, S. A., Shofner, M. L. & Nair, S. Graphene Oxide Membranes in Extreme Operating Environments: Concentration of Kraft Black Liquor by Lignin Retention. *ACS Sustain. Chem. Eng.* **5**, 1002–1009 (2017).

92.   Parker, J. F., Chervin, C. N., Nelson, E. S., Rolison, D. R. & Long, J. W. Wiring zinc in three dimensions re-writes battery performance—dendrite-free cycling. *Energy Environ. Sci.* **7**, 1117–1124 (2014).

93.   Kołodziejczak-Radzimska, A. & Jesionowski, T. Zinc Oxide—From Synthesis to Application: A Review. *Materials (Basel).* **7**, 2833–2881 (2014).

94.   Bian, S.-W., Mudunkotuwa, I. A., Rupasinghe, T. & Grassian, V. H. Aggregation and Dissolution of 4 nm ZnO Nanoparticles in Aqueous Environments: Influence of pH, Ionic Strength, Size, and Adsorption of Humic Acid. *Langmuir* **27**, 6059–6068 (2011).

95.   Wang, L., Liu, Y., Chen, X., Qin, H. & Yang, Z. Zinc Aluminum Antimony Hydrotalcite as Anode Materials for Ni-Zn Secondary Batteries. *J. Electrochem. Soc.* **164**, A3692–A3698 (2017).

96.   Long, J., Yang, Z., Zhang, Z. & Huang, J. Sheet-Like Carbon-Coated Zn-Al-Bi Layered Double Oxides Nanocomposites Enabling High Performance for Rechargeable Alkaline Batteries. *J. Electrochem. Soc.* **164**, A3068–A3074 (2017).

97.   Zeng, X. *et al.* An in situ recovery method to prepare carbon-coated Zn–Al–hydrotalcite as the anode material for nickel–zinc secondary batteries. *RSC Adv.* **7**, 44514–44522 (2017).

98.   Sun, L. *et al.* Fast and Energy Efficient Synthesis of ZnO@RGO and its Application in Ni-Zn Secondary Battery. *J. Phys. Chem. C* **120**, 12337–12343 (2016).

99.   Boukhvalov, D. W., Katsnelson, M. I. & Son, Y. Origin of Anomalous Water Permeation through Graphene Oxide Membrane. *Nano Lett.* **13**, 3930–3935 (2013).

100. Chabot, V. *et al.* A review of graphene and graphene oxide sponge: material synthesis and applications to energy and the environment. *Energy Environ. Sci.* **7**, 1564 (2014).

101. Sun, P., Wang, K. & Zhu, H. Recent Developments in Graphene-Based Membranes: Structure, Mass-Transport Mechanism and Potential Applications. *Adv. Mater.* **28**, 2287–2310 (2016).

102. Marcus, Y. Volumes of aqueous hydrogen and hydroxide ions at 0 to 200 °C. *J. Chem. Phys.* **137**, 154501 (2012).

103. Pessine, E. J., Agostinho, S. M. L. & Chagas, H. C. Evaluation of the diffusion coefficient of the zincate ion using a rotating disk electrode. *Can. J. Chem.* **64**, 523–527 (1986).

104. Abraham, J. *et al.* Tunable sieving of ions using graphene oxide membranes. *Nat. Nanotechnol.* **12**, 546–550 (2017).

105. Akbari, A. *et al.* Large-area graphene-based nanofiltration membranes by shear alignment of discotic nematic liquid crystals of graphene oxide. *Nat. Commun.* **7**, 10891 (2016).

106. Adler, T. C. Low-Zinc-Solubility Electrolytes for Use in Zinc/Nickel Oxide Cells. *J. Electrochem. Soc.* **140**, 289 (1993).

107. Jindra, J. *et al.* ESCA investigations on plastic-bonded nickel oxide electrodes. *J. Power Sources* **13**, 123–136 (1984).

108. Greaves, C., Thomas, M. A. & Turner, M. Structural and electrochemical characteristics of plastic (PTFE) bonded nickel hydroxide electrodes. *J. Power Sources* **12**, 195–202 (1984).

109. Tessier, C. *et al.* Electrochemical Study of Zinc-Substituted Nickel Hydroxide. *J. Electrochem. Soc.* **149**, A1136 (2002).

110. Obrovac, M. N., Christensen, L., Le, D. B. & Dahn, J. R. Alloy Design for Lithium-Ion Battery Anodes. *J. Electrochem. Soc.* **154**, A849 (2007).

111. Parker, J. F. *et al.* Retaining the 3D framework of zinc sponge anodes upon deep discharge in Zn-Air cells. *ACS Appl. Mater. Interfaces* **6**, 19471–19476 (2014).

112. Parker, J. F., Chervin, C. N., Nelson, E. S., Rolison, D. R. & Long, J. W. Wiring zinc in three dimensions re-writes battery performance—dendrite-free cycling. *Energy Environ. Sci.* **7**, 1117 (2014).

113. Lee, S., Yi, C. & Kim, K. Characteristics and Electrochemical Performance of the TiO2-Coated ZnO Anode for Ni−Zn Secondary Batteries. *J. Phys. Chem. C* **115**, 2572–2577 (2011).

114. Ma, M. *et al.* Electrochemical performance of ZnO nanoplates as anode materials for Ni/Zn secondary batteries. *J. Power Sources* **179**, 395–400 (2008).

115. Wang, J., Zhong, H., Wang, Z., Meng, F. & Zhang, X. Integrated Three-Dimensional Carbon Paper/Carbon Tubes/Cobalt-Sulfide Sheets as an Efficient Electrode for Overall Water Splitting. *ACS Nano* **10**, 2342–2348 (2016).

116. Parker, J. F., Pala, I. R., Chervin, C. N., Long, J. W. & Rolison, D. R. Minimizing Shape Change at Zn Sponge Anodes in Rechargeable Ni–Zn Cells: Impact of Electrolyte Formulation. *J. Electrochem. Soc.* **163**, A351–A355 (2016).

117. Thermo Fisher Scientific Inc. Supplemental material. Available at: http://xpssimplified.com/elements/titanium.php.

118. Long, J., Yang, Z., Huang, J. & Zeng, X. Self-assembly of exfoliated layered double hydroxide and graphene nanosheets for electrochemical energy storage in zinc/nickel secondary batteries. *J. Power Sources* **359**, 111–118 (2017).

119. Zhang, J. *et al.* The enhanced adhesion between overlong TiNxOy/MnO2nanoarrays and Ti substrate: Towards flexible supercapacitors with high energy density and long service life. *Nano Energy* **43**, 91–102 (2018).

120. Bonnick, P. & Dahn, J. R. A Simple Coin Cell Design for Testing Rechargeable Zinc-Air or Alkaline Battery Systems. *J. Electrochem. Soc.* **159**, A981–A989 (2012).

121. Zeng, D. *et al.* Preparation and electrochemical performance of In-doped ZnO as anode material for Ni-Zn secondary cells. *Electrochim. Acta* **56**, 4075–4080 (2011).

122. Yu, J., Yang, H., Ai, X. & Zhu, X. A study of calcium zincate as negative electrode materials for secondary batteries. *J. Power Sources* **103**, 93–97 (2001).

123. Yang, B., Yang, Z. & Wang, R. Facile synthesis of novel two-dimensional silver-coated layered double hydroxide nanosheets as advanced anode material for Ni–Zn secondary batteries. *J. Power Sources* **251**, 14–19 (2014).

124. Liu, Y., Yang, Z., Xie, X., Huang, J. & Wen, X. Layered Double Oxides Nano-flakes Derived From Layered Double Hydroxides: Preparation, Properties and Application in Zinc/Nickel Secondary Batteries. *Electrochim. Acta* **185**, 190–197 (2015).

125. Yang, B., Yang, Z., Wang, R. & Feng, Z. Silver nanoparticle deposited layered double hydroxide nanosheets as a novel and high-performing anode material for enhanced Ni–Zn secondary batteries. *J. Mater. Chem. A* **2**, 785–791 (2014).

126. Yang, B. & Yang, Z. Structure and improved electrochemical performance of a nanostructured layered double hydroxide–carbon nanotube composite as a novel anode material for Ni–Zn secondary batteries. *RSC Adv.* **3**, 12589 (2013).

127. Zheng, S. *et al.* Nano-copper-assisted immobilization of sulfur in high-surface-area mesoporous carbon cathodes for room temperature Na-S batteries. *Adv. Energy Mater.* **4**, 1–7 (2014).

128. Albers, J., Meissner, E. & Shirazi, S. Lead-acid batteries in micro-hybrid vehicles. *J. Power Sources* **196**, 3993–4002 (2011).

129. Fu, X.-Z. *et al.* β-CoOOH coated spherical β-NiOOH as the positive electrode material for alkaline Zn-NiOOH battery. *J. Power Sources* **164**, 916–920 (2007).

130. Xu, C., Wu, J., Desai, U. V. & Gao, D. High-efficiency solid-state dye-sensitized solar cells based on TiO2-coated ZnO nanowire arrays. *Nano Lett.* **12**, 2420–2424 (2012).

131. Nørskov, J. K. *et al.* Trends in the Exchange Current for Hydrogen Evolution. *J. Electrochem. Soc.* **152**, J23 (2005).

132. Zheng, Y. *et al.* Hydrogen evolution by a metal-free electrocatalyst. *Nat. Commun.* **5**, 3783 (2014).

133. Laursen, A. B. *et al.* Electrochemical Hydrogen Evolution: Sabatier's Principle and the Volcano Plot. *J. Chem. Educ.* **89**, 1595–1599 (2012).

134. Nai, J. *et al.* Efficient Electrocatalytic Water Oxidation by Using Amorphous Ni–Co Double Hydroxides Nanocages. *Adv. Energy Mater.* **5**, 1401880 (2015).

135. Zheng, Y. *et al.* Hydrogen evolution by a metal-free electrocatalyst. *Nat. Commun.* **5**, 3783 (2014).

136. Lim, M. B., Lambert, T. N. & Ruiz, E. I. Effect of ZnO-Saturated Electrolyte on Rechargeable Alkaline Zinc Batteries at Increased Depth-of-Discharge. *J. Electrochem. Soc.* **167**, 060508 (2020).

137. Olivares-Ramírez, J. M., Campos-Cornelio, M. L., Uribe Godínez, J., Borja-Arco, E. & Castellanos, R. H. Studies on the hydrogen evolution reaction on different stainless steels. *Int. J. Hydrogen Energy* **32**, 3170–3173 (2007).

138. Yuan, Y. F. *et al.* Effect of ZnO nanomaterials associated with Ca(OH)2 as anode material for Ni-Zn batteries. *J. Power Sources* **159**, 357–360 (2006).

139. Yuan, Y. F. *et al.* Preparation, characteristics and electrochemical performance of Sn6O4(OH)4-coated ZnO for Zn-Ni secondary battery. *Electrochem. commun.* **8**, 653–657 (2006).

140. Wu, J. Z. *et al.* Ag-modification improving the electrochemical performance of ZnO anode for Ni/Zn secondary batteries. *J. Alloys Compd.* **479**, 624–628 (2009).

141. Zhang, Z. *et al.* Electrochemical performance of ZnO/SnO2 composites as anode

materials for Zn/Ni secondary batteries. *Electrochim. Acta* **134**, 287–292 (2014).

142. Li, Z. Q., Li, B. Q., Qin, Z. X. & Lu, X. Fabrication of porous Ag by dealloying of Ag–Zn alloys in H2SO4 solution. *J. Mater. Sci.* **45**, 6494–6497 (2010).

143. Guo, W. *et al.* MOFs derived Ag/ZnO nanocomposites anode for Zn/Ni batteries. *J. Solid State Chem.* **272**, 27–31 (2019).

144. Guo, W., Tian, Z., Yang, C., Lai, Y. & Li, J. ZIF-8 derived nano-SnO2@ZnO as anode for Zn/Ni secondary batteries. *Electrochem. commun.* **82**, 159–162 (2017).

145. Gao, Y. *et al.* Polymer–inorganic solid–electrolyte interphase for stable lithium metal batteries under lean electrolyte conditions. *Nat. Mater.* **18**, 384–389 (2019).

146. Xue, W. *et al.* Intercalation-conversion hybrid cathodes enabling Li–S full-cell architectures with jointly superior gravimetric and volumetric energy densities. *Nat. Energy* **4**, 374–382 (2019).

147. Pan, H. *et al.* Addressing Passivation in Lithium-Sulfur Battery Under Lean Electrolyte Condition. *Adv. Funct. Mater.* **28**, 1707234 (2018).

148. Turney, D. E. *et al.* Rechargeable Zinc Alkaline Anodes for Long-Cycle Energy Storage. *Chem. Mater.* **29**, 4819–4832 (2017).

149. Parker, J. F., Ko, J. S., Rolison, D. R. & Long, J. W. Translating Materials-Level Performance into Device-Relevant Metrics for Zinc-Based Batteries. *Joule* **2**, 2519–2527 (2018).

150. Higashi, S., Lee, S. W., Lee, J. S., Takechi, K. & Cui, Y. Avoiding short circuits from zinc metal dendrites in anode by backside-plating configuration. *Nat. Commun.* **7**, 11801 (2016).

151. Yan, Y. *et al.* A Lasagna-Inspired Nanoscale ZnO Anode Design for High-Energy Rechargeable Aqueous Batteries. *ACS Appl. Energy Mater.* **1**, 6345–6351 (2018).

152. Yuan, Y. F., Tu, J. P., Wu, H. M., Li, Y. & Shi, D. Q. Size and morphology effects of ZnO anode nanomaterials for Zn/Ni secondary batteries. *Nanotechnology* **16**, 803–808 (2005).

153. Zhang, C., Wang, J. M., Zhang, L., Zhang, J. Q. & Cao, C. N. Study of the performance of secondary alkaline pasted zinc electrodes. *J. Appl. Electrochem.* **31**, 1049–1054 (2001).

154. Michlik, T., Schmid, M., Rosin, A., Gerdes, T. & Moos, R. Mechanical Coating of Zinc Particles with Bi2O3-Li2O-ZnO Glasses as Anode Material for Rechargeable Zinc-Based Batteries. *Batteries* **4**, 12 (2018).

155. Stock, D. *et al.* Design Strategy for Zinc Anodes with Enhanced Utilization and

Retention: Electrodeposited Zinc Oxide on Carbon Mesh Protected by Ionomeric Layers. *ACS Appl. Energy Mater.* **1**, acsaem.8b01117 (2018).

156. Kim, J. *et al.* Improved cell performances in Ni/Zn redox batteries fabricated by ZnO materials with various morphologies synthesized using amine chelates. *J. Ind. Eng. Chem.* **56**, 463–471 (2017).

157. Kang, S. *et al.* The incorporation of Cr ions into the framework of ZnO for stable electrochemical performance in a membrane free alkaline Ni/Zn redox. *Electrochim. Acta* **209**, 623–631 (2016).

158. Im, Y. *et al.* Inhibition of Zn dendrite growth using Ni x Zn (1-x) O anodic material during a redox cycling test in Zn/Ni battery. *Solid State Ionics* **295**, 13–24 (2016).

159. Kwak, B. S. *et al.* Synthesis of microcrystalline ZnO as an anodic material via a solvothermal method, and its electrochemical performance in Ni/Zn redox battery. *J. Ind. Eng. Chem.* **46**, 111–118 (2017).

160. Kwak, B. S., Kim, D. Y., Park, S. S., Kim, B. S. & Kang, M. Implementation of stable electrochemical performance using a Fe0.01ZnO anodic material in alkaline Ni–Zn redox battery. *Chem. Eng. J.* **281**, 368–378 (2015).

161. Im, Y. *et al.* Electrochemical performance of three shaped ZnO nanoparticles prepared in LiOH, NaOH and KOH alkaline solutions as anodic materials for Ni/Zn redox batteries. *Korean J. Chem. Eng.* **33**, 1447–1455 (2016).

162. Im, Y. *et al.* Influence of small amount of Mg incorporated into hexagonal ZnO crystal on cell performance in membrane free Zinc–Nickel redox battery. *J. Ind. Eng. Chem.* **64**, 318–327 (2018).

163. Yufit, V. *et al.* Operando Visualization and Multi-scale Tomography Studies of Dendrite Formation and Dissolution in Zinc Batteries. *Joule* **3**, 485–502 (2019).

164. Yan, K. *et al.* Selective deposition and stable encapsulation of lithium through heterogeneous seeded growth. *Nat. Energy* **1**, 16010 (2016).

165. Lee, Y.-G. *et al.* High-energy long-cycling all-solid-state lithium metal batteries enabled by silver–carbon composite anodes. *Nat. Energy* **5**, 299–308 (2020).

166. Huang, J. & Yang, Z. A one-pot method to prepare a ZnO/Ag/polypyrrole composite for zinc alkaline secondary batteries. *RSC Adv.* **5**, 33814–33817 (2015).

167. Yu, J. *et al.* Ag-Modified Cu Foams as Three-Dimensional Anodes for Rechargeable Zinc–Air Batteries. *ACS Appl. Nano Mater.* **2**, 2679–2688 (2019).

168. Cui, M. *et al.* Quasi-Isolated Au Particles as Heterogeneous Seeds To Guide Uniform Zn Deposition for Aqueous Zinc-Ion Batteries. *ACS Appl. Energy Mater.* **2**, 6490–6496 (2019).

169. Shi, X. *et al.* Homogeneous Deposition of Zinc on Three-Dimensional Porous Copper Foam as a Superior Zinc Metal Anode. *ACS Sustain. Chem. Eng.* **7**, 17737–17746 (2019).

170. Kresse, G. & Furthmüller, J. Efficiency of ab-initio total energy calculations for metals and semiconductors using a plane-wave basis set. *Comput. Mater. Sci.* **6**, 15–50 (1996).

171. Kresse, G. & Furthmüller, J. Efficient iterative schemes for ab initio total-energy calculations using a plane-wave basis set. *Phys. Rev. B* **54**, 11169–11186 (1996).

172. Perdew, J. P., Burke, K. & Ernzerhof, M. Generalized Gradient Approximation Made Simple. *Phys. Rev. Lett.* **77**, 3865–3868 (1996).

173. Blöchl, P. E. Projector augmented-wave method. *Phys. Rev. B* **50**, 17953–17979 (1994).

174. Monkhorst, H. J. & Pack, J. D. Special points for Brillouin-zone integrations. *Phys. Rev. B* **13**, 5188–5192 (1976).

175. Gómez-Acebo, T. Thermodynamic assessment of the Ag-Zn system. *Calphad* **22**, 203–220 (1998).

176. Massalski, T. B. & Okamoto, H. *Binary Alloy Phase Diagrams*. (ASM International, 1990).

177. Wei, X. *et al.* Impact of anode substrates on electrodeposited zinc over cycling in zinc-anode rechargeable alkaline batteries. *Electrochim. Acta* **212**, 603–613 (2016).

178. Zhang, Y. *et al.* Deeply Rechargeable and Hydrogen-Evolution-Suppressing Zinc Anode in Alkaline Aqueous Electrolyte. *Nano Lett.* **20**, 4700–4707 (2020).

179. Higashi, S., Lee, S. W., Lee, J. S., Takechi, K. & Cui, Y. Avoiding short circuits from zinc metal dendrites in anode by backside-plating configuration. *Nat. Commun.* **7**, 11801 (2016).

180. Yuan, Y. F., Tu, J. P., Wu, H. M., Li, Y. & Shi, D. Q. Size and morphology effects of ZnO anode nanomaterials for Zn/Ni secondary batteries. *Nanotechnology* **16**, 803–808 (2005).

181. Parker, J. F. *et al.* Rechargeable nickel-3D zinc batteries: An energy-dense, safer alternative to lithium-ion. *Science (80-.).* **356**, 415–418 (2017).

182. Lee, S. H., Yi, C. W. & Kim, K. Characteristics and electrochemical performance of the TiO 2-coated ZnO anode for Ni-Zn secondary batteries. *J. Phys. Chem. C* **115**, 2572–2577 (2011).

183. Sato, Y. *et al.* Gas evolution behavior of Zn alloy powder in KOH solution. *J. Power*

Sources **38**, 317–325 (1992).

184. Yano, M., Fujitani, S., Nishio, K., Akai, Y. & Kurimura, M. Effect of additives in zinc alloy powder on suppressing hydrogen evolution. *J. Power Sources* **74**, 129–134 (1998).

185. Li, Y.-J. *et al.* Multiscale Structural Engineering of Ni-Doped CoO Nanosheets for Zinc–Air Batteries with High Power Density. *Adv. Mater.* **30**, 1804653 (2018).

186. Tan, M. J. *et al.* Acrylamide-derived freestanding polymer gel electrolyte for flexible metal-air batteries. *J. Power Sources* **400**, 566–571 (2018).

187. Lee, H.-J. *et al.* Electrospun polyetherimide nanofiber mat-reinforced, permselective polyvinyl alcohol composite separator membranes: A membrane-driven step closer toward rechargeable zinc–air batteries. *J. Memb. Sci.* **499**, 526–537 (2016).

188. Meng, J. *et al.* Spent alkaline battery-derived manganese oxides as efficient oxygen electrocatalysts for Zn–air batteries. *Inorg. Chem. Front.* **5**, 2167–2173 (2018).

189. Li, H. *et al.* Colloidal Cobalt Phosphide Nanocrystals as Trifunctional Electrocatalysts for Overall Water Splitting Powered by a Zinc–Air Battery. *Adv. Mater.* **30**, 1705796 (2018).

190. Li, B. *et al.* Sheet-on-Sheet Hierarchical Nanostructured C@MnO2 for Zn-Air and Zn-MnO 2 Batteries. *ChemNanoMat* **3**, 401–405 (2017).

191. Li, B. *et al.* A Robust Hybrid Zn-Battery with Ultralong Cycle Life. *Nano Lett.* **17**, 156–163 (2017).

192. Niu, W. *et al.* Surface-Modified Porous Carbon Nitride Composites as Highly Efficient Electrocatalyst for Zn-Air Batteries. *Adv. Energy Mater.* **8**, 1701642 (2018).

193. Olivares-Ramírez, J. M., Campos-Cornelio, M. L., Uribe Godínez, J., Borja-Arco, E. & Castellanos, R. H. Studies on the hydrogen evolution reaction on different stainless steels. *Int. J. Hydrogen Energy* **32**, 3170–3173 (2007).